

Department of Physics and Astronomy

University of Heidelberg

Master thesis

in Physics

submitted by

Sotirios Nikas

born in Athens

2017

# Characterization studies of PACIFIC readout ASIC for the LHCb SciFi Tracker.

This Master thesis has been carried out by Sotirios Nikas

at the

Physikalisches Institut

under the supervision of

Prof. Dr. Ulrich Uwer

## **Kurzfassung:**

Während des Long Shutdown 2 des LHC in 2019/2020 wird ein Upgrade am LHCb experiment durchgeführt. Der bestehende "outer tracker" wird ersetzt um mit der höheren instantanen Luminosität und der gestiegenen Ausleserate von 40 MHz umgehen zu können. Die neue Detektorkomponente verwendet szintillierende Fasern, die mit Hilfe von silicon photomultiplier (SiPMs) ausgelesen werden. Ein neuer ASIC (genannt PACIFIC) wird entwickelt, um das Signal der SiPMs zu verarbeiten.

In dieser Arbeit werden die Ergebnisse einer Charakterisierung zweier Versionen, PACIFICr3 und PACIFICr4, vorgestellt. Insbesondere untersucht wird die Kalibrierungsroutine, die für ein gleichmäßiges Verhalten aller Kanäle des ASIC sorgt. Außerdem wird festgestellt, wie sich eine Anpassung des Zeitfensters der Signalintegration, relativ zur Ankunftszeit des Signals, auswirkt. Eine  $^{90}\text{Sr}$ -Quelle wird verwendet, um die Kalibration des Chips, die Rekonstruktion des Strahlprofils, sowie die Clusterisierung der Eingangssignale und die generelle Funktionalität zu überprüfen. Zusätzlich erfolgt eine Charakterisierung der SiPMs anhand des PACIFICr4.

## **Abstract:**

The LHCb experiment will undergo an upgrade during the LHC's Long Shutdown 2 in 2019/2020. The current outer tracker of the LHCb will be replaced in order to cope with higher instantaneous luminosities and an increased readout rate of 40 MHz. The new tracker is realised with scintillating fibers which are read out by silicon photomultipliers (SiPMs). A new ASIC (PACIFIC) is developed to process and digitize the signal from the SiPMs.

This thesis presents characterization results from two PACIFIC versions, namely PACIFICr3 and PACIFICr4. In particular, the calibration routine allowing a uniform response of PACIFIC and the adjustment of the arrival time of the signal with respect to integration window of PACIFIC are investigated. In addition, signal cluster studies were conducted with a  $^{90}\text{Sr}$  source in the lab to verify the calibration, reconstruct the beam profile, understand the exhibited cluster size and general performance of the chip. Moreover, a characterization of the SiPMs is performed using PACIFICr4.

# Contents

<b>1</b>	<b>Introduction</b>	<b>7</b>
<b>2</b>	<b>The LHCb experiment</b>	<b>9</b>
2.1	Theoretical overview . . . . .	10
2.1.1	Standard Model . . . . .	10
2.1.2	CP violation . . . . .	11
2.2	Physics at the LHCb experiment . . . . .	12
2.3	The LHCb detector . . . . .	13
2.3.1	Tracking detectors . . . . .	13
2.3.2	Particle Identification (PID) . . . . .	15
2.3.3	Trigger System . . . . .	16
2.4	The LHCb Upgrade . . . . .	17
<b>3</b>	<b>The LHCb Scintillating Fibre Tracker (SciFi)</b>	<b>19</b>
3.1	Requirements . . . . .	19
3.2	Radiation Environment . . . . .	20
3.3	Layout of the SciFi Detector . . . . .	21
3.4	Scintillating Fibres . . . . .	22
3.4.1	Organic Scintillators . . . . .	22
3.4.2	Fibre Mats . . . . .	23
3.4.3	Fibre Modules . . . . .	25
3.5	Silicon Photomultiplier (SiPMs) . . . . .	26
3.5.1	Semiconductors . . . . .	26
3.5.2	Avalanche Photo Diodes (APDs) . . . . .	28
3.5.3	Characteristic properties of SiPMs . . . . .	29
3.5.4	Hamamatsu SiPMs . . . . .	31
<b>4</b>	<b>PACIFIC</b>	<b>32</b>
4.1	PACIFIC specifications . . . . .	33
4.1.1	PACIFIC evolution . . . . .	34
4.2	PACIFIC Channel Structure . . . . .	34
4.2.1	SiPM model . . . . .	34
4.2.2	Input Stage . . . . .	36
4.2.3	Shaper Stage . . . . .	37
4.2.4	Gated Integrator . . . . .	37
4.2.5	Track and Hold . . . . .	39
4.2.6	DC Correction (Common Mode Control) . . . . .	39

4.2.7	Digitization . . . . .	40
4.3	Slow Control . . . . .	42
4.4	Clusterization . . . . .	43
4.5	Threshold Scan . . . . .	45
<b>5</b>	<b>PACIFICr3 characterization studies</b>	<b>47</b>
5.1	Motivation . . . . .	47
5.1.1	Light Injection System . . . . .	47
5.1.2	Beta source setup . . . . .	48
5.2	DC Baseline variation of the integrators . . . . .	49
5.2.1	DC baseline difference for two PACIFICr3 ASICs . . . . .	49
5.2.2	DC baseline difference between two integrators within the same channel . . . . .	52
5.2.3	DC baseline difference between different states of PACIFIC . .	53
5.3	Light injection measurements . . . . .	54
5.3.1	Delay Scan . . . . .	55
5.3.2	Tuning $V_{offset}$ . . . . .	56
5.3.3	Calibration of the threshold DACs . . . . .	59
5.4	Beta source measurements . . . . .	59
5.4.1	Selection of events: Finetiming . . . . .	60
5.4.2	Delay Scan . . . . .	61
5.4.3	Threshold bit pattern . . . . .	62
5.4.4	Cluster distribution/size . . . . .	63
5.4.5	Threshold scan with a beta source . . . . .	66
<b>6</b>	<b>PACIFICr4 characterization studies</b>	<b>71</b>
6.1	DC baseline variation of the integrators . . . . .	73
6.1.1	DC baseline difference between different states of PACIFIC . .	74
6.2	Light injection measurements . . . . .	75
6.2.1	Delay Scan . . . . .	75
6.2.2	Breakdown voltage determination . . . . .	76
6.2.3	Verification of $V_{offset}$ . . . . .	78
6.2.4	Linearity region . . . . .	79
6.2.5	Calibration of threshold DACs . . . . .	81
6.3	Beta source measurements . . . . .	84
6.3.1	Delay Scan . . . . .	84
6.3.2	Finetiming . . . . .	84
6.3.3	Threshold bit pattern . . . . .	85
6.3.4	Cluster distribution/size . . . . .	88
<b>7</b>	<b>Conclusion</b>	<b>90</b>
7.0.5	Outlook . . . . .	90

<b>I</b>	<b>Appendix</b>	<b>92</b>
<b>A</b>	<b>Lists</b>	<b>94</b>
A.1	List of Figures . . . . .	94
A.2	List of Tables . . . . .	99
<b>B</b>	<b>Bibliography</b>	<b>100</b>

# 1 Introduction

Our current knowledge of particle physics is encapsulated in the so-called Standard Model. However, indirect experimental observations such as dark matter, neutrino mass and matter-anti matter asymmetry have not been fully answered yet.

The desire for exploring high energy physics has led to the construction of the world's largest circular accelerator, the Large Hadron Collider (LHC) at CERN<sup>1</sup>, placed close to Geneva. One of the experiments at the LHC is the LHCb experiment designed to study CP violation and rare decays.

For revealing new physics effects beyond the Standard Model, precision measurements are needed. To maximize the sensitivity to the physical observables of the Standard Model, the highest LHC energies and luminosities are used. For many LHCb results so far, the measurement uncertainties are dominated by statistical uncertainties. An increase of the data collection rates is currently limited by the 1MHz hardware trigger rate. Thus, the LHCb detector is going to be upgraded during the next LHC shutdown in 2019/20. Increasing the readout rate from 1 MHz to 40 MHz combined with the increased luminosity of  $2 \times 10^{33} \text{ cm}^{-2} \text{ s}^{-1}$ , five times higher than the current luminosity, allows to increase the annual signal yield by a factor 10 for the leptonic channels and a factor 20 for hadronic channels. The statistical uncertainties in some channels will be reduced down to the theoretical levels after 10 years of data collection. Several detectors will also undergo an upgrade. Among them, the current tracking system equipped with a hybrid system comprising a silicon strip Inner Tracker(IT) surrounding the beam pipe and a straw drift tube<sup>2</sup> Outer Tracker(OT) will be replaced by the Scintillating Fibre Tracker, in order to cope with so high particle multiplicities, increased hit occupancy and radiation damage resulting after the upgrade.

The three OT/IT tracking stations will be replaced by a Scintillating Fibre Tracker (SciFi). The detector modules are realized with 2.5 m long scintillating fibres of 250  $\mu\text{m}$  diameter. The fibres will be read out by Silicon Photomultipliers (SiPMs). Eventually, the SiPMs are read out by a dedicated ASIC(Application Specific Integrated Circuit), the so-called PACIFIC.

The PACIFIC is directly connected to the SiPMs. Its input stage, including a current conveyor, allows to control the DC voltage of the input anode of SiPMs achieving a uniform gain response among the channels. Due to the light propagation along the 2.5 long fibre, the signal of the SiPMs can be distributed over two LHC clock periods. Thus, a configurable shaper is used for performing tail cancellation prior integration minimizing thereby the spill over and the fluctuation of the integrated

---

<sup>1</sup>CERN is acronym for the French Conseil Européen pour la Recherche Nucléaire

<sup>2</sup>The straw drift tubes have 5 mm diameter.

signal as a function of the signal arrival time. Two interleaved integrators are used for implementing the integration of the signal in order to minimize the dead time. Finally, the digitization is based on configurable non-linear thresholds that fulfil the requirements of clusterization, aiming for high hit efficiency while simultaneously effectively reducing noise. Only three thresholds are used for the digitization of the integrator output providing a data reduction at the hardware level.

In this study the first characterization results of the latest available prototypes of PACIFIC, that is PACIFICr3 and PACIFICr4, are presented. Employing the available tools, the chip is adjusted to the given SiPM device and thereby it is prepared for clusterization studies using a beta source.

In Chapter 2, the fundamental notions of Standard Model and CP violation as well as the current LHCb detector and its upgrade are discussed. A more detailed description of the SciFi detector is given in Chapter 3. The PACIFIC ASIC and its functionality are explained in Chapter 4. While, in Chapter 5 and 6 the characterization results of PACIFICr3 and PACIFICr4 are presented. A conclusion and an outlook follow in Chapter 7.

## 2 The LHCb experiment

### LHC experiments

The Large Hadron Collider (LHC) at CERN in Switzerland is a circular hadron-hadron collider [1] with a circumference of 26.7 km. It is buried 100 meters underneath the French and Swiss border. Bunches of protons are accelerated and kept on their circular path by means of super-conducting magnets. At a center of mass energy of 14 TeV, the particles have a speed close to the speed of light. At the four collision points, the following detectors are positioned.

- ATLAS (A Toroidal LHC Apparatus) [2]
- CMS (Compact Muon Solenoid) [3]
- LHCb (Large Hadron Collider beauty) [4]
- ALICE(A Large Ion Collider Experiment) [5]
- TOTEM(Total Cross Section, Elastic Scattering and Diffraction Dissociation) [6]
- LHCf(LHC-forward) [7]
- MoEDAL (Monopole and Exotics Detector At the LHC) [8]

Each detector is designed to study different aspects of the Standard Model. The location of each experiment at CERN is shown in Fig. 2.1.

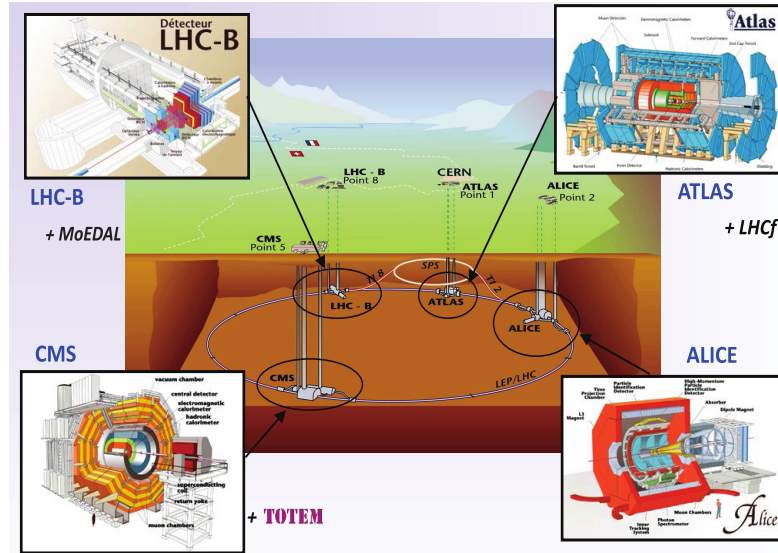


Figure 2.1: Detector positions along CERN accelerator chain. Taken from [9]

## 2.1 Theoretical overview

### 2.1.1 Standard Model

The elementary particles and the forces between them are described by an elegant theory, the so-called "Standard Model".

The Standard Model is a quantum field theory which describes the elementary particles and their interactions. It is a theory which incorporates Special Relativity and Quantum Mechanics in order to describe the particles and forces as quantum excitations of fields.

In this context, fermions are excitations of a fermionic field with spin  $1/2$ . Such particles are the quarks and leptons comprising of 12 particles in total. Six of them carrying the color charge of the strong interaction are the quarks. The quarks are further sorted based on their flavour: up, down, charm, strange, top and beauty. The six remaining fermions which do not carry color charge are the leptons. Leptons are sorted in turn into three families, the electron, muon and tauon with their corresponding neutrinos.

Each of those twelve particles has its own antiparticle with same mass and reversed charge and quantum numbers, respectively.

The forces observed in the universe are the interactions between fermions and are described as an exchange of bosons with spin equal to 1. In the SM, three forces exist: the electromagnetic, the strong nuclear and the weak nuclear force. Photons, W and Z bosons are excitations of the electroweak gauge fields. Photons are the force mediators of the electromagnetic force, while W and Z bosons are the mediators of the weak nuclear force. Gluons are excitations of the strong gauge field and force mediators of strong nuclear force. Finally, the Higgs boson is the excitation of

the Higgs field which gives mass to the elementary particles.

The periodic table of elementary particles described by standard model is summarized in Fig. 2.2.

The SM has been validated over the last 50 years. A large missing piece in the Standard Models was the Higgs boson. It was predicted in 1964 by Peter Higgs and discovered 48 years later[10].

The quarks introduced before are obeying the so-called "Color confinement", thus they can not be directly observed but rather they are always bound together in order to form hadrons. The hadrons are sorted into mesons and baryons. The mesons consist of one quark and anti-quark. While the baryons are made of three quarks. However, the LHCb collaboration has confirmed the existence of exotic four-quark and five-quark particles which had been predicted by theory[11].

Despite the triumphs of SM, it is not capable of explaining all observations. Open questions such neutrino masses, dark energy and dark matter may extend the SM or even replace it by new theories. Moreover, the fact that the SM does not incorporate gravity, a force between objects due to their mass, indicates that this is not the end of the story.

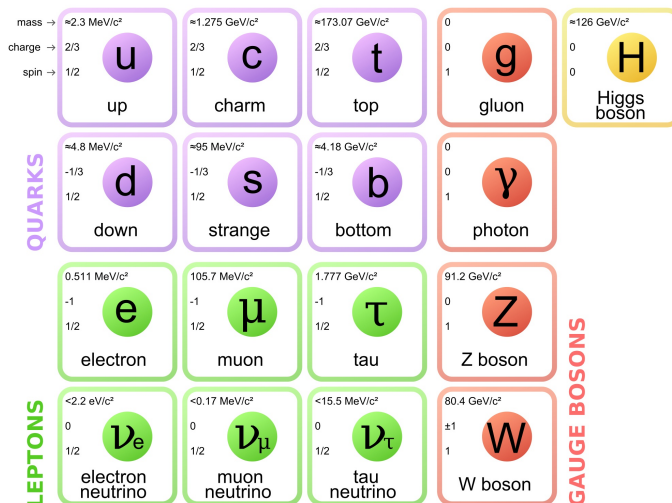


Figure 2.2: All elementary particles with their masses and spins described by Standard model. Taken from [12]

### 2.1.2 CP violation

According to the Big Bang theory, matter and antimatter were equally created [13]. When matter and anti-matter collide, they typically annihilate into photons. Nevertheless, not all of the matter annihilated into photons: about one out of every billion particles eventually survived. These relics originated our Universe. This leads to the question why matter survived instead of anti-matter resulting in the observed Baryon-Anti-Baryon Asymmetry. It was the Russian physicist Andrei Sakharov

(1967) who postulated the three conditions giving an explanation to Baryon-Anti-Baryon Asymmetry [14].

The discovery of CP violation occurred in 1964. Val Fitch and Jim Cronin observed this in the decays of neutral kaons. Although the observed effect was small, it was sufficient to prove that matter and anti-matter are different. Predictions of CP violation in the kaon system are different due to the nature of strong force binding the quarks together. However, the theoretical calculations are facilitated with heavier quarks such as the beauty quark which is constituent of B meson. The amount of CP violation symmetry is quantified by the area of the Unitary triangle formed by the parameters of the Kobayashi-Maskawa mechanism [15].

Symmetries are a fundamental principle in physics. The Noether Theorem attributes any symmetry in nature to a conservation of physics law.

The CP symmetry refers to the combination of the discrete symmetries under charge conjugation (C) and parity (P). The C operator conjugates all quantum numbers, thereby transforms particles into antiparticles and vice versa. On the other hand, under P operator all spatial coordinates are inverted. The violation of CP symmetry allows the matter and antimatter asymmetry and the evolution of a predominant matter Universe.

## 2.2 Physics at the LHCb experiment

The LHCb experiment is primarily searching for indications of CP violation effects as well as rare decays of B mesons, namely hadrons consisting of beauty quark.

The study of CP violation in the Standard Model is done by measuring precisely the Cabibbo-Kobayashi-Maskawa (CKM) matrix parameters [16]. In order to investigate whether the Standard Model provides a complete description, it is important to measure CP violation accurately in many different B-particle and charm decays. Thereby, the same observables extracted from the experiments can constrain the parameters of the Kobayashi-Maskawa mechanism forming the Unitary Triangle as has already mentioned before.

Moreover, the production of a very large number of B-hadrons facilitates the observation of very rare decay processes, which are highly suppressed in the Standard Model. For instance, the decay  $B_s \rightarrow \mu^+ \mu^-$  as shown in Fig. 2.3 is predicted by the Standard Model to have a branching fraction of  $(3.66 \pm 0.23) \times 10^{-9}$  [17]. However, if new particles exist beyond the Standard Model, the New Physics could modify the prediction. Recently LHCb measured  $(2.7 \pm 0.7) \times 10^{-9}$ , a measurement which is consistent with the SM model.

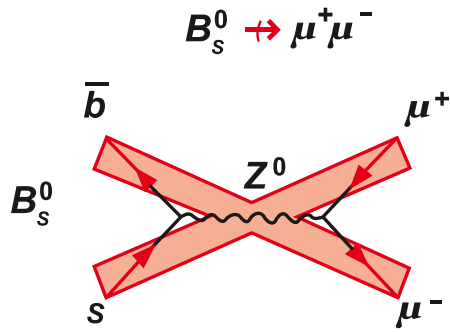


Figure 2.3: The decay of  $B_s^0$  is forbidden in SM through the direct flavour changing neutral current process, due to the  $Z^0$  can not couple directly to quarks of different flavours. However, this transition is allowed for higher order transitions, resulting in a reduced probability of scattering amplitude due to the increased number of interaction vertices considered. Taken from [17]

## 2.3 The LHCb detector

The LHCb detector was designed to probe heavy flavour physics. In particular, the experiment studies the decays of B hadrons. Simulations of the  $\bar{b}b$ -production cross sections as a function of the polar angles have shown that the production is most probable for small angles with respect to the beam pipe as shown in Fig. 2.4 [18].

This led the LHCb detector to be built as a single arm forward spectrometer having a polar angular coverage of 15 to 300 mrad in the horizontal plane and 15 to 250 mrad in the vertical plane [19]. Thereby, the LHCb can observe 25% of the produced  $\bar{b}b$  quarks pairs inside its acceptance area [20].

The realization of a particle detector is based on three different systems. First, a tracking system capable of reconstructing the trajectories of particles pass through the detector. The second system is dedicated to the particle identification and the measurement of deposited energy in the detector by the penetrated particles. Finally the trigger system, allowing the selection of data based on certain criteria. A brief description of the aforementioned systems follows in the next sub-chapters. The LHCb detector is shown in Fig 2.5.

### 2.3.1 Tracking detectors

A tracking detector typically exploits the ionizing effects produced in its sensitive material when charged particle passes through it, thereby providing information of the interaction points in the detector allowing the reconstruction of its trajectory.

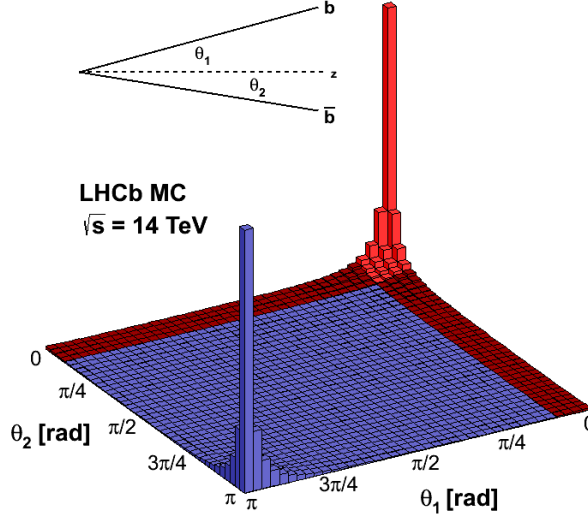


Figure 2.4: A simulation of the cross section for the production of  $\bar{b}b$  quark pairs as a function of the polar angles  $\theta_1$  and  $\theta_2$  with respect to the beam axis. The red color region points the acceptance area of the LHCb detector, while the blue region the area which is not included. Taken from [20]

The LHCb tracking systems are the Vertex Locator (VELO), the Tracker Turicensis (TT) and the tracking stations (T1-T3). The tracking stations (T1-T3) are positioned behind the magnet which are divided in turn in Inner- and Outer Tracker (IT/ OT), respectively.

## VELO

The Velo is a silicon strip detector which surrounds the interaction point. The silicon modules are positioned in such a way providing information for the radial and azimuthal coordinates of tracks along the beam direction. Thereby, it reconstructs primary and secondary interaction vertices with a resolution better than  $13 \mu\text{m}$  on the x and y coordinates using 25 tracks [22].

## Tracker Turicensis (TT)

The TT consists of four layers of silicon strip sensors with a resolution of  $50 \mu\text{m}$  positioned between the magnet and RICH1. It is 150 cm wide and 130 cm long flat tracking station covering the full acceptance of the experiment. It is dedicated to reconstruct and subsequently identify trajectories of low-momentum particles. Since the trajectories of low-momentum particles passing through the magnet are bent out of the acceptance of the experiment and finally do not reach stations T1-

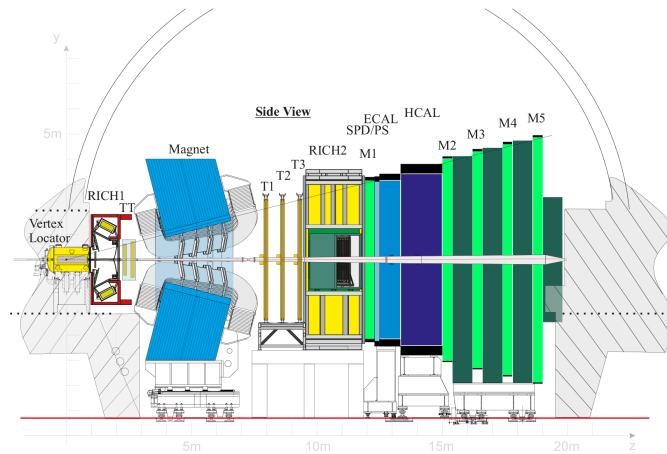


Figure 2.5: Schematic view of the current LHCb experiment. Taken from [21]

T3. Moreover, it is used in the Level-1 trigger to assign transverse momentum information to large-impact parameters tracks [21].

### T1-T3

After the dipole magnet, the three tracking stations (T1-T3) are positioned. Each tracking station consists of an Inner Tracker (IT) and an Outer Tracker (OT), respectively. The IT is a silicon strip detector with a horizontal spatial resolution of  $50 \mu\text{m}$ . It has a cross-shaped layout around the beam pipe allowing a precise measurement of track coordinates. The OT is a gas-filled straw tube having a resolution of  $200 \mu\text{m}$  [21]. Both tracking systems allow the momentum determination exploiting the bending of the charged particle trajectories after passing through the magnet.

### 2.3.2 Particle Identification (PID)

The LHCb employs a particle identification system making use of:

- Ring Imaging Cherenkov (RICH) systems
- Calorimetry system
- Muon system

#### RICH

Ring-Imaging Cherenkov (RICH) detectors are located between VELO and TT and between the T stations and the calorimeter, respectively. They both contribute to particle identification (PID) exploiting the emitted so-called "Cherenkov light",

when charged particles traversing a material having a velocity greater than the speed of light. A Cherenkov light is emitted under a certain angle  $\cos \theta = \frac{1}{\eta\beta}$ , where  $\beta$  is the relativistic velocity defined as  $\beta = \frac{v}{c}$  and  $\eta$  stands for the refraction index of the material. This angle can be used for determining the velocity of particles. Combining thus the momentum information from the tracking system with velocity from the RICH allows to determining the mass of the particle.

### **Calorimetry system (SPD, PS, ECAL, HCAL)**

The Calorimetry system is located after the RICH2 provides the identification of electrons, photons and hadrons thanks to the measurement of their energies and position hits. The Calorimetry consists of the Scintillating Pad Detector (SPD), the Pre-Shower Detector (PS), the Electromagnetic Calorimeter (ECAL) and the scintillating tile iron plate Hadron CALorimeter (HCAL).

The SPD and PS are made of scintillating pads with a thickness of 15 mm. They are both specialized to distinguish the particles passing through the calorimeter whether are charged or neutral. While the ECAL and HCAL use alternating scintillation tiles with absorption materials. The ECAL uses lead whereas the HCAL uses iron for absorption. Finally, the particles induce electromagnetic or hadronic particle showers which in turn are detected by the scintillating tiles [23]. It should be noted that the SPD, PS and ECAL are used by the trigger system so that to indicate the presence of electrons, photons, and neutral pions. Whilst the HCAL provides the information to the Level-0 trigger about the presence of high transverse momentum hadrons, which is a signature of B-events [24].

### **Muon Stations (M1-M5)**

The five muon stations (M1-M5) consist of alternating multi-wire proportional counter (MWPC) with 80 cm thick iron absorber [25]. Only the first muon station (M1) is positioned in front of the calorimeter system. Muons are charged particles like electrons, however, are 200 times more massive. Muons can penetrate several meters of iron without interacting, while other particles will have already stopped. Thus, muon stations are located at the end of the detector, where the only particles most likely to be detected are muons. The Muon system is a part of trigger providing identification of muons.

### **2.3.3 Trigger System**

The current LHCb trigger consists of two stages, the Level-0 (L0) and the High-Level Trigger (HLT). The L0 is responsible for reducing the data rate from 40 MHz to 1 MHz. The reduction of rate is based on information received from the calorimeters and muon chambers. The HLT is a software trigger running on the CPU farm receiving the information coming from the (L0), reducing thereby its rate further to a few kHz [26].

## 2.4 The LHCb Upgrade

During the Long Shut-down 2 in 2019 the LHCb detector will experience an upgrade replacing the first-level hardware trigger (L0) by a trigger-less read-out system of the full detector. The upgraded detector will be capable of reading out every LHC bunch crossing increasing thus the current readout data rate from 1 MHz to 40 MHz event rate. Therefore, it is necessary to apply a data suppression already at the level of the front-end electronics reducing thereby the data throughput. The increase of the recorded luminosity to  $L = 2 \times 10^{33} \text{ cm}^{-2} \text{ s}^{-1}$  five times higher than the current luminosity combined with the higher trigger efficiency and data rate will allow to increase the statistics, which was the primary limiting factor of physics results.

In the end, this is translated to an increase of the annual signal yielding a factor 10 for the leptonic channels and a factor 20 for hadronic channels, respectively. Those yields will offer a statistical sample capable of reaching the experimental sensitivities for many physics observables comparable or even better than the given theoretical uncertainties [27]. A schematic of the upgraded detector equipped with the new Vertex Locator (VeLoPix), the Upstream Tracker (UT) and the Scintillating Fibre Tracker (SciFi), the two RICH detectors and the calorimeter system are shown in Fig. 2.6

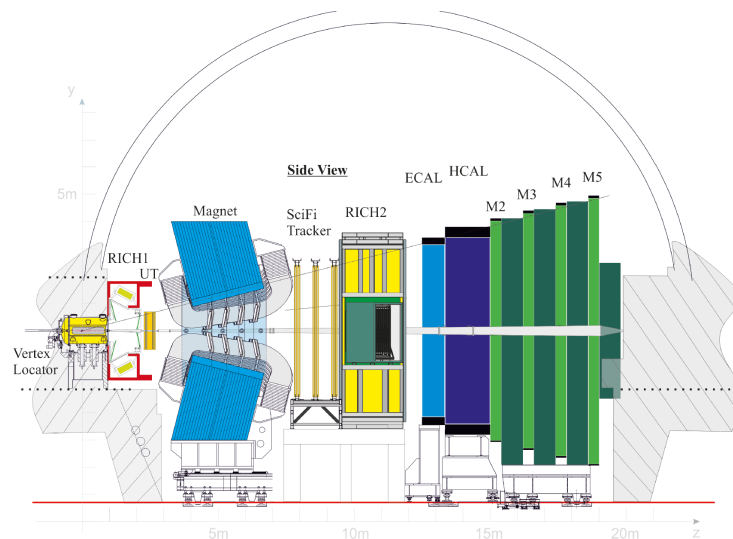


Figure 2.6: Schematic view of the upgraded LHCb experiment. Taken from [21].

### Vertex Locator Pixels (VeLoPix)

The new VELO must maintain the excellent performance as its predecessor although being in harsher conditions. Due to the combination of an increased luminosity by a factor of five and the increased average number of visible proton-proton collision per bunch crossing so-called pile-up, the Velo will cope with higher radiation damage.

The recent technology reviews are favoured of choosing a Si-pixel sensors having dimensions of  $55 \times 55 \mu m^2$  pitch integrated with cooling microchannels [28]. Reducing thus the material budget facilitating the improvement of track reconstruction and spatial resolution. The pixel sensors will be read out by a dedicated ASIC, so-called VeloPix [29].

### **Upstream Tracker (UT)**

The TT will be replaced by four silicon micro-strip planes (UT) increasing the coverage of the LHCb acceptance. Moreover, it will also have a better granularity and improved radiation resistance. The sensors will be read-out by so-called SALT ASIC chip [30].

### **Scintillating Fibre Tracker (SciFi)**

The current IT and OT will be replaced by the Scintillating Fibre Tracker. In the next chapter, a detailed description is given concerning the new SciFi Tracker.

### **RICH**

The general structure of both RICH detectors will not change in the upgrade. However, the fact that the PID performance of RICH system running at such a high rate (40 MHz) will be degraded led to the replacement of some of its components. One of the most important change is the replacement of the current Hybrid photon detectors (HPD) by multianode photomultipliers (MaPMT) [31]. The MaPMT will be read out by so-called "CLARO" ASIC adjusted to the requirements of trigger-less read-out scheme at 40 MHz [32].

### **Calorimeter**

The current ECAL and HCAL will remain to be part of the upgraded Calorimeter. However, the PS and SPD will be removed. Moreover, it turns out that the gain of the PMTs (Photo Multiplier Tubes) have to be intentionally reduced by a factor 5, reducing the ageing effect which will be experienced due to the higher luminosities. The front-end electronics of all subsystems will be redeveloped to fit the reduced gain and the trigger-less readout scheme mentioned above [33].

### **Muon Station**

The 4 layers (M2-M5) made of MWPC will still remain part of the Muon Station. However, the first layer of the Muon Station used in the first level trigger will be replaced by GEM due to the higher multiplicities of particles. In addition, the inner part of M2 positioned close to the beam-pipe where the flux is high will be replaced by GEMs detectors allowing to have finer granularity [31].

## 3 The LHCb Scintillating Fibre Tracker (SciFi)

The current main tracker (T stations) consists of the silicon strip Inner Tracker and the straw tube Outer Tracker is dedicated to determine the momentum of charged particles with high precision. However, running at the upgrade luminosity of  $L = 2 \times 10^{33} \text{ cm}^{-2} \text{ s}^{-1}$  collecting up to  $50 \text{ fb}^{-1}$  integrated luminosity over the lifetime of the upgraded detector will be an issue. The OT occupancy will become too high due to the coarse granularity of the 5 mm straw drift tubes. Therefore, the downstream tracker is to be replaced by a higher granular detector that can cope with such luminosities. Additionally, the trigger-less upgrade read-out scheme dictates the development of new front-end electronics be read out with 40 MHz rate.

A new tracking detector is realized with 2.5 m long scintillating fibres with  $250 \mu\text{m}$  diameter read out by SiPMs. The fibres are wound into fibre mats which in turn are assembled into modules. The detector has 12 layers consisting of 128 modules in total, covering the total acceptance area of the LHCb detector. While its spatial resolution for a reconstructed hit is less than  $100 \mu\text{m}$ .

### 3.1 Requirements

A good tracking system should have high hit efficiency, good spatial resolution, low material budget and ensure the long-term durability performance.

The main requirements are summarised below [34] :

- High hit detection efficiency, better than 99% efficiency for a single hit. Since the high detection efficiency is translated to a good track reconstruction.
- Low material budget of a single detector layer, namely  $\leq 1\%$  of a radiation length  $X_0$ , inducing the least possible multiple scattering of the penetrating particles through the detector.
- The spatial resolution must be less than  $100 \mu\text{m}$  in x direction (bending plane) and the vertical resolution should be 1 mm. Better spatial hit resolution is not necessary since multiple scattering effects in the material before will dominate.
- The detector should be read out by 40 MHz trigger-less electronics with minimum dead time for digitization process.
- The fibres inside the detector should be straight and aligned better than  $50 \mu\text{m}$  in x-direction and flat within  $300 \mu\text{m}$  in z-direction (beam pipe direction).

Allowing thus a precise alignment of the detector necessary to achieve the aforementioned spatial resolution.

- The radiation environment of fibre mat and SiPMs has to be studied to ensure the long term durability performance during the whole lifetime of the detector. On the next paragraph a detailed description of radiation environment is given.

## 3.2 Radiation Environment

The signal to noise ratio depends strongly on the radiation environment. Therefore, it was necessary to perform a FLUKA [35] [36] simulation of the LHCb detector estimating the radiation level for scintillation fibres and SiPMs. The simulation assumes an integrated luminosity of  $50 \text{ fb}^{-1}$ , a proton-proton cross section of  $100 \text{ mb}$  and collision energy at  $14 \text{ TeV}$ .

The resulting  $1 \text{ MeV}$  neutron equivalent fluence and ionizing dose at the position of the tracking station T1 are shown in Fig. 3.1. The fluence at the position of the SiPMs ( $y = \pm 250 \text{ cm}$ ) is expected to reach after an integrated luminosity of  $50 \text{ fb}^{-1}$  to the estimated value of  $9.5 \times 10^{11} \text{ eq/cm}^2$  and  $13 \times 10^{11} \text{ eq/cm}^2$  for T1 and T3, respectively. Moreover, the expected integrated ionising dose for the SiPMs is  $40 \text{ Gy}$  in T1 and  $80 \text{ Gy}$  in T3. While the maximum dose absorbed in the fibres is expected to be around  $35 \text{ kGy}$  and  $25 \text{ kGy}$  at T1 and T3 next to the beam pipe. The simulations have also shown that a shielding can be realized, with a layer of Polyethylene capable of reducing the neutron fluence by a factor of 3-4 in the region of the SiPMs [21],[37].

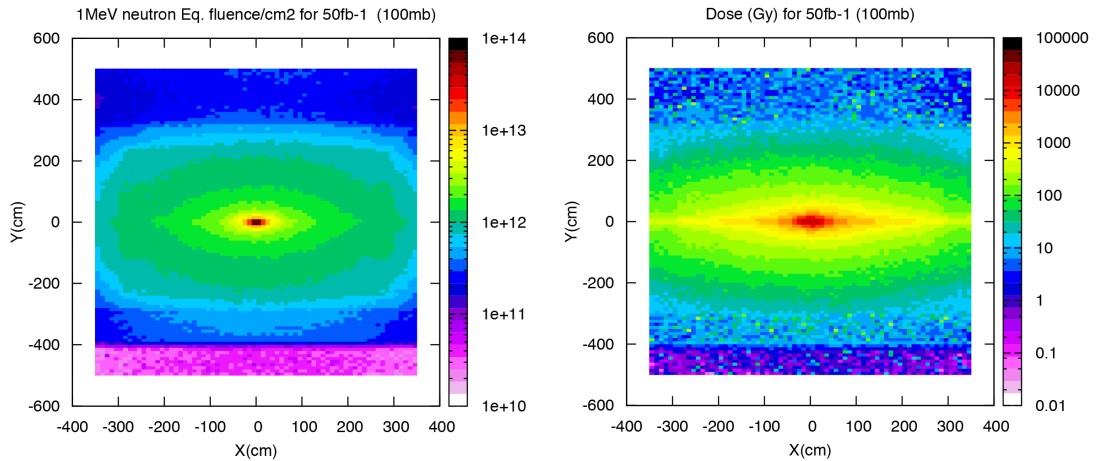


Figure 3.1: Left side: The expected  $1 \text{ MeV}$  neutron equivalent fluence at  $z = 783 \text{ cm}$  after an integrated luminosity of  $50 \text{ fb}^{-1}$ . Right Side: The expected dose in the  $x - y$  plane at  $z = 783 \text{ cm}$  after an integrated luminosity of  $50 \text{ fb}^{-1}$ . Taken from [21]

### 3.3 Layout of the SciFi Detector

The SciFi Tracker is realized as a single detector technology based on scintillating fibres. It is a 6 m wide and 5 m high planar detector covering the full acceptance defined by the experiment. It will consist of three stations (T1, T2, T3), each has four detection layers, which are in turn divided into X, U and V layers. The ("X" layers) are the first and the last layers in each station having no stereo angle with respect to the y-axis. Whilst, the two intermediate layers are tilted by  $\pm 5$  ("U" and "V" layers) providing thereby 1 mm resolution in vertical direction. In T1 and T2 stations, the detection layers are made of 10 modules while in the T3 station consists of 12 modules, leading to a total of 128 modules to cover the dimensions of the detector as shown in Fig 3.2. The dimensions of a module is 4.85 m long and 0.528 m wide. The two central modules in each layer have a squared cut giving space for the beam pipe. Each module consists of eight fibre mats. On the inner ends of fibre mat, the mirror is positioned while on the other end the Readout-Box (ROB) is mounted. The ROB contains the SiPMs, front-end electronics and cooling system. In the end, the modules are mounted on two frames per layer which open and close the beam pipe. .

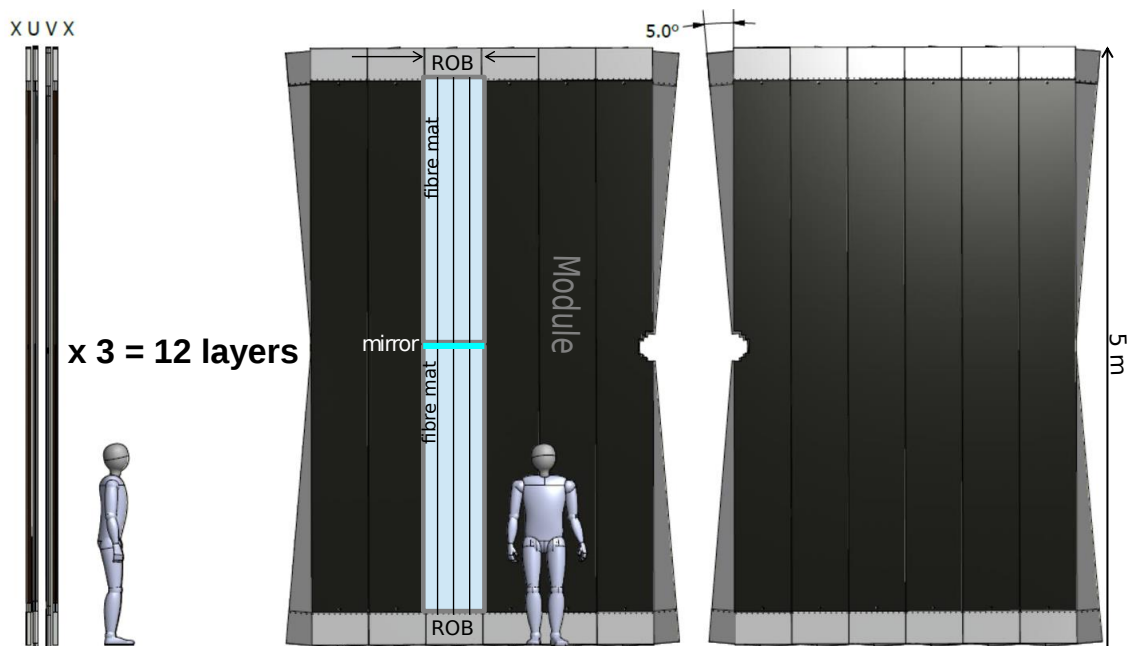


Figure 3.2: One station which consisted of 4 detection layers ("X", "U", "V" and "X") (left). The SciFi view with the squared cut in the middle for the beam pipe (right). Taken from [38]

## 3.4 Scintillating Fibres

### 3.4.1 Organic Scintillators

The scintillation fibres are organic scintillators. A brief description of organic scintillators follows.

The process of light generation in organic scintillators depends on the presence of delocalized electrons. In most scintillators, these electrons are provided by benzene molecules/rings which contain three so-called  $\pi$ -orbitals. When a charged particle passes through the material, its deposited ionisation energy excites the  $\pi$ -electrons. Before the excitation they are in the ground state which itself splits into multiple energy levels due to a coupling between the electronic and the vibrational states of the molecule. The electron goes from initial state  $S_{ix}$ , where  $i$  denotes the electronic state and  $x$  denotes the vibrational level to a state of higher energy  $S_{ix}$ , where  $i = 1, 2, 3$ , etc. These are transitions between singlet states (spin 0). A transition from the ground state to triplet state  $T_x$  is spin-forbidden.

After an electron has been excited, it will lose energy until it reaches the state  $S_{10}$ . The energy is dispersed in a non-radiative way which happens much more quickly than the subsequent radiative decay to one of the ground states  $S_{1x}$ . The radiative decay has a decay time on the order of  $1 \times 10^{-9}$  s, whereas the period of the non-radiative decay is on the order of  $1 \times 10^{-12}$  s [39]. Before the excitation, the electrons are typically in the state of lowest energy  $S_{00}$ . However, the radiative decay can end up in any of the ground states  $S_{i0}$  with the probability determined by the overlap of the wavefunctions of the excited and de-excited states. In combination with the non-radiative energy loss, this leads to the fact that the energy of the emitted photon is on average smaller than the energy that was used for the excitation. This leads to the so-called "Stokes-Shift": The emission spectrum of the scintillator is shifted to longer wavelengths, compared to the absorption spectrum. This reduces the self-absorption and makes it possible to transmit light through the scintillator. In practice, one wants to maximize the Stokes-Shift and radiative efficiency. Therefore, dyes are added to the base scintillator. The energy absorbed by the base is transferred in a non-radiative way to the primary dye, which then emits the photons. The primary dye increases the light yield. While the secondary dye serves as a wavelength shifter (WLS) [40]. The emission spectrum of the whole system is then identical to the emission spectrum of the wavelength shifter.

The SciFi is built from plastic scintillating fibre made of polystyrene (PS) with a circular cross section having a diameter of 250 micrometer. It is covered by two claddings of non-scintillating materials. Those claddings have a lower refractive index for improving the transmission characteristics of the fibre.

Due to the reflection only a small part of the scintillation light will be trapped in the fibre. The trapped photons will propagate until to the fibre ends as shown in Fig. 3.3. In the LHCb Upgrade SciFi Tracker, the fibre end will be read out by SiPMs. Whilst on the opposite end of the fibre, a mirror will be intentionally attached to increase the light yield be read out by the SiPM [40].

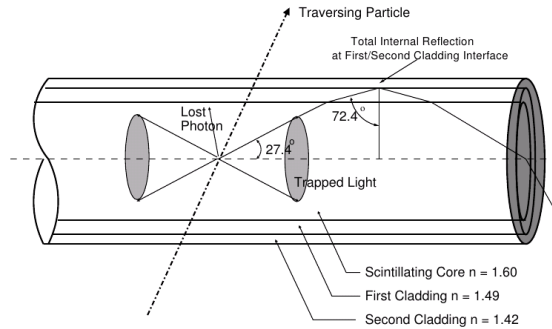


Figure 3.3: Fibre schematic showing the light production and propagation within the fibre thanks to total internal reflection. Taken from [21].

The scintillating fibres manufactured by Kuraray company<sup>1</sup> was chosen for the LHCb Upgrade SciFi tracker. Studies were carried out in order to reveal key properties such as the decay time, the emission spectrum of the fibre, the light yield, its radiation hardness, the benefit from the mirror as well as production quality [40].

The decay time of the scintillation light is 2.8 ns, while the mean propagation time of light along the length of the fibre is 6 ns/m. The light yield is expected to be 8000 photons/MeV or 1600 photons per mm of scintillating fibre [41].

The emission spectrum ranges from about 400 to 600 nm and with a maximum at 450 nm as shown in Fig. 3.4, fitting quite well with the wavelength-dependent photon detection efficiency (PDE) of the SiPMs as shown in section 3.5.4.

The radiation damage caused in fibres is described by complex processes of radical production, which form chromophores and degrades the transmission. These are dependent on many parameters such as dose, dose rate, the presence and diffusion of oxygen. The scintillation light yield has not been observed to degrade at the expected LHCb doses. A mirror at the end of the fibre placed to opposite side from the SiPM is necessary providing an adequate light output, particularly after irradiation [40].

### 3.4.2 Fibre Mats

Single scintillating fibres with diameter of 250  $\mu\text{m}$  are arranged into a staggered multi-layer fibre mat providing a sufficient light yield to the SiPMs. Studies have shown that a compromise between the constraints of low budget material and spatial resolution, six layers are required. A threaded winding wheel with a diameter of approximately 0.82 m produce these mats. In particularly, a layer of fibre is produced

<sup>1</sup>Kuraray Co., Ltd Kabushiki-gaisha Kurare is a Japanese manufacturer of chemicals, fibers and other materials.

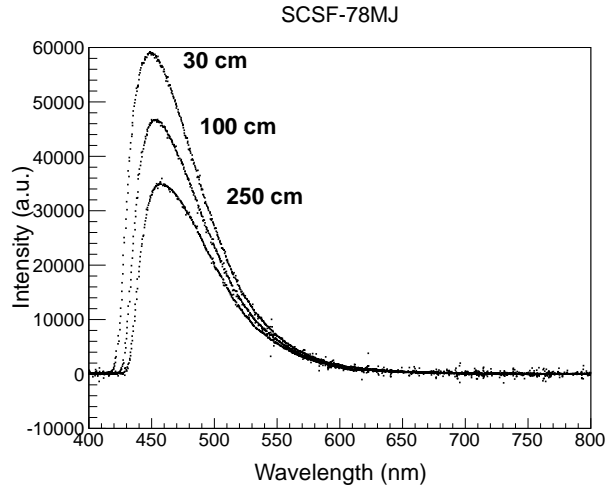


Figure 3.4: Wavelength spectrum for three different position from the SiPMs. Taken from [21].

by guiding the fibre into the grooves on the turning wheel with a pitch of  $275 \mu\text{m}$ . The remaining 5 fibre layers in turn follow their preceding as a positioning guide. Each layer is shifted by half the horizontal pitch with respect to the above forming a hexagonal packing structure as shown in Fig 3.5. In addition, 9 pin holes are made in the central groove on the winding wheel which during the winding process are filled with glue, producing precise alignment pins for the next production steps. For the sake of stability and protection, at the end of the winding process polyimide black foils are laminated on top and bottom of each fibre mat improving the light tightness. Polycarbonate pieces are glued on the read-out side of the mat facilitating the alignment of the fibre mats during the production of the modules. This also allows the attachment of the SiPMs to the fibre mat. Then the foil cast mat has to be cut to the right length. Finally, an aluminized mylar foil mirror is attached on the opposite side of read-out side to increase the light yield of the fibres as mentioned above.

The geometry of the fibre mats is constrained by several parameters. Thus, the width of each fibre mat was chosen to fully cover four SiPM arrays comprising 128 channel each. Considering tolerances, this corresponds to a total width of around 130.60 mm. Around 0.125 mm of each side of the mat is inactive due to the longitudinal cut, resulting in an active fibre width of 130.34 mm matching to the active region of the SiPM arrays.

Two groups of four fibre mats are positioned with the mirror sides in back to back topology resulting in a fibre module. Eventually, the SciFi Tracker needs 1024 fibre mats, in order to form three tracking stations necessary to cover the detector acceptance of the LHCb detector, which means 128 modules in total [34].

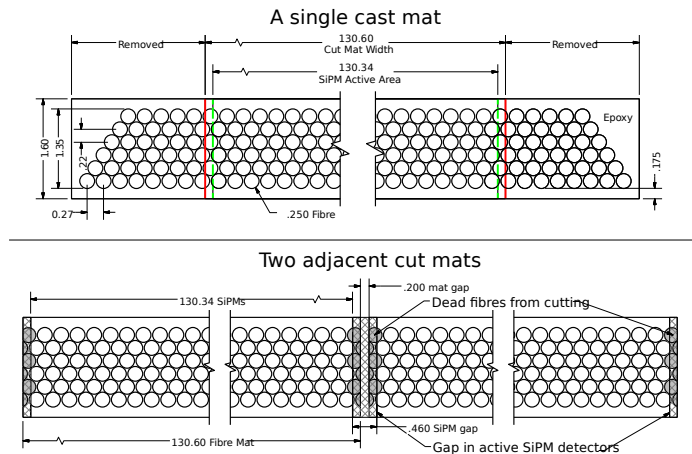


Figure 3.5: The top schematic shows a single cast fibre mat before performing a longitudinal cut. While, on the bottom two adjacent mats are shown after the mats have been cut to a width of 130.60 mm. The grey fibres indicate that SiPMs can not read out them, since they lose the majority of transmission light due to their cut. Taken from [21] [Modified].

### 3.4.3 Fibre Modules

The fibre mats are not stiff objects. Thus, they have to be sandwiched a two 2 cm high honeycomb cores and a single carbon-fibre reinforced polymer skin on both sides. A SciFi fibre module includes eight fibre mats, four aluminium endplugs, two half-panels made of a honeycomb core and carbon-fibre sidewall. Fig 3.6 shows a schematic view of the single module.

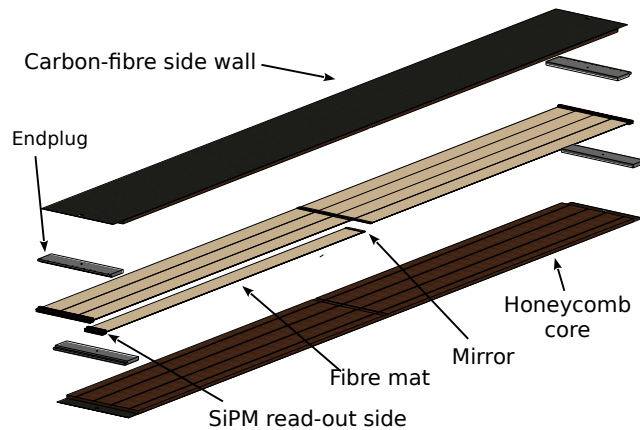


Figure 3.6: A view of module showing its components. Taken from [34] [Modified]

## 3.5 Silicon Photomultiplier (SiPMs)

The SiPMs consists of multiple APDs (Avalanche photo diodes) connected in parallel. They are widely used in high energy and medical physics, due to the following advantages.

- High gain.
- Fast response.
- High sensitivity.
- Insensitive to magnetic field.
- Small size.
- Low bias voltage.

### 3.5.1 Semiconductors

The SiPM is a semiconductor device. The operation principle of a semiconductor device is conceived using the band model of solids [42]. In this context, the discrete electron energy levels of individual atoms within a whole crystal are brought together in order to form energy bands. The lowest energy band partially or completely filled with electrons but never empty is known as "valence band". In this band the electrons are bound and therefore can not contribute in the conduction of current. Whilst the highest band is either partially filled or empty known as "conduction band". The gap between the top of the valence band,  $V_V$ , and the bottom of the conduction band,  $V_C$ , defines the energy band gap having a width of  $E_g = V_C - V_V$  [42] as shown in Fig 3.7.

Solids can be classified by the size of energy band gap.

- Insulators  
A material with zero conductivity has an energy band gap in the order of at least a few eV. Such an amount of energy can not be provided thermally at room temperature, so electrons can never reach the conduction band.
- Semiconductors  
In case that the energy gap of material is slightly bigger than the thermal energy which electrons bear in room temperature. This means that a small proportion of electrons can possess enough kinetic energy to move up to the conduction band. Therefore, these few electrons can induce a limited amount of current flowing when an external electric field is applied.

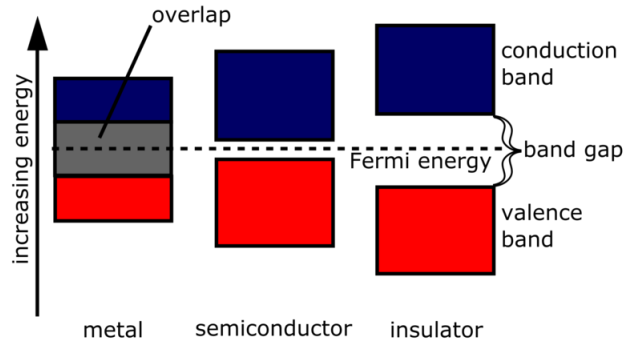


Figure 3.7: A band gap diagram showing the different sizes of band gaps for conductors, semiconductors, and insulators. The Fermi energy is defined as the highest occupied energy level of a material at absolute zero temperature and is placed between the conduction and valence bands. Taken from [43].

- Conductors

The conduction and valence bands are overlapping. Thus, as soon as an electric field is applied to the conductor then the electrons can readily acquire the small additional energy necessary to climb to the conduction band. The remaining energy in form of kinetic energy is used to contribute to the formation of electric current.

The semiconductors are further distinguished into **intrinsic** and **extrinsic** semiconductors, respectively. Intrinsic semiconductors stand for the case where the number of thermally generated electrons is equal to the number of holes. While extrinsic semiconductor stands for the case where impurities have been added to the semiconductor such that to contribute to either the excess of electrons or excess of holes. The extrinsic semiconductors are categorized in turn to p-doped and n-doped depending on their excess to holes or electrons. For instance, when impurities of arsenic are added to Si, each As atom serves as a **donor** providing a free electron to the crystal. In this case, the silicon will exhibit an excess of electrons and therefore convert silicon to a **n-type Si**. On the other hand, when impurities of boron are added to Si, each boron atom serves as an **acceptor** since it captures electrons from Si inducing thereby an excess of holes in the crystal. In such a case the silicon is converted to **p-type Si**.

### p-n junction

When the n-type semiconductor and p-type semiconductor material are coming in contact a density gradient is created, since the free electrons from the donor impurity atoms will diffuse in order to recombine with the holes of the p-type material leaving behind positively charged donor ions. Similarly, the free holes from the acceptor impurity atoms will diffuse in order to recombine with the electrons of n-type

material leaving behind negatively charged acceptor ions. This process creates an electric field across the junction, which stops eventually the diffusion. The region where the immobile charge carriers such as positive and negative ions are positioned is called "depletion region". When a free charge carrier placed in this region drifts out under the influence of the electric field of the junction. A schematic showing before the p-type and n-type semiconductor come together and afterwards is shown in Fig. 3.8. The electric field of the junction induce a built-in potential  $V_{bi}$  to be formed.

Applying the same voltage polarity on the p-n-junction sides, the holes from the p-side and the electrons from the n-side are forced towards to p-n-junction reducing the depletion region. This decreases the built-in potential barrier and facilitates the movement of the electrons across the p-n-junction. In this case, the p-n-junction operates in "forward bias mode". On the other hand, applying a reverse voltage polarity on the p-n-junction, the electrons and holes of n-side and p-side respectively are repulsed from the junction increasing the depletion region. The p-n-junction operates in "reversed bias mode".

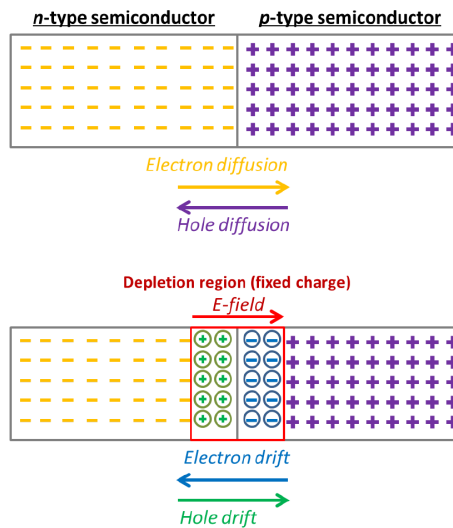


Figure 3.8: A schematic before and after merging the p-type with n-type semiconductor is shown. Taken from [44].

### 3.5.2 Avalanche Photo Diodes (APDs)

APD is a highly sensitive silicon photodiode. Exploiting the photoelectric effect, it is capable of converting the light to electricity.

An APD operates in reversed bias mode. In this case, the bias voltage applied is slightly above the breakdown voltage (see below). Operating in this mode, whenever a photon is absorbed then one electron-hole pair (charge carriers) is created. The generated charge carriers are separated under the influence of the electric field.

Thus, the very high electric field is capable of accelerating the charge carriers such that they can create secondary charge carriers in turn to develop an avalanche. Actually, a single photon can trigger an avalanche producing a signal of  $10^6 - 10^7$  electrons depending on the gain of the device. It turns out that the signal is independent of the primary number of photons inducing the given avalanche. At some extent, it is necessary to stop the avalanche allowing thereby the detector to recover. A dedicated "quenching" circuit lowers the bias voltage after a hit. During this recovering time until voltage returns to its initial value, the APD is insensitive for detecting any photon.

The typical quenching method is based on a series resistor. After triggering an avalanche, then a high current is flowing through the resistor, which in turn drops the voltage applied on the resistor stopping thereby the multiplication process. This method is known as "passive quenching".

A SiPM channel consists of multiple APDs in parallel. A typical structure of SiPM is shown in Fig. 3.9.

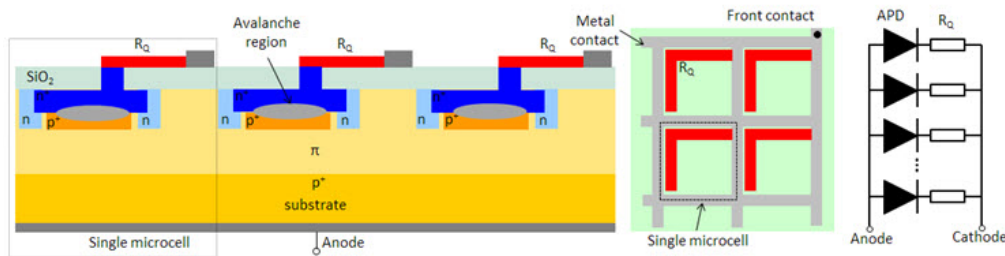


Figure 3.9: A schematic of a typical SiPM channel consists of multiple single micro cells, that is APDs including their quenching resistors and interconnections between them. Taken from [45].

### 3.5.3 Characteristic properties of SiPMs

#### Breakdown Voltage

The breakdown voltage ( $V_{bd}$ ) is considered as the minimum reversely applied bias voltage that results in a self-sustaining avalanche multiplication.  $V_{bd}$  is temperature dependent.

Thus, operational voltage  $V_{op}$  beyond the breakdown voltage is called overvoltage  $V_{ov}$  defined as follows:

$$V_{ov} = V_{op} - V_{bd}$$

#### Gain

The multiplication factor of an elementary charge  $e$  in the avalanche is defined as follows:

$$G = \frac{Q_{av}}{q} = \frac{U_{ov}C}{e}$$

where  $Q_{av}$  is the charge of a single avalanche produced,  $q$  is the elementary charge and  $C$  the capacitance of a single pixel of the SiPM. For a given type of SiPM at a given temperature, the capacitance of each pixel is constant. Therefore, for an operating voltage higher than the breakdown voltage, the gain is increasing linearly with the overvoltage.

### Cross Talk

Photons created in the avalanche can trigger a secondary avalanche in one or more adjacent pixels. The signal amplitude is one photo-electron. Opaque optical trenches between the pixels are added to reduce this effect.

### Photon detection efficiency

The probability that a photon arriving at the SiPM surface will trigger an avalanche is called photon detection efficiency. It depends on the following features [46]:

- **Quantum efficiency (Qe)** defines the probability that a photon penetrating in the SiPM is actually absorbed and subsequently converted in an electron/hole pair. Qe depends on the wavelength  $\lambda$  and the temperature  $T$ .
- The **trigger probability (Pt)** is the probability that the generated electron/hole pair can initiate an avalanche process. The Pt depends on the overvoltage, the wavelength  $\lambda$  and the temperature  $T$ . Increasing the overvoltage will increase the PDE. However, this will increase the noise as well.
- The geometrical efficiency or **fill factor (FF)** is the sensitive area of surface capable of detecting photons. Dead area due to the quenching resistor area and metal traces for signal routing positioned on the surface cover a part of the sensitive area and reduces the FF.

Combining the aforementioned effects, one arrives at the following formula:

$$PDE(V_{ov}) = Qe(\lambda, T) \cdot Pt(\lambda, V_{ov}, T) \cdot FF$$

### Dark counts

An avalanche can be triggered by thermally excited electrons even without presence of the light. This effect depends on the temperature, overvoltage, the impurities and the lattice defects. Lattice defects can be created by propagating neutrons through the silicon, hence the concern about the neutron fluence earlier. The probability of two avalanches from thermally excited electrons at the same instant and overlapping is small for sub-MHz rates. They can therefore be rejected by a single p.e threshold. However, large signals can be created through pixel crosstalk.

## After-pulses

Impurities and the lattice defects can create intermediate energy levels in the band gap. Carrier charges can be trapped and later released by the impurities. The results are delayed avalanches (after-pulses).

### 3.5.4 Hamamatsu SiPMs

SiPMs from Hamamatsu<sup>2</sup> are used in this study (HRQ 2015 and HRQ 2016 technology), for detecting the light generated by the fibres. In the following, the Hamamatsu HRQ 2016 is presented. It is composed of multichannel arrays consisting of 128 channels each. The channel pitch is  $250 \mu\text{m}$ . While its height is  $1.62 \text{ mm}$  necessary for covering all 6 fibre layers of a fibre mat. Each channel comprises 104 avalanche photodiode pixels with a pixel size of  $62.5 \times 57.5 \mu\text{m}$ . The size of each silicon die is capable of hosting an array of 64 channels ( $\approx 16 \text{ mm}$  width) as shown in Fig 3.10 due to the manufacturing yield of silicon. Thus, two dies have to be packaged into one SiPM array of 128 channels. Two dies are separated by a gap of  $220 \mu\text{m}$ . The SiPM arrays are mounted on a flex PCB cable which is connected to the front-end electronics. The characteristic properties of the two Hamamatsu SiPM versions at an overvoltage of  $3.5 \text{ V}$  are shown in the following table [47].

version	PDE	direct x-talk	delayed x-talk	After-pulse
HRQ 2015	47%[480nm]	4.5%	5.5%	6.5%
HRQ 2016	48%[450nm]	3%	2.5%	0%

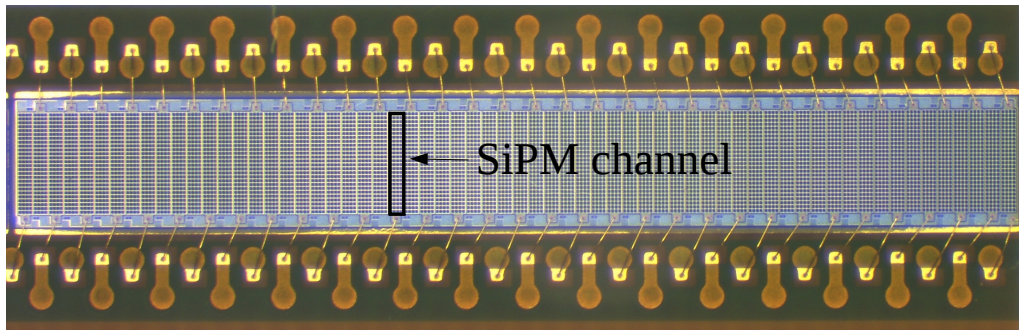


Figure 3.10: Photo taken under the microscope showing the 64 channels of a single die of a Hamamatsu HRQ H2016. Taken from [47].

<sup>2</sup>Hamamatsu Photonics K.K., 325-6, Sunayama-cho, Naka-ku, Hamamatsu City, Shizuoka Pref., 430-8587, Japan

## 4 PACIFIC

### Motivation

The SciFi detector need to be read out at 40 MHz. Thus, a dedicated front-end electronic ASIC so-called PACIFIC (Low Power Asic for the SCIntillator FIBres Tracker) is developed operating at this rate. The PACIFIC consists of 64-channels, each containing a pre-amplifier, a fast shaper, two interleaved integrators and three comparators used for digitization. The signal of each SiPM channel is digitized into 2-bits. This keeps the amount of data low in the PACIFIC front-end. The cluster algorithm detects real clusters related to particle tracks and suppresses single hits related to noise.

### CMOS technology

The Complementary metal-oxide-semiconductor (CMOS) technology is used for fabricating the PACIFIC chip. Thus, a brief description follows.

CMOS technology uses complementary pairs of p-type and n-type metal oxide semiconductor field effect transistors (MOSFETs). MOSFETs transistors are the basic constituents of modern integrated chips. They are sorted to p-type (P-MOS) and n-type (N-MOS) depending on the used doping profile. A typical N-MOS is implemented on semiconductor wafers implanting two n-doped areas in a p-doped substrate which serve as electrical contacts (drain and source contacts). On the surface intermediates between two contacts a metal layer is positioned (gate contact), which in turn is separated from the substrate thanks to an oxide layer as shown in Fig. 4.1. Once one applies a positive voltage on the gate, then an electric field is formed between the gate and silicon substrate. This electric field points perpendicularly through the gate oxide. The silicon oxide placed between substrate and metal serves as dielectric, whereas the gate and silicon substrate can be considered as the plates of a capacitor. The positively charged gate repulses the free holes of the opposite area of substrate resulting only negative ions to remain there. Since the ions are immobile and fixed in the lattice of crystal, they create a depletion region. However, by applying further higher voltage on the gate, then the gate starts to attract electrons from the substrate. When the voltage exceeds a certain threshold depending on the material substrate (impurity concentration) and gate oxide (depth, material) then a conductive channel is formed connecting the source with the drain. This channel formation allows a current flowing between drain and source when one applies voltage on drain-source as be can shown in Fig. 4.1.

Typically, in digital circuits the MOSFETs are operating as switches. While on the analogue circuits can be used as resistors and current sources when they are oper-

ating at the linear and saturation region as can be shown on the right of Fig. 4.1, respectively.

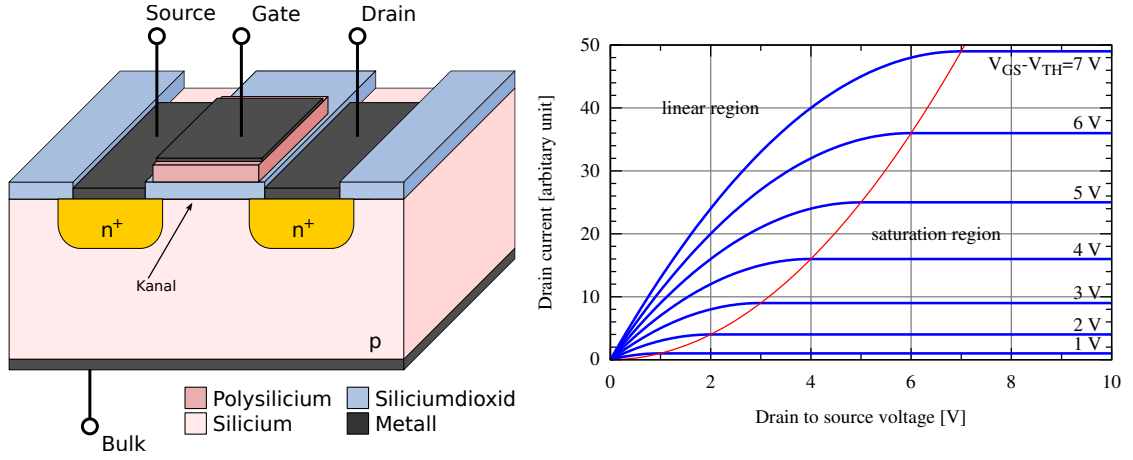


Figure 4.1: The physical structure of N-Mos Transistor (left) and its characteristic curve of I-V(right). Taken from [48] and [49]

## 4.1 PACIFIC specifications

The SciFi detector requires the PACIFIC chip to meet the following specifications [50] [38] [51].

- A low input impedance of  $\approx 50 \Omega$  to avoid affecting the timing behaviour of the SiPMs and increase the input current.
- A high bandwidth of  $\approx 250$  MHz is needed to handle the fast time component of the SiPMs signal.
- A configurable shaper implemented allows to suppress the slow time constant of the SiPM signals.
- An integration plateau  $\geq 15$  ns with less than 10% spill over.
- The integration should be implemented using two interleaved gated integrators with minimum dead time during acquisition.
- After the integrator each channel has three non linear thresholds used for the digitization of the amplitude information of the SiPM signal.
- In the end, the SciFi will consist of approximately 524k SiPM channels. Therefore, the huge number of channels necessitates the power consumption per channel to be kept as low as possible. Thus, the energy consumption should be less than 10mW/channel.

- The PACIFIC should provide the possibility for fine tuning the bias voltage of single SiPMs allowing a uniform gain across all the SiPMs channels.
- The different clocks inside the chip should be synchronized in order to ensure a uniform response among different channels and different operations.

### 4.1.1 PACIFIC evolution

Since 2013, several submissions of the PACIFIC chip versions have been sent to the foundry. The implemented PACIFIC versions are shown in Fig. 4.2 The starting point of PACIFIC development was "PACIFICr0" with a single channel current mode input stage and analog output. The next version "PACIFICr1" came to integrate additionally to the input stage of PACIFICr0 a shaper, a dual interleaved integrator and testing blocks for debugging. The following version PACIFICr2 used the features of its predecessor, however, it integrated additionally internal biasing and I<sup>2</sup>C digital configuration. It was the first chip having eight fully processing front end channels with digital output. The next versions, namely PACIFICr3 and PACIFICr4 are 64-channel full design prototype versions. and tested in this study and therefore their functions will be explained in detail in the next chapters [51]. The next PACIFICr5 version has already submitted in 2017, which replaces the single-ended output by SLVS differential outputs.

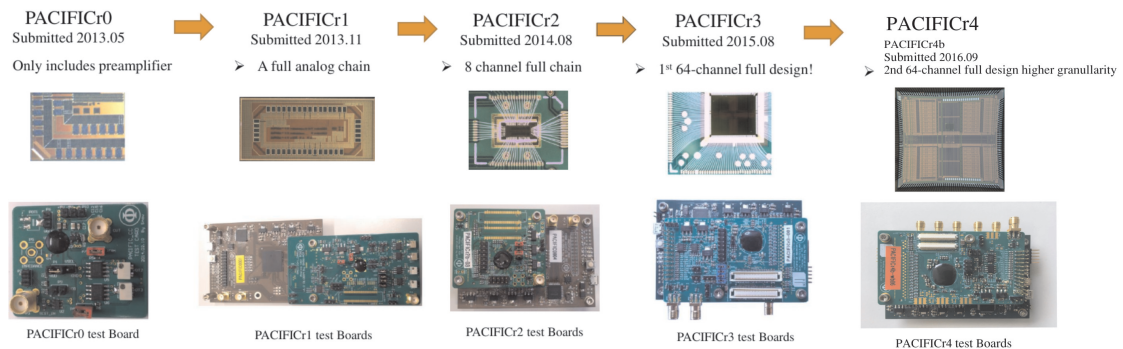


Figure 4.2: PACIFIC evolution.

## 4.2 PACIFIC Channel Structure

### 4.2.1 SiPM model

Before developing the PACIFIC front-end ASIC, an accurate model of the SiPM signal based on SPICE<sup>1</sup> was necessary. Providing thereby a prediction of features of the input signal going to the PACIFIC generated by different devices. Since the

<sup>1</sup>SPICE (Simulation Program with Integrated Circuit Emphasis) is a general-purpose, open source analog electronic circuit simulator.

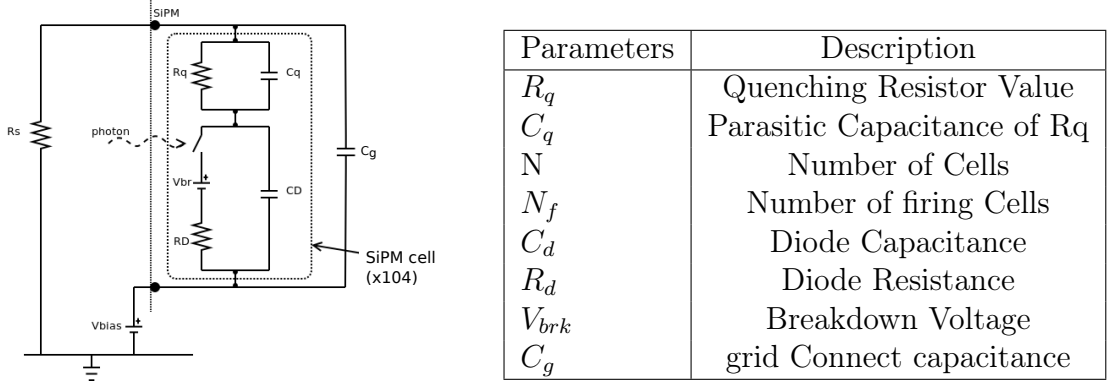


Figure 4.3: The SiPM simulated model (left) and the model parameters (right) [38].

vendors do not provide a detail-full information concerning the SiPMs key parameters used in the model, the parameters had to be measured in the lab.

The model parameters as well as the analogue circuit used for the simulations are shown in Fig 4.3.

Thus, two important equations can be extracted from this model which allow to adjust the time constants of the SiPMs predicted by the model to the measured ones. The first equation models the slow time constant of the SiPMs using the following parameters [51]:

$$\tau_{SiPM_{slow}} = R_q \times (C_q + C_d)$$

While the second equation models the fast time constant of the SiPMs as follows:

$$\tau_{SiPM_{fast}} = R_{load} \times (C_d N_{pix} + C_g)$$

where  $R_{load}$  is the input resistance of the input stage around 250Mhz while the other parameters are explained in the Table of Fig. 4.3.

The model and the measurements gave the following values for the Hamamatsu HQR 2015 and H2016 used in this study [52] [47]:

	Parameters	HQR 2015	HQR 2016
Model [Barcelona]	$\tau_{fast}$	0.72ns	0.68ns
	$\tau_{slow}$	34.76ns	50ns
Experiment [EPFL]	$\tau_{fast}$	<1ns	< 1ns
	$\tau_{slow}$	40ns	50ns

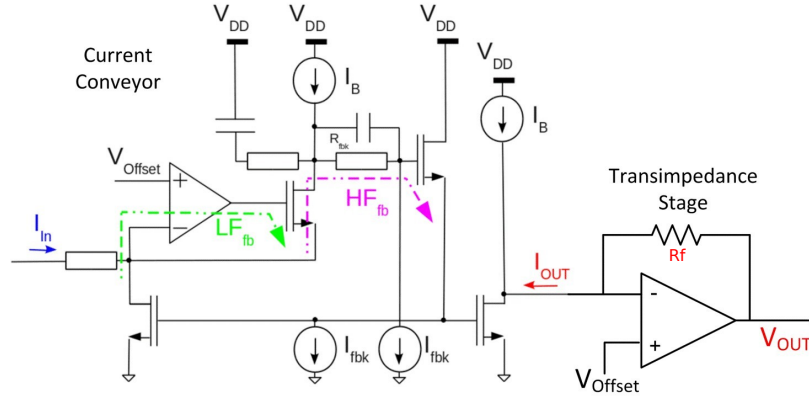


Figure 4.4: The current conveyor and the transimpedance amplifier. Taken from [38]

### 4.2.2 Input Stage

The input stage is realized having a current conveyor (amplifier with unity gain) based on two feedback loops and a transimpedance amplifier as shown in Fig. 4.4. A Low Frequency feedback loop ( $LF_{FB}$ ) is implemented using a virtual short circuit of a folded cascode operational transconductance amplifier dedicated to control the dc voltage ( $V_{Offset}$ ) of the input anode of each SiPM channel. Thus, the current anode voltage control is capable of tuning the bias voltage of SiPM within the defined range of around 100-800 mV with an approximate step of 50 mV as shown in Fig. 4.5. Ensuring thereby the gain uniformity among the channels. Whereas, the high Frequency feedback path ( $HF_{FB}$ ) is implemented with a common-gate regulated cascode configuration such that to keep the input impedance  $R_{load}$  constant over the operating bandwidth (250Mhz) avoiding the modification of the fast time constant  $\tau_{SiPM_{fast}}$  of SiPMs. Moreover, the gain of the current conveyor is configurable in order to fit to the certain SiPM connected.

The current conveyor is followed by a transimpedance amplifier where the current of SiPM is converted into a voltage using the relation:

$$V_{out} = I_{out} \times R_f$$

where  $V_{out}$  is the output voltage,  $I_{out}$  the output current and  $R_f$  the feedback resistor of transimpedance stage as shown in Fig 4.4. There are four different gain settings, the highest gain was preferably used in this study for single cell calibration.

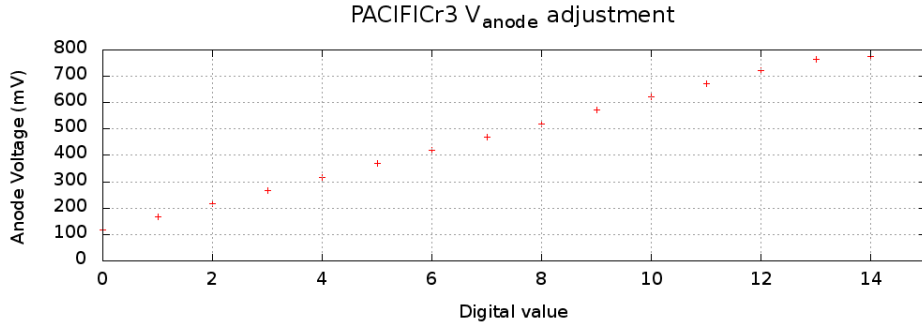


Figure 4.5: The voltage anode adjustment ranges between 100 to 800mV with an approximate step of 50 mV. Taken from [51].

### 4.2.3 Shaper Stage

The signal shape depends on the position of light generation in the fibre mat due to the reflection from the mirror as well as the SiPM recovery. The shape of the signal for different interaction points of an incoming electron of beta source on fibre mat is shown in Fig. 4.6.

The slow time constant  $\tau_{SiPM_{slow}}$  given from the SiPM model describing the Hamamatsu SiPMs indicates that the signal is going to be distributed over more than one bunch crossing. Therefore, a configurable shaper is necessary in order to cancel the long tail of SiPMs prior integration. By means of pole zero cancellation circuit, a suppression of the  $\tau_{SiPM_{slow}}$  and cancellation of the  $\tau_{SiPM_{fast}}$  time constants of SiPMs is possible. Owing to an adjustable tunable pole zero cancellation circuit, the shaper is flexible allowing to operate with different time constant of different types of SiPMs.

To ensure that the DC baseline before and after shaping should be the same. An additional DC feedback loop has been added after the shaper in order to keep the baseline constant. Since any discrepancy between them during the operation will result in a different integration output.

### 4.2.4 Gated Integrator

The shaper stage is followed by two interleaved gated integrators. The integrator is based on Miller OTA [53]. Their implementation is shown in Fig. 4.7. They apply an integration of the input voltage over the time as described by the following formula:

$$v_{out}(t) = -\frac{1}{RC} \int_0^t v_{in}(t)dt - V_{cm}$$

The two reset switches of each integrator provide the capability of setting its value of the input and output voltages to the reference voltage, respectively. While the

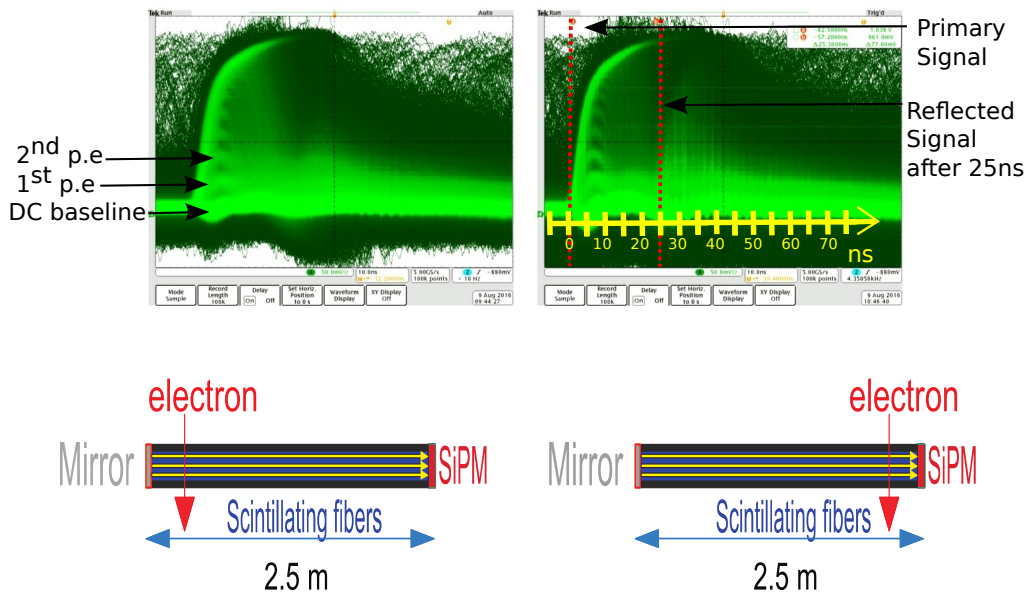


Figure 4.6: For two different cases of positioning a beta source close to the mirror (left) and close to SiPMs (40cm) (right) resulting in a different shaped signal of PACIFIC. Close to SiPMs a reflected signal is observed coming after 25ns validating the rule of the mean propagation time of light along the fibre is 6 ns/m. On the left figure, the DC baseline, 1<sup>st</sup> and 2<sup>nd</sup> p.e have been pointed starting from low to high voltage values.

value of capacitor and resistor define the maximum value of the output signal. The two interleaved integrators are alternatively activated and reset at a 20 MHz rate. This allows while the first integrator is integrating the other resets avoiding any dead time during acquisition. Three comparators digitize the integrator output each 25 ns just before the switching between two integrators occurs. Since the integrator switching lasts some time while neither one nor the other integrator can integrate the signal, this induces a small loss of the signal integration during the switching.

### Trimming mechanism

The DC baseline of the two integrators within one channel are not exactly the same, due to fabrication mismatch. This in turn for the same input signal can induce different digitization output for different integrators. Therefore, to cancel this offset, two trimming circuits have been added at the integrator's reference voltage per channel. The trimming circuit is implemented using a current output DAC(Digital to Analogue Converter) and some current mirrors dedicated to feeding the current to any direction allowing a positive or negative movement of the initial DC level.

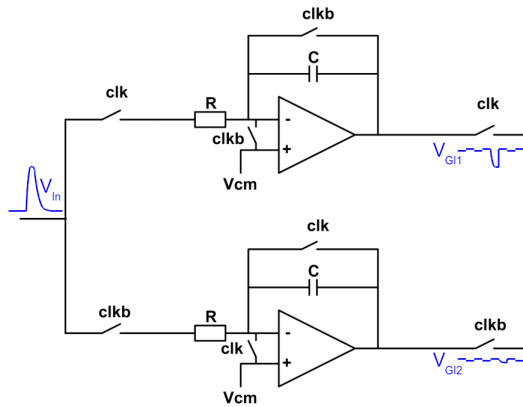


Figure 4.7: The interleaved gated integrators. Taken from [51]

### 4.2.5 Track and Hold

After integration, a track-and-hold circuit is used to merge the two gated integrators output to a single signal and saving the charge into a common capacitor. The implementation of track and hold circuit is based on large capacitors reducing a potential mismatch between them as well as switches as shown in Fig. 4.8.

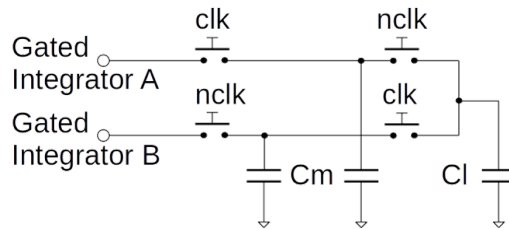


Figure 4.8: The track and hold circuit. Taken from [51]

### 4.2.6 DC Correction (Common Mode Control)

At the output of track and hold a closed loop feedback had been added in order to compensate the channel to channel variations in the PACIFICr3. It was a low speed loop dedicated to ensuring that the DC level before the comparators is equal to the reference voltage. However, this mechanism was not capable of solving the problem as this study is going to present resulting in its removal from PACIFICr4 design.

## 4.2.7 Digitization

The last part of the processing chain of a PACIFIC channel is the digitization implemented with three comparators having adjustable thresholds. The hysteresis of the comparator is  $\approx 10\text{mV}$ .

In PACIFICr3, the thresholds of the comparators were set thanks to a multiplexer selecting one out of the three different groups of threshold DACs common for all the channels. This serves to deal with any system non-uniformity. These threshold DACs are generated by the current mirrors referenced to the reference voltage of PACIFIC ( $V_{\text{refDCFB}}$ ) as shown in Fig. 4.9. This voltage reference is used across the analogue processing chain in order to keep constant the DC value at the output of the different blocks. One threshold DAC of PACIFICr3 was 7-bit while the other two were 6-bit, respectively.

In PACIFICr4, the generation of comparator thresholds is independent of the reference of PACIFIC ( $V_{\text{refDCFB}}$ ). Beside of common thresholds DACs for all 64 channels, a new option added including local thresholds for each channel individually as shown in Fig. 4.10. The PACIFICr4 version was designed integrating three of 8-bit threshold DACs in each channel in order to generate the threshold values. The output of the three comparator outputs is encoded into 2 bits as follows:

- $0_b00$  if no comparator is fired
- $0_b01$  if one comparator is fired
- $0_b10$  if two comparators are fired
- $0_b11$  if three comparators are fired

Thresholds should be sorted with an increasing order, ensuring that when a higher comparator has been fired then the lower comparators should have also been fired.

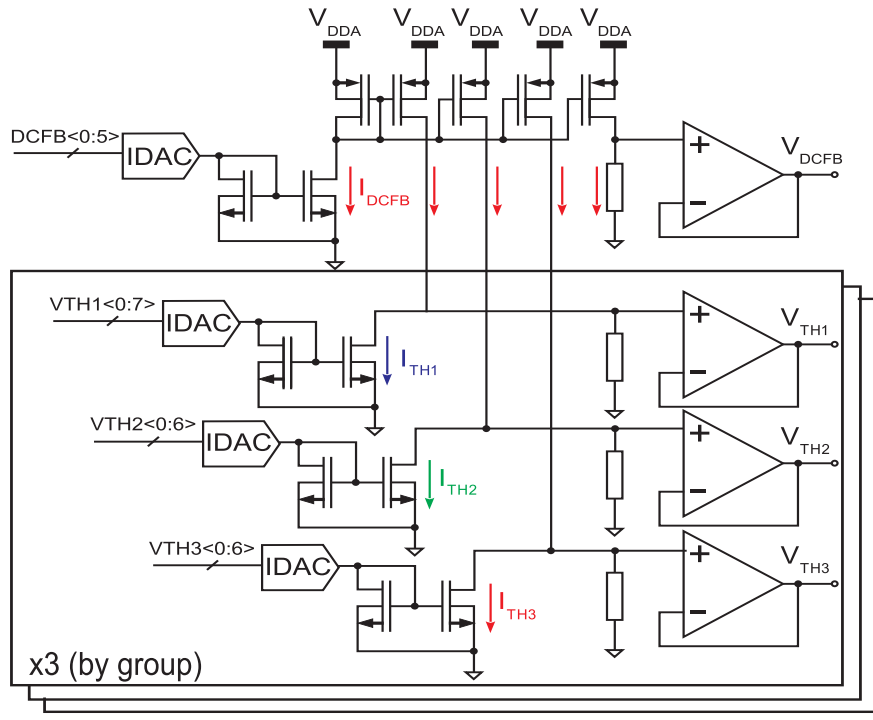


Figure 4.9: The generation of three groups of common thresholds for 64 channels. Taken from [51] [Modified].

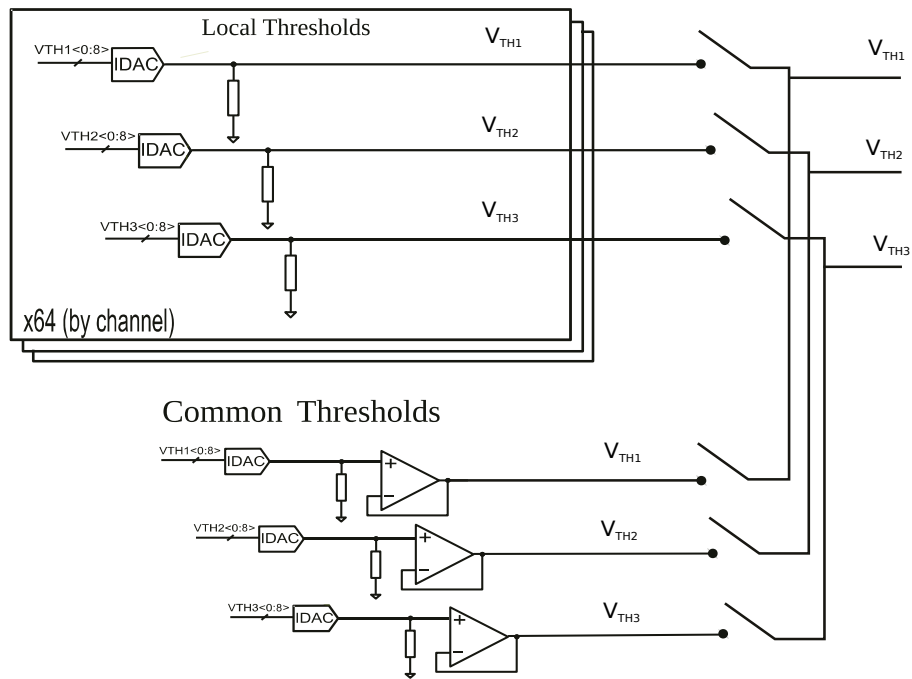


Figure 4.10: Selection between common and local threshold DACs for each channel [51] [Modified].

## 4.3 Slow Control

The operational parameters of each stage of the ASICs are configurable via  $I^2C$  (Inter-Integrated Circuit) interface. A list of configured operational parameters are shown above:

1. Input stage gain selection depending on the operation mode. For the calibration purpose the highest gain is used.
2. The pole zero cancellation circuit parameters adjusting the shaper to the given SiPMs
3. Input anode voltage control which is dedicated to ensure the uniform gain response among SiPMs.
4. Integrator trimming allowing to align the DC baseline between two integrators within one channel.
5. The comparator thresholds settings leading to the digitalization of analogue amplitude information.

The first two features can be configured globally for all 64 channels. While the next three are individually configured for each channel. However, the last feature can be selected between the common configuration for 64 channels and separately for each channel individually.

The slow control is used also for testing the features of PACIFIC. It is possible to debug the output of the analogue and digital part of chip as shown in Fig. 4.11.

The analogue output signals are available for debugging the preamplifier, the shaper and the track and hold output of each channel, separately.

An external digital signal can be injected in the serializer block for testing the serialization output and digital links.

For the characterization of PACIFIC, a calibration input is available by means of injection of electrical signals controlled by slow control registers. This calibration input can be injected with two possible ways. The first way is with internal signal injection where the signals can be injected into multiple channels at the same time. An external signal can be injected to only one channel at a time.

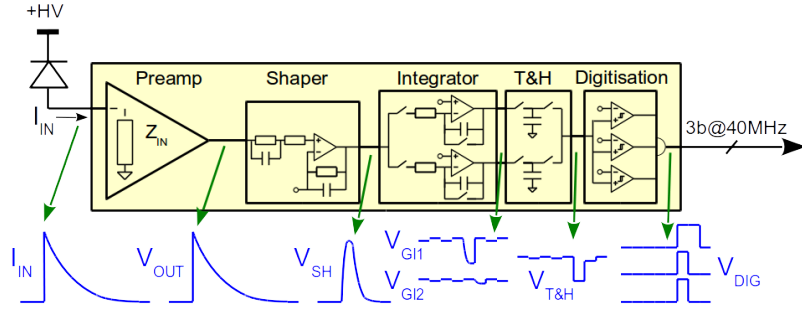


Figure 4.11: The available output signals for debugging of the analogue and digital part of PACIFIC. At the output of every two channels, an encoder and serialization block is included encoding the three outputs of the channel comparators to two bits. Taken from [51].

## 4.4 Clusterization

A charged particle passing through the fibre mat deposits part of its energy via ionization to scintillating fibres. Then, in turn, part of deposited energy is converted to scintillation light which is reflected inside the fibre in order to end up to the end of fibres, where the SiPMs are attached. This light is detected by the SiPM and results in an electrical signal measured by the PACIFIC. Depending on the optical cross talk between the fibres, the light generation is distributed over multiple scintillating fibres which in turn can shine more than one SiPM channels forming a cluster as shown in Fig. 4.12. By comparing the signal in the channels to certain thresholds the PACIFIC can reconstruct a cluster.

The thresholds are described in terms of DACs<sup>2</sup> (Digital to Analogue Converter) and they have a physical interpretation, such that the thresholds can be set in terms of photo-electrons. A calibration of each SiPM channel is necessary, allowing us to know the relation between the threshold DACs of the comparators and photon-electrons (p.e).

After calibration, in order to set correctly the thresholds, two different requirements have to be considered. First, the thresholds should be set high enough in order to reject the dark noise of SiPMs. Second, they should not be too high decreasing the hit efficiency. A compromise between them was considered in order to find the optimum threshold settings.

The PACIFIC is using three thresholds for the digitalization of analogue amplitude information. They are defined as *low*, *middle* and *high*. To begin constructing a cluster one of the following minimum requirements has to be met:

- The amplitude of the analogue signal of one channel has to pass the high threshold (channel three as shown in Fig. 4.12).

<sup>2</sup>Each DAC value is 3 mV

- The amplitude of the analogue signal of one channel has to pass the middle threshold (channel nine in Fig. 4.12) and in addition any of its two neighbours has to pass the low threshold (channel 10).

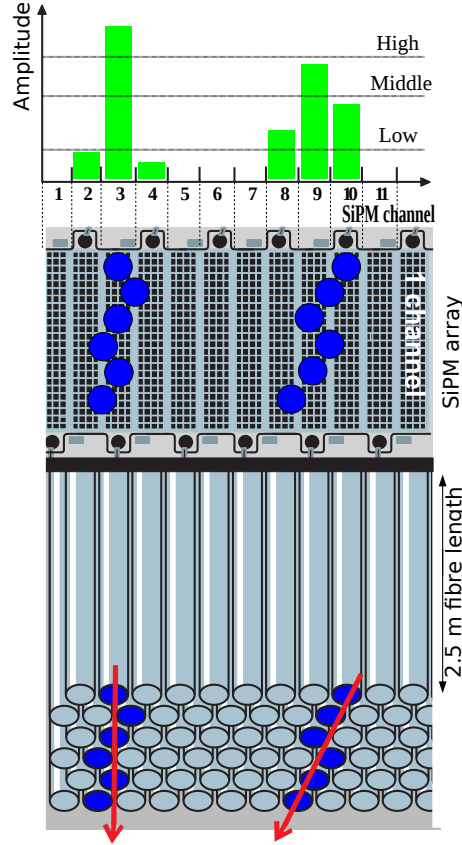


Figure 4.12: The two different cases where a particle track is indicated with red color can induce clusters fulfilling the minimum requirements as shown on the top of figure.

### Barycentre Weighting

In order to calculate the barycentre of the cluster using PACIFIC thresholds, a weighting of the thresholds is necessary based on the full 12-bit reference data coming from simulations studies and test beam data [54]. The comparison studies have shown that for thresholds of low = 1.5, middle = 2.5 and high = 4.5 photo electrons (p.e), the weights are 2,4 and 12 at the mirror, respectively. Then, the barycentre position of the n-th cluster in the PACIFIC is calculated using the following formula [54]:

$$\bar{x}_n = \frac{\sum_{i>Low} x_i w_i}{\sum_{i>Low} w_i}$$

## 4.5 Threshold Scan

In order to further characterize the PACIFIC, a so-called threshold scan is performed. In this scan, the amplitude of the incoming signal is compared to a single threshold which varies over a wide range. At the beginning this threshold is set to a low DAC, corresponding to a low voltage. A large number of events are recorded within a fixed time window. Then the following ratio is calculated:

$$n[DAC] = \frac{\text{Number of events the comparator has fired}[DAC]}{\text{Number of sent events}[DAC]}$$

where  $n[DAC]$  is scaled to one and defined as the `overThresholdRatio` for the certain DAC value.

For low thresholds this ratio is always equal to one, since the signal has a constant offset, the DC baseline, causing it to exceed the threshold. In the next step the threshold is increased by one DAC and the ratio is calculated again. It decreases once the threshold becomes larger than the DC baseline. During the scan, light is injected into the system, producing a signal that is added to the baseline. Without this additional signal the ratio would drop to zero. Instead, it follows a smeared-out step function so-called "S-curve", where each step corresponds to a number of photons arriving at the SiPMs. An example of this is shown in Fig. 4.13. The first plateau after the baseline has a ratio of approx. 0.7, meaning that in 70 % of the recorded events the threshold was exceeded, due to sufficiently large number of photons arriving at the SiPMs. In this case, at least one photon has been detected. Once the threshold is increased beyond a certain point, two or more photons are necessary. Since events with at least two photons occur less often, the rate decreases again.

In case of an ideal detector and electronics where there is no noise. A threshold scan would give rise to a perfect step function, with steps occurring at the photo-electron amplitudes. However, the steps are smeared by electronic noise superimposed on the input signal. The amplitude of the input signal is injected constantly to the system follows a Gaussian distribution due to the noise. Therefore, the probability of that signal to exceed the threshold can be expressed as follows [55]:

$$P(V > V_{Th}) = \frac{1}{\sqrt{2\pi}\sigma} \int_{V_{Th}}^{\infty} e^{-\frac{(V-\mu)^2}{2\sigma^2}} dV$$

where  $V$  is the current input voltage amplitude of the signal, while  $\mu$  and  $\sigma$  are the mean voltage amplitude and RMS noise voltage of the signal.

The smeared-out step function so-called "S-curve" due to the noise is described by the next formula [55]:

$$n[DAC] = \frac{1}{2} \left[ \text{erf} \left( \frac{[DAC] - \mu}{\sqrt{2}\sigma} \right) \right]$$

where in this case the  $\mu$  and  $\sigma$  are representing the same quantities as described above but now they are given in terms of DACs.

After differentiation of the error function, a Gauss distribution is observed. The width of the gauss distribution gives the noise in terms of DACs. In this study, both erf function and Gauss fit used in order to extract the steps of S-curves or alternatively the peak positions of differential S-curves. Mainly, a peak finder algorithm is used to find peaks and to fit a Gaussian to them.

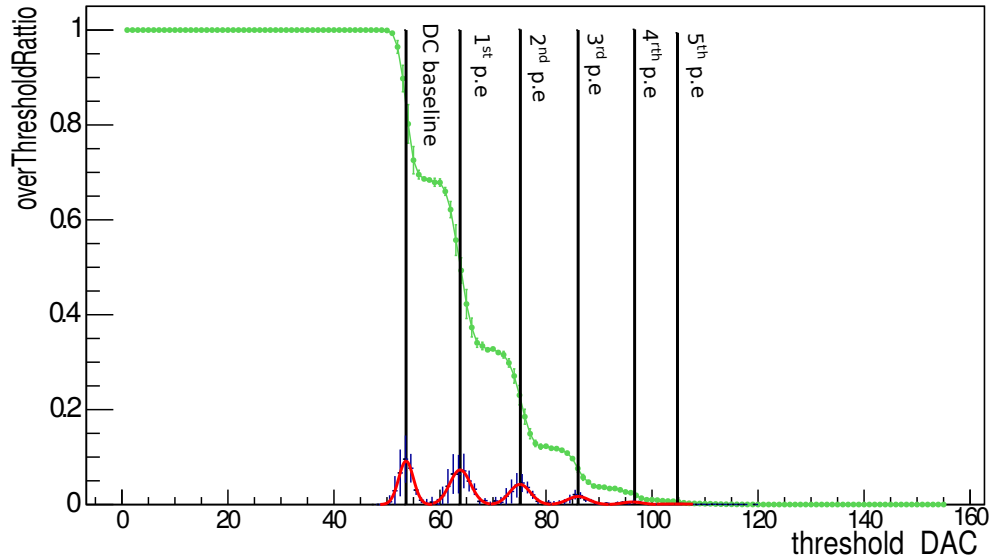


Figure 4.13: A typical S-curve (green) and its differential (red) are shown for channel 37 of PACIFICr4. The perpendicular lines (black) intersect the S-curve on the transition positions or alternatively on the peak positions of differential S-curve pointing the corresponding threshold DAC. Starting from left to right, the DC baseline, 1<sup>st</sup>, 2<sup>nd</sup>, 3<sup>rd</sup>, 4<sup>th</sup> and 5<sup>th</sup> p.e (photoelectrons) are shown.

# 5 PACIFICr3 characterization studies

## 5.1 Motivation

In this chapter the calibration routine is described. So, the DC baseline is adjusted in order to achieve a uniform response across all the channels and the integrators. A delay scan is performed in order to investigate the impact of the arrival of the signal with respect to the integration window on the observed gain. Combined with the DC baseline uniform response, the uniform gain response of SiPMs is achieved by tuning the overvoltage of each channel. Once the uniformity has been accomplished then a calibration of the threshold DACs is performed. This allows to extract the threshold settings that the clusterization algorithm needs in order to yields correct results.

The setup that is used for these measurements is presented.

### 5.1.1 Light Injection System

A light injection system is used in order to calibrate the SiPM gain. It provides a uniform illumination of the SiPMs, which is crucial for the calibration procedure. The light injection system is based on the vertical-cavity surface-emitting lasers (VCSEL). It is configurable from a Lab PC allowing to change the modulation current of diode achieving different light intensities. A red light pulse with a width of 5 ns is generated thanks to an internal trigger received from a FPGA located on the same PCB board as the PACIFIC.

The light pulse is guided through an optical fibre into aluminum bar. A scratch along the fibre in the light bar allows a nearly uniform distribution of light. The aluminum bar is positioned into the polycarbonate endpiece of fibre mat. The SiPMs Hamamatsu HRQ 2015 operating at 3.5 V overvoltage are attached on the other side of polycarbonate endpiece such that to detect the light from the light bar. The output of the SiPMs is processed and digitized by the PACIFIC and in turn sent it to the FPGA and the Lab PC. An overview of the light injection system is shown in Fig. 5.1.

The FPGA applies the clusterization algorithm on the output of PACIFIC. Moreover, it configures the PACIFIC. A delay unit intermediates between light injection system and FPGA, however, its utility will be explained in section 5.3.

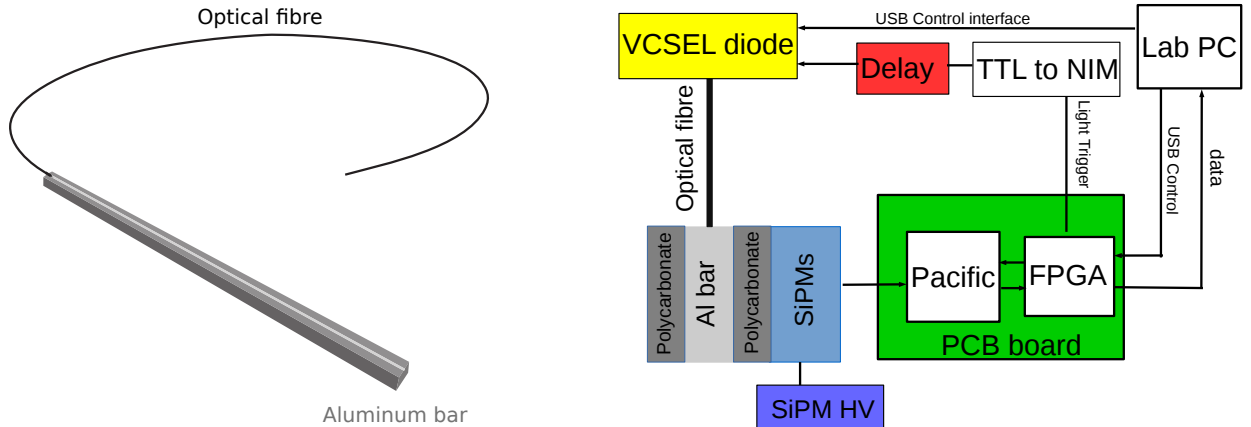


Figure 5.1: The aluminium lightbar with the optical fibre glued into one side (left) and the experimental setup dedicated for the SiPM calibration. (right).

### 5.1.2 Beta source setup

A beta source setup is needed for conducting studies of the clusterization algorithm and the asynchronous arrival of the signal with respect to the integration window of the PACIFIC.

It is realized using an external trigger scintillator positioned underneath the fibre mat. This trigger uses a scintillation bar with dimensions  $1 \times 1 \times 17 \text{ cm}^3$  in order to detect the traversing particles from the beta source passing through it. Thus, the generated scintillation light is travelling along the bar in order to be detected by two single SiPMs as shown on the left side of Fig. 5.2. Dedicated electronics are used for reading out the SiPMs on each end, including an adjustable amplifier and threshold discriminator. Moreover, two SiPMs allow to select their coincidence signal reducing thereby the number of fake triggers.

The output of the trigger is driven to the FPGA. A delay unit intermediates between the trigger and the FPGA, its utility will be explained further in section 5.4. The SiPMs Hamamatsu 2015 operating at overvoltage of 3.5 V and are attached on the other side of the polycarbonate endpiece. The generated light from the fibre mat is detected by SiPMs and their output is processed by the PACIFIC and in turn sent it to the FPGA and the Lab PC as shown in Fig. 5.2.

The light generated in the fibre mat is due to the electrons coming from a  $^{90}\text{Sr}$  (3.7 MBq) source positioned on the fibre mat close to the mirror. The  $^{90}\text{Sr}$  is a radioactive isotope having a half-live time of 28.8 years while its decay energy is 0.546 MeV. It undergoes a  $\beta^-$  decay into Yttrium-90, which in turn decays into the stable Zirconium-90, the anti-neutrino and an electron with energy of 2.28 MeV:



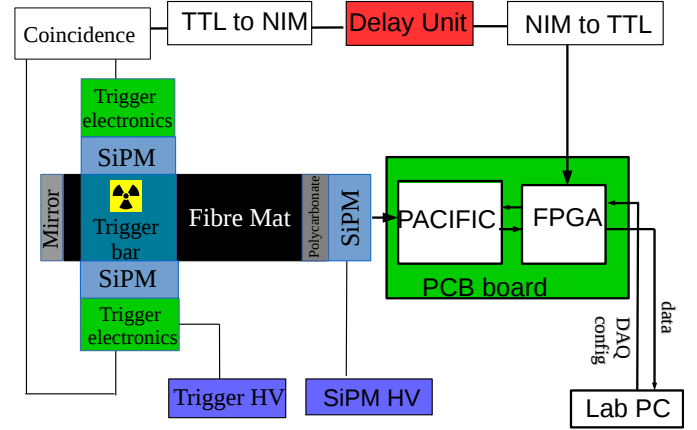
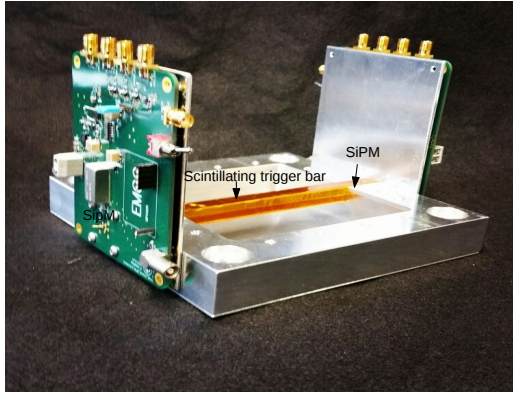


Figure 5.2: The trigger is shown(left) and the beta source experimental setup (right).

## 5.2 DC Baseline variation of the integrators

The DC baseline position for PACIFICr3 is defined as the threshold DAC value where the first transition occurs starting from the right side of a S-curve plot as shown in Fig. 5.11.

The DC baseline variations can induce a different digitization output for the same input signal. Thus, it is necessary to perform a uniformity test to determine the DC baseline position for the following cases.

1. DC baseline differences across the channels for two PACIFICr3 ASICs
2. DC baseline differences between two integrators within the same channel
3. DC baseline difference for different operating condition of PACIFICr3 within the same channel.

In the aforementioned cases, DC baseline differences can be observed. The correction mechanisms of the PACIFIC such as trimming and common mode control are used. A comparison of results before and after applying those mechanisms are presented in order to evaluate their capability of ensuring indeed a uniform response of PACIFIC.

### 5.2.1 DC baseline difference for two PACIFICr3 ASICs

#### Mismatch between ASICs

The channel to channel variations due to the fabrication process induce a non uniform response between the channels before the comparators. This means that the DC baseline position from channel to channel varies. The DC baseline positions are expressed in terms of DACs. Thus, the DC baseline distribution of 64 channels of comparator 1 before applying any correction mechanism are shown in Fig. 5.3 for

two PACIFICr3 ASICs. The mean value and RMS of DC baseline distribution of 64 channels for the ASIC 1 and ASIC 2 are displayed in Table 5.1. It turns out that these two PACIFICr3 ASICs exhibit different mean value of DC baseline distribution for the 64 channels. A small difference is indeed expected to occur since each PACIFIC is slightly different from the other due to the fabrication process. The smaller the difference is the smaller the mismatch between two PACIFICr3 ASICs is. The RMS shows the mismatch between the channels of each PACIFICr3 ASIC. The smaller the RMS is the smaller the mismatch between the channels of the certain PACIFIC is.

### Common Mode Control (CMC)

Thus, in order to cancel out the difference of DC baselines among the channels, the so-called CMC is applied in order to shift the DC baseline of each channel and in turn equalize it to the reference DC baseline of the chip. The mean value and RMS value of DC baseline distribution of 64 channels after enabling CMC for the ASIC 1 and ASIC 2 are displayed in Table 5.1. An improvement of uniformity of DC baseline across the channels is observed as the RMS decreases compared with the case of no alignment. However, there is still room for improvement concerning the alignment of the DC baseline of 64 channels since a maximum deviation from the mean value of around 8 and 7 DACs for ASIC 1 and ASIC 2 are observed as shown in Fig. 5.4.

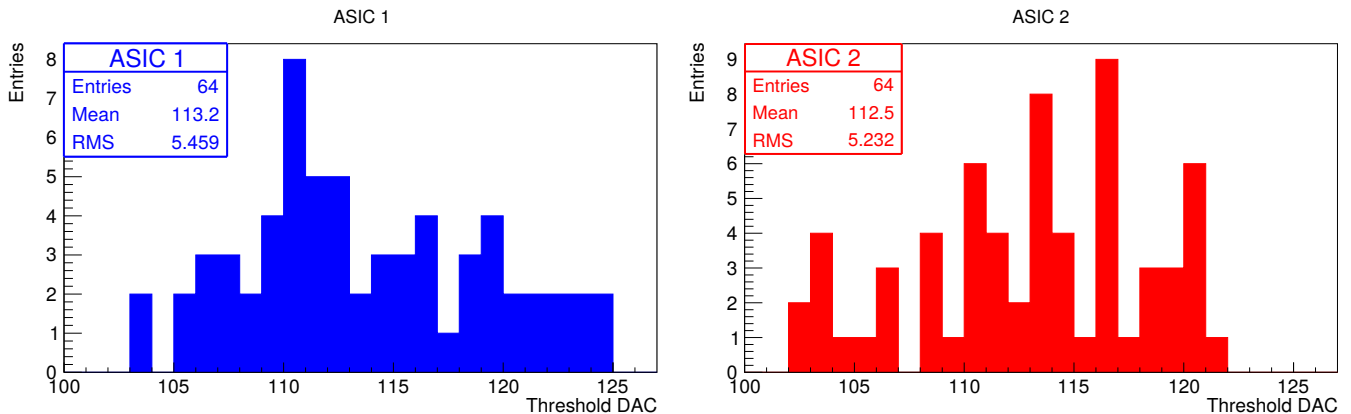


Figure 5.3: The DC baseline distribution of 64 channels for two PACIFICr3 ASICs without any alignment.

### Trimming

In order to align the DC baseline of 64 channels individually, the CMC is disabled and it is necessary to use the remaining available correction mechanism, namely trimming (described in 4.2.4). However, before shifting the DC baseline of each channel by means of trimming mechanism, one has to calibrate the trim DACs with

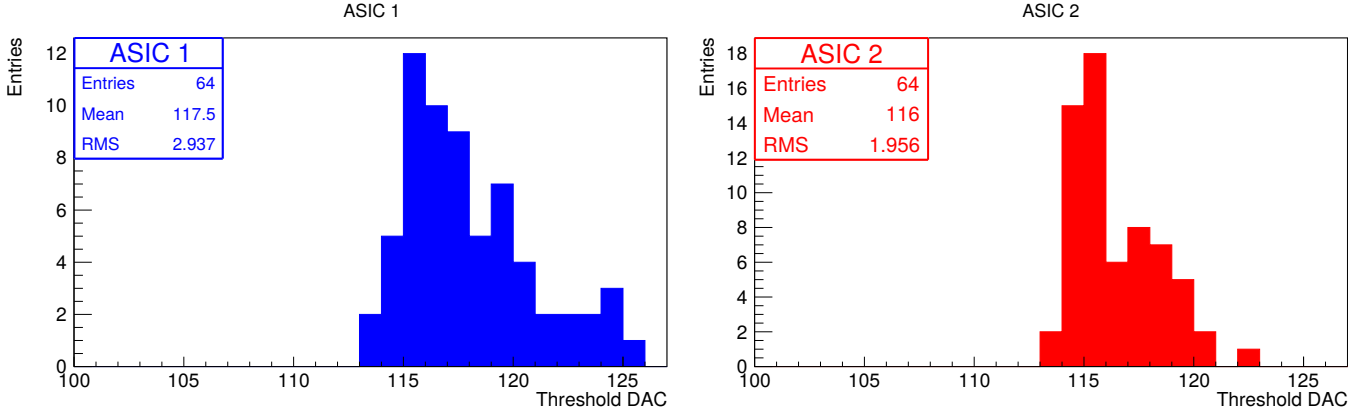


Figure 5.4: The DC baseline distribution of 64 channels for two PACIFICr3 ASICs after enabling CMC.

	ASIC 1		ASIC 2	
	Mean	RMS	Mean	RMS
No alignment	113.2	5.459	112.5	5.232
CMC enabled	117.5	2.937	116	1.958

Table 5.1: The Mean DC baseline and RMS for two PACIFIC ASICs without alignment and after enabling CMC.

respect to the threshold DACs. Since it is necessary to know by changing the trim DAC value how much in practice the shift of the DC baseline position in terms of threshold DACs is. To do so, a series of measurements to determine the DC baseline for each channel and each comparator by changing the trim DAC value have been conducted. Since the function between trim DAC and DC baseline position is linear. The given points are fitted with a linear function which gives a slope and an offset for every channel. For clarity reasons, this is shown only for comparator 1 for 16 channels in the left plot of Fig. 5.6. The right plot shows a histogram filled with the slopes of these channels. In the next step the mean slope and offset of all 64 channels is calculated for each comparator. Eventually, the mean and offset of three comparators is calculated and used later for auto-alignment of the DC baseline of 64 channels.

Once the DC baseline position for each of the 64 channels and 3 comparators is known before any alignment, then their mean DC baseline position can be calculated. Thanks to the given mean slope and offset, each separate channel DC baseline can be trimmed analogously towards this mean DC baseline value by using the correct trim DAC value. However, due to the ASIC mismatch as explained above, the calibration of the trim DAC has to be done for each PACIFIC individually. The slopes and offsets are unique for each PACIFIC. After applying trimming an alignment of  $\pm 2$  DAC is possible as it can be seen in Fig. 5.5.

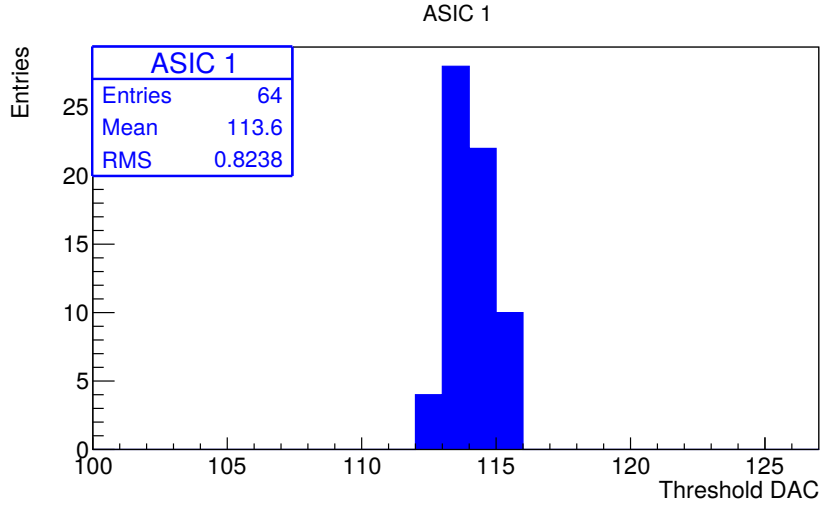


Figure 5.5: The alignment of DC baseline of 64 channels of comparator 1 after applying trimming.

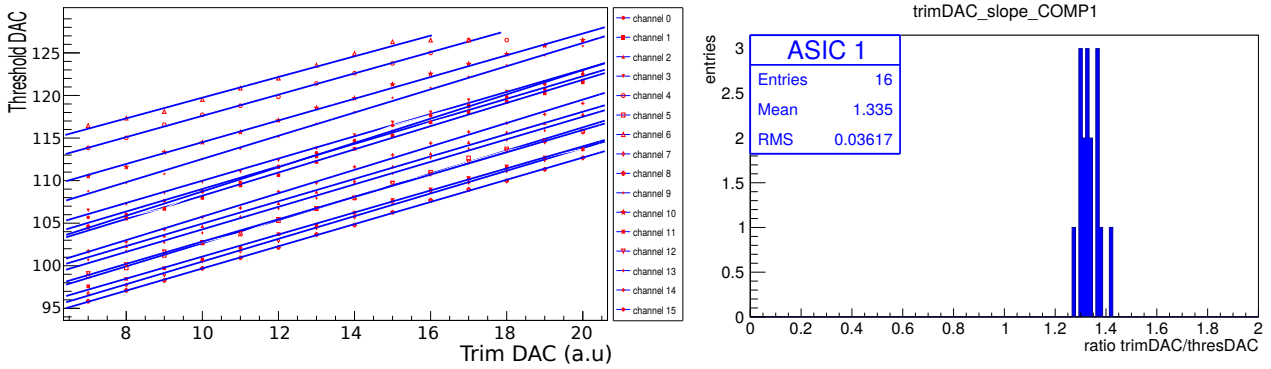


Figure 5.6: A linear fit of threshold DAC versus trim DAC for 16 channels of comparator 1 (left) is applied. A histogram with the slopes of the linear fit for 16 channels (right) is shown

### 5.2.2 DC baseline difference between two integrators within the same channel

The integration of the signal charge is implemented with two interleaved integrators within the same channel. As it has already been mentioned, these two integrators may be slightly different exhibiting a fabrication mismatch. This is manifested by a difference of DC baseline position between two integrators within the same channel. Subsequently, this DC baseline difference can induce a different digitization output for different integrators. Applying the same thresholds within the same channel, the same signal amplitude after integration can exceed the threshold for one integrator and not for the other due to the difference of DC baseline. For the sake of simplicity and limited time, this study continued investigating only one ASIC. The

DC baseline difference between two integrators of each channel is determined under two different conditions, namely before and after applying alignment of DC baseline across the channels by means of trimming as described above.

A histogram is filled with the DC baseline difference between two integrators for each channel for three comparators before applying trimming as shown in Fig 5.7. A DC baseline difference is observed between two integrators to be less than  $\pm 1$  DAC.

On the other hand, it is important to investigate whether there is a difference of DC baseline between the integrators after applying trimming in order to align the DC baseline across the channels. As long as, there is no difference between integrators before trimming and the trimming mechanism of each integrator is shifting the DC baseline at the same amount, one should expect to observe no difference after trimming as well. A histogram of the DC baseline difference between two integrators for each channel for three comparators is shown in Fig. 5.7. Once again, the DC baseline difference is observed to be less than  $\pm 1$  DACs apart from three entries, however, they are still smaller than  $\pm 2$  DACs which is considered acceptable due to the limited precision of determining the DC baseline position and binning of the histogram.

In conclusion, it is observed that there is no DC baseline difference between integrators before and after trimming. This also means that the trim mechanism shifts the DC baseline at the same amount for both integrators.

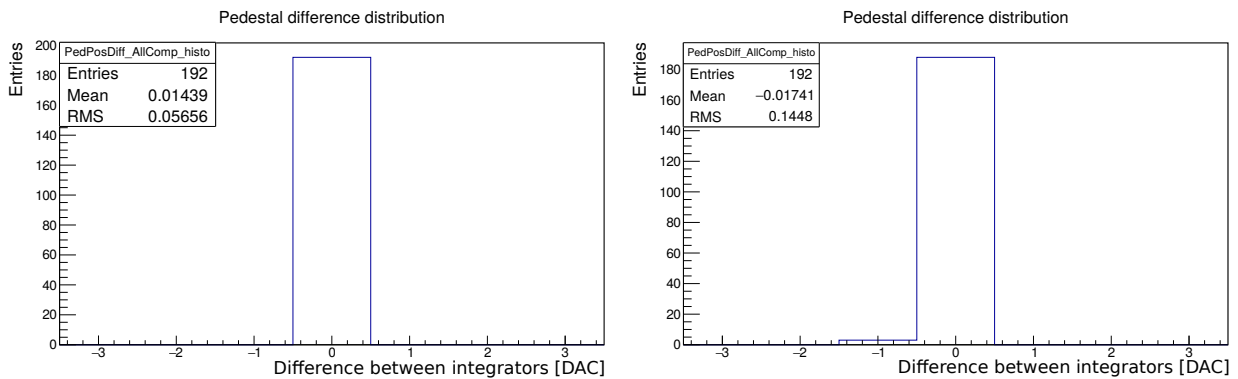


Figure 5.7: The DC baseline difference between two integrators of 64 channels for all three comparators before (left) and after trimming (right).

### 5.2.3 DC baseline difference between different states of PACIFIC

A test is performed in order to investigate whether the DC baseline of each channel for the same integrator is shifting for different operating conditions of PACIFIC. The different operating conditions are the followings:

- PACIFIC without any connection

- PACIFIC connected to biased SiPMs
- PACIFIC connected to biased SiPMs and light injection

A plot of the DC baseline of 64 channels for these three different PACIFIC operating conditions is shown in Fig. 5.8. No shift of DC baseline operating under different conditions is observed.

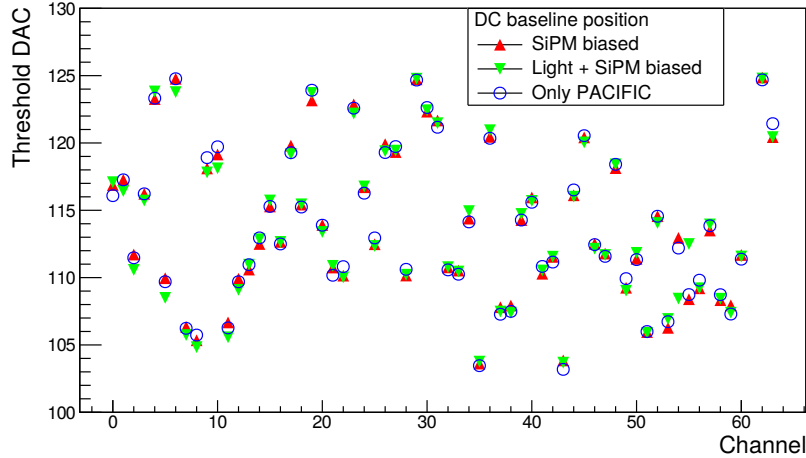


Figure 5.8: The DC baseline positions for 64 channels for different operating conditions.

## 5.3 Light injection measurements

### Synchronous system

The PACIFIC integration window is synchronized with its 40 MHz system clock, therefore it is crucial to well align the phase of the arrival of the light signal to the integration window, to ensure that the signal is fully integrated within one integration window and not split into multiple ones. Note that each integration window is 25 ns, that is one bunch crossing. Two examples are given for the sake of clarity. The first case, where the arrival of the signal from the shaper occurs between two integration windows sharing thereby the integrator output to two consecutive bunch crossings as shown in Fig. 5.9. On the next case the arrival of the signal from the shaper is fully assigned within one integration window and therefore the full charge is seen in one integration window in Fig. 5.10. The higher the integrator output amplitude is, the more thresholds are exceeded and thereby increasing the probability of being considered as a cluster candidate. Therefore, the arrival time of the signal with respect to the integration window of the PACIFIC is considered crucial, since it is going to have a strong impact on the hit efficiency.

A logic sequence should be followed before starting the calibration of SiPMs allowing us to achieve the best possible integration of the signal. An internal trigger of 625 kHz synchronous with 40 MHz system clock of the PACIFIC is generated by the FPGA. The synchronization is performed using the delay unit between the light injection system and FPGA. The arrival time of the signal is adjusted in order to achieve the maximum possible integration. A series of measurements are conducted by changing the delay time in order to find the optimum point of integration. The criterion used in order to identify whether the integration is the maximum is the "calculated observed gain". Using the so-called "S-curve", one can define this calculated observed gain of the SiPMs calculating the distance between two transitions in terms of DACs. The distance between two consecutive transitions is counted as the gain for a single photon-electron (p.e) as shown in Fig. 5.11. The counting of photon-electrons starts from high threshold value going to lower threshold values for bigger number of photon-electrons.

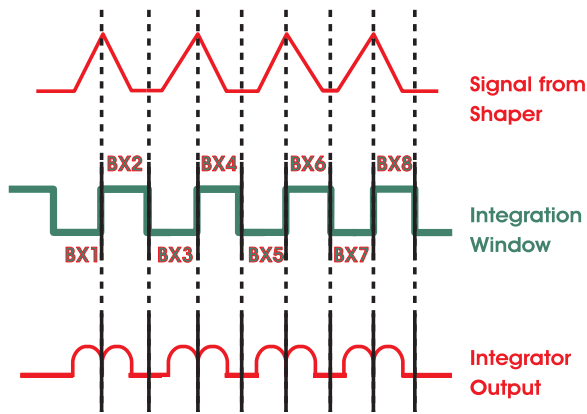


Figure 5.9: The arrival time of signal exact between two integration windows, sharing the integration of signal.

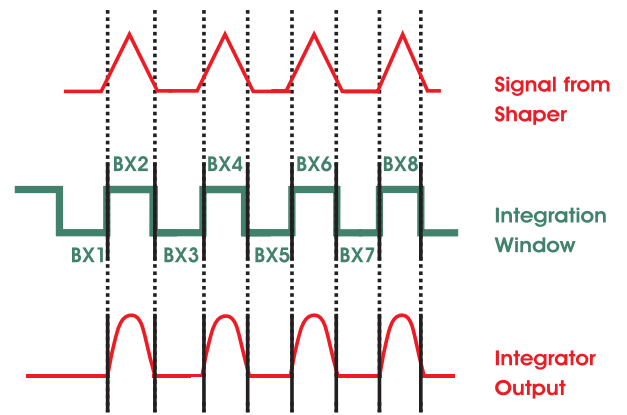


Figure 5.10: The arrival time of signal within the integration window, allowing full integration within one bunch crossing.

### 5.3.1 Delay Scan

In order to determine the best delay time for which the signal is the most integrated, the transitions of the S-curves have to be determined in terms of DACs. Once, one can observe a S-curve with visible transitions, their projections on the y-axis are extracted. That is their overThresholdRatio values as shown in Fig 5.11, which is related to the light intensity that the SiPMs are detecting. During a measurement,

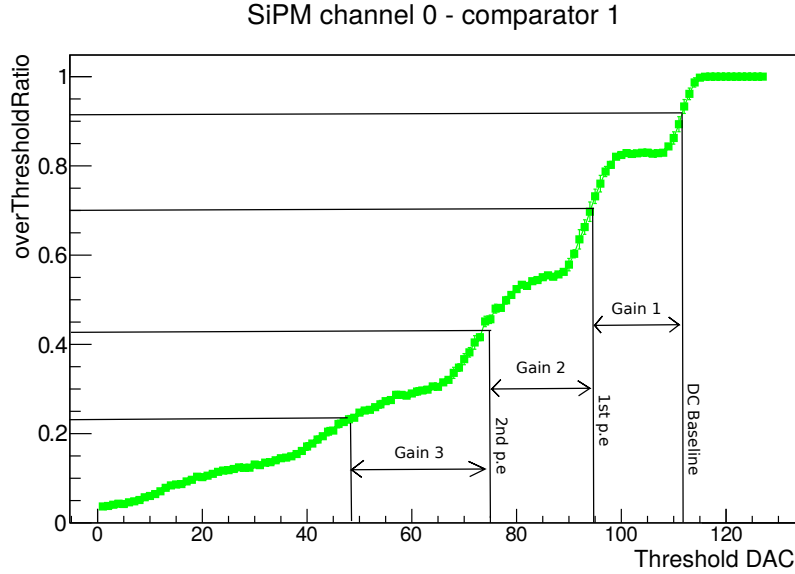


Figure 5.11: The calculated observed gain is defined as the distance between the transitions in terms of threshold DACs.

the light intensity should remain constant. Thus, the overThresholdRatio values can be used for determining the transition positions even though a S-curve is smeared due to the improper delay time as shown in 5.12.

Taking into account the overThresholdRatio values, one can determine and plot the found threshold DACs of the transitions for different delay times. The best delay time is when the distance between the transitions (gain) is the maximum. This is an indication of the best integration. This process is called "delay scan" and is shown in Fig. 5.13.

Nevertheless, for the case of PACIFICr3, this can be done only in groups of 16 channels, since it is observed that the PACIFICr3 exhibited a difference in the clock distribution of around 3ns among groups of 16 channels. Therefore, the optimum delay time would be valid only for groups of 16 channels of the chip. The first group of 16 channels was selected in order to perform the delay scan and in turn to be used for the calibration.

### 5.3.2 Tuning $V_{offset}$

In order to ensure the uniform response of the channels, the trimming has been applied such that the DC baselines are all aligned. However, using the light injection system shining 16 channels and performing a threshold scan, it is observed that the gain among the SiPMs channels is not the same even though the SiPMs are operating at the same operating voltage as shown in Fig. 5.14. The operating voltage is defined by the formula (5.1). The fact that the SiPM channels have slightly different breakdown voltages  $V_{br}$  the same  $V_{op}$  and  $V_{offset}$  result in a difference in the

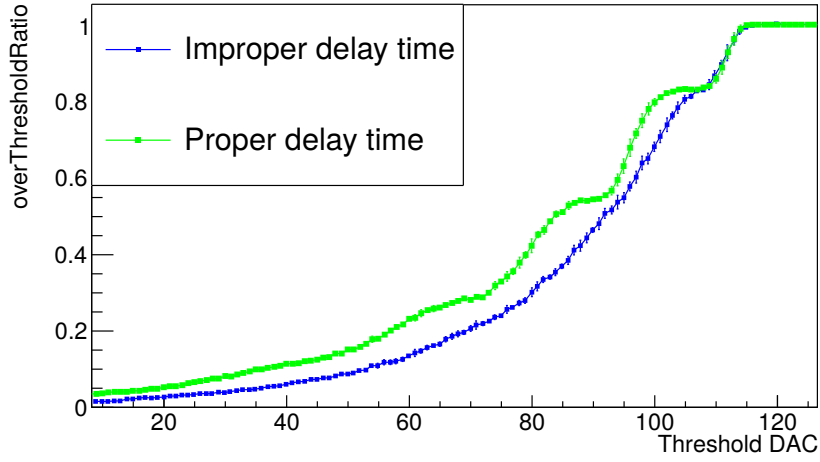


Figure 5.12: The S-curve for proper delay time and improper delay time.

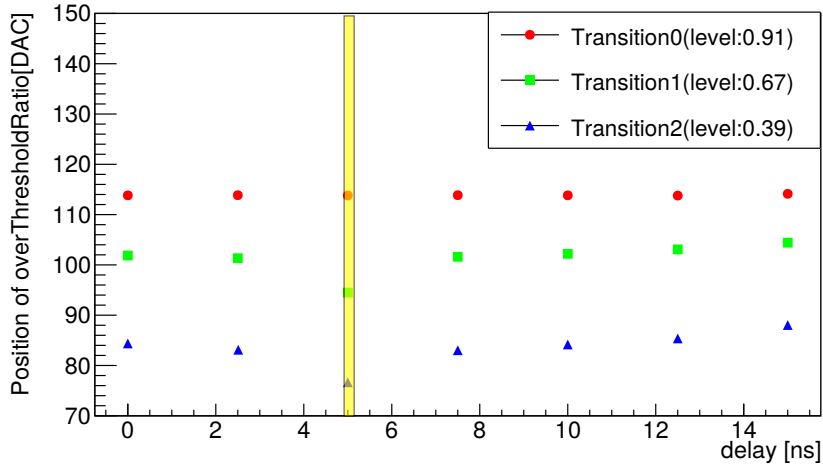


Figure 5.13: The delay of 5 ns is selected since exhibits the biggest gain. The level values correspond to the overThreshold values. Note that the counting of photon-electrons starts from high threshold DAC value going to lower threshold DAC values for bigger number of photon-electrons. Thus, the transition 0 is the DC baseline, the transition 1 is the first p.e, etc. The lower the threshold DAC the transition has, the higher the gain is.

overvoltage  $V_{ov}$  seen from each channel and in turn influences the observed SiPM gain. In order to correct the SiPM gain difference between the channels, the input voltage control  $V_{offset}$  is used.

$$V_{ov} = V_{op} - V_{br} + V_{offset} \quad (5.1)$$

Channels exhibiting smaller gain with respect to the average gain of 16 channels are tuned by increasing the  $V_{offset}$  voltage, while channels showing bigger gain are

tuned by decreasing the  $V_{offset}$  voltage, respectively. Eventually all SiPM channels have the same gain as shown in Fig. 5.15.

Now, a criterion can be established for defining an acceptable DC baseline variation among the channels relating it to the SiPM signal:

$$DC \text{ baseline variation} < \frac{1}{4} p.e$$

This requirement can be met more easily for high gain, considering the same DC baseline variation.

An inspection of the uniformity among 16 channels for all the transitions of S-curve can be made using the following Fig. 5.16. The black line indicates the DC baseline positions while the next lines the positions of p.e transitions.

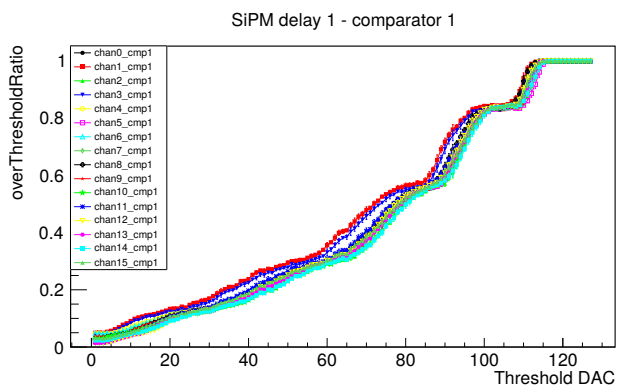


Figure 5.14: Before  $V_{offset}$  tuning.

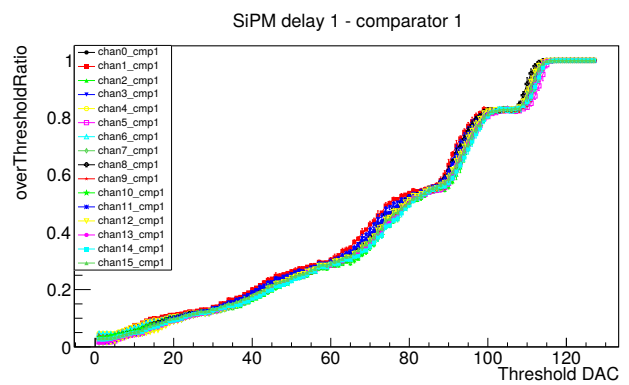


Figure 5.15: After  $V_{offset}$  tuning.

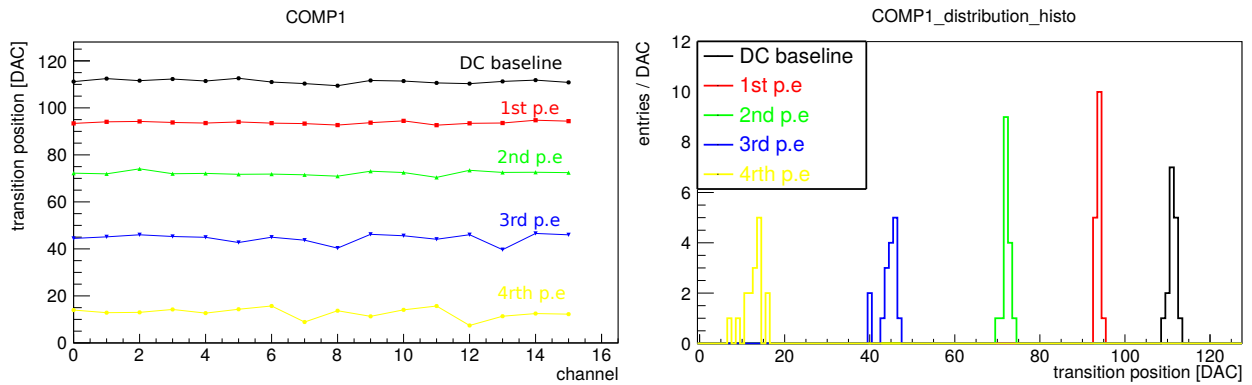


Figure 5.16: The transition positions of DC baseline(black), 1<sup>st</sup>(red), 2<sup>nd</sup>(green), 3<sup>rd</sup> (blue) and 4<sup>th</sup>(yellow) p.e for 16 channels (left). The position distributions of each transition for 16 channels (right).

### 5.3.3 Calibration of the threshold DACs

Once, the alignment of both DC baseline and p.e positions between 16 channels has been accomplished. The calibration can be done allowing to extract the relation between threshold DACs and photo-electrons. The mean threshold DAC value of each transition position distribution of 16 channels for the first comparator as shown on the right side of Fig. 5.16 is used for plotting Fig. 5.17. Since the PACIFICr3 is not linear, a second order polynomial is used for fitting the threshold DACs as a function of photo-electron transitions. This information can be used in order to set the thresholds of the cluster algorithm expressed in photo-electrons, low threshold = 1.5 p.e, middle threshold = 2.5 p.e and high threshold = 3.5 p.e.

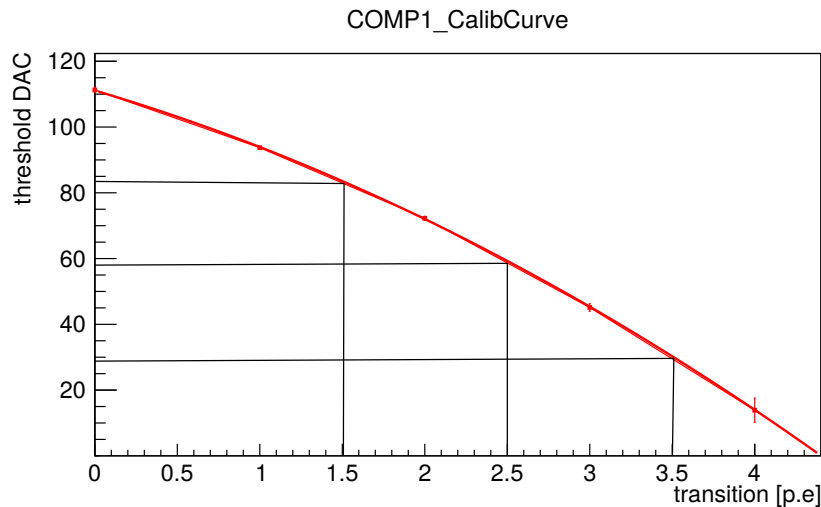


Figure 5.17: The calibration of threshold DACs as a function of p.e of 16 channels for the first comparator allows to determine the thresholds as follows: 1.5 p.e = 83 DAC, 2.5 p.e = 58 DAC and 3.5 p.e = 28 DAC. Thus, for setting the low threshold common for 16 channels, the 83 threshold DAC value is used.

## 5.4 Beta source measurements

### Semi-Synchronous system

After the calibration has been completed and the global thresholds for 16 channels have been properly set, measurements with the asynchronous beta source can be conducted. There is a crucial difference between the light injection system and beta source measurements. Signal from the radioactive source are randomly distributed following a poisson distribution. Thereby, the arrival time of the signal in PACIFIC induced by a beta source particle is random and therefore not synchronous with the 40 MHz integration clock. Thus, a tool has to be developed allowing to select the events within the integration window.

Once a particle passes through the fibre mat, the trigger is also fired sending a "trigger signal" to the FPGA. In parallel, the particle generates scintillation light in the fibre mat which is detected by SiPM, read out and digitized by the PACIFIC and ,in turn, the data are transferred to a FPGA called as "particle signal". The trigger signal comes always later with respect to the particle signal to the FPGA. Since, the trigger signal experiences a delay because of the trigger response, cable length and all the NIM logic devices. While, the particle signal experiences a delay due to the light propagation in the fibre mat, the SiPM response and the PACIFIC response. A delay unit is inserted between the trigger and the FPGA in order to adjust properly the arrival time of trigger signal to the FPGA as shown in Fig. 5.18.

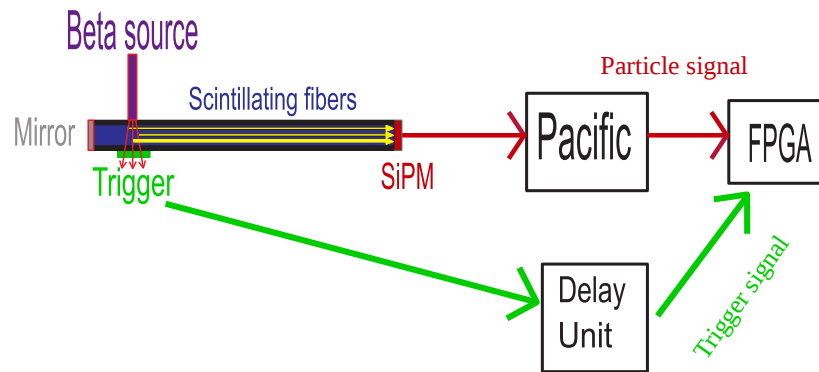


Figure 5.18: Once a particle passes through the fibre mat and trigger, two signals are made. The trigger (green) and particle (red) signals arrive at the FPGA with constant time difference.

#### 5.4.1 Selection of events: Finetiming

The trigger and particle signals arrive at the FPGA with a constant time difference independently of the integration window of PACIFIC. The PACIFIC is integrating the input signal from the SiPMs every 25ns. While the FPGA is saving the PACIFIC output in its memory. As soon as the particle signal arrives in the FPGA, after a certain time the trigger signal is expected to arrive as well. The delay  $t_{delay}$  between those two signals is constant and it can be determined using an oscilloscope. As long as the  $t_{delay}$  is known, for every trigger signal arriving at the FPGA, one has to look back in time by ( $< t_{delay}$ ) in memory and fetch eight consecutive bunch crossings of the PACIFIC output where the particle signal is expected to be. Then,

these eight bunch crossings are moved to a FIFO (First In First Out) allowing the correct timing sequence of the triggers detected and in turn write them to a file. A wide window of 8 bunch crossings is considered intentionally ensuring that within them, the particle signal is going to be distributed and allowing to study the spill over effect.

The arrival of the trigger signal can be measured within the FPGA using an internal TDC (Time to Digital Converter) counter. It is always counting from 0 to 32 with a step of 780 ps. Therefore, a full circle of this counter (25ns) is fully covering the integration circle of the PACIFIC. Each step of 780 ps is defined as "finetiming". Each trigger signal is recorded having its own finetiming stamp. Thereby, one can sort out all the triggers which exhibit the best integration making use the finetiming stamp. An example is provided in Fig 5.19 in order to explain the logic behind the finetiming.

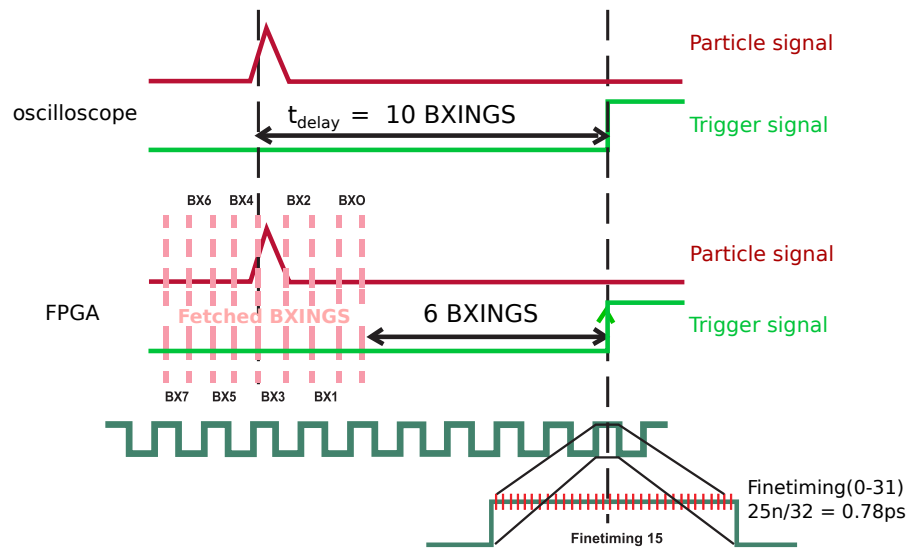


Figure 5.19: Driving both trigger (green) and particle (red) signals in oscilloscope. The  $t_{delay}$  is determined to 10 bunch crossing (250 ns). Then, one should look in the memory of FPGA back in time by 6 BXINGS and fetch 8 bunch crossings (pink). The particle signal is going to be distributed in the third bunch crossing of these 8 fetched bunch crossings. The trigger arrival in FPGA is stamped with the TDC counter so-called finetiming (Finetiming 15).

## 5.4.2 Delay Scan

Checking the number of events over thresholds in a series of 8 fetched bunch crossings, one can observe that the signal is mainly distributed into three of them. By

changing  $t_{delay}$  one can select in which of the bunch crossings the signal is distributed. In order to maximise the integrated signal, the signal should fall into a single bunch crossing. This is achieved by performing a delay scan. Therefore the number of events over thresholds in three consecutive bunch crossings is summed up. For each of these bunch crossings the fraction of the sum is calculated. This fraction should be as high as possible in one bunch crossing while being as low as possible in the other two. To do so, the "best channel" which exhibits the best integration, that is passing the thresholds at most has to be selected as well. Positioning the beta source on the fibre mat as shown in the Fig. 5.20, one should record a source profile. Thus, at the center of the source, it is expected the most generated light and in turn the corresponding PACIFIC channel ("best channel") detects this light obtaining the most analogue signal. The fractions of the three bunch crossings are plotted together in order to find the best  $t_{delay}$ . In practice the delay in the delay unit, which is one the adjustable components of  $t_{delay}$ , is varied. The result of such a delay scan is shown in Fig. 5.21.

A finetiming histogram is filled using all the triggers of all bunch crossings and all channels as shown in Fig. 5.23. This reveals that there is something influencing the read-out. The reason of this is the firmware structure. The FPGA TDC counter has a limited resolution of 1 ns. Despite this limitation, a trick in the logic is used to reduce the resolution down to 780 ps, however, this induces a repetitive pattern. This pattern is not due to different bin sizes but it is the result of the software. Repeating this procedure for the best channel and the best bunch crossing, one obtains a distribution shown in Fig. 5.22. The repetitive pattern is still visible below the signal distribution. In order to cancel out this repetitive pattern in the finetiming histograms, the number of events considering all three thresholds passed for each finetiming of Fig. 5.22 are divided by the number of triggers of Fig 5.23. The corrected finetiming plot is shown in Fig. 5.24 without being affected from the bias effect of firmware structure. This shows a probability distribution of the arrival of the particle signal with respect to the integration clock of PACIFIC for the given trigger finetimings. In this finetiming plot, a plateau of 8 ns is seen considering 15% variations on the y axis.

## Clusterization studies

For performing clusterization, one selects a window of 4 finetimings which corresponds to the maximum of the distribution shown in Fig. 5.24. In this area the number of events over thresholds per trigger is the highest and therefore the signal is integrated at most.

### 5.4.3 Threshold bit pattern

In order to test whether the thresholds have been set correctly for applying the clusterization, a bit pattern of 001, 011 and 111 should be expected from the measurement. The pattern 001 corresponds to the low threshold ( $TH_{low}$ ), 011 to the

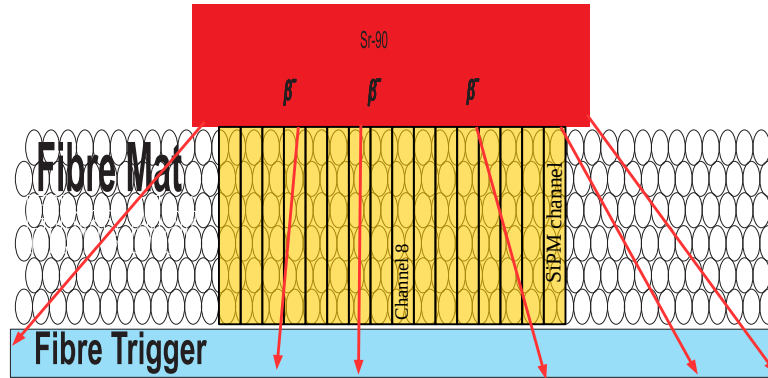


Figure 5.20: The position of beta source on the fibre mat without collimator. The channel 8 is considered as the "best channel".

middle threshold ( $TH_{middle}$ ) and 111 corresponds to the high threshold ( $TH_{high}$ ). Any different bit pattern than the previous ones indicates an error of de-serialization at the data acquisition system. All bit patterns are shown in Fig. 5.25 for before and after selecting the best four finetimings. It is necessary to normalize the counts per bit pattern for each group of finetimings. This allows to determine the percentage of each bit pattern for the aforementioned cases of finetimings as shown in the following Table.

finetimings	$TH_{low}$ [%]	$TH_{middle}$ [%]	$TH_{high}$ [%]	SUM [%]
32	42.3	23.8	33.9	100
4	19.2	17.8	63.0	100

It turns out that this selection of four finetimings excludes a significant fraction of events which pass only the low and middle thresholds. As a result, most events (63%) pass the high threshold, which is a manifestation of integration efficiency of this finetiming area.

#### 5.4.4 Cluster distribution/size

The cluster distribution and the cluster size distribution for the case where the beta source is positioned exactly on the fibre mat after pre-selection of the best four finetimings are shown in Fig 5.26 and 5.27, respectively. Apart from this position, the beta source is also positioned in a collimator of 6 mm diameter, 2 cm and 20cm above the fibre mat as shown in the Fig. 5.29, in order to investigate the impact of the given geometry on the clusterization algorithm. As soon as the beta source is positioned in the collimator, the observed source profile becomes flat compared with

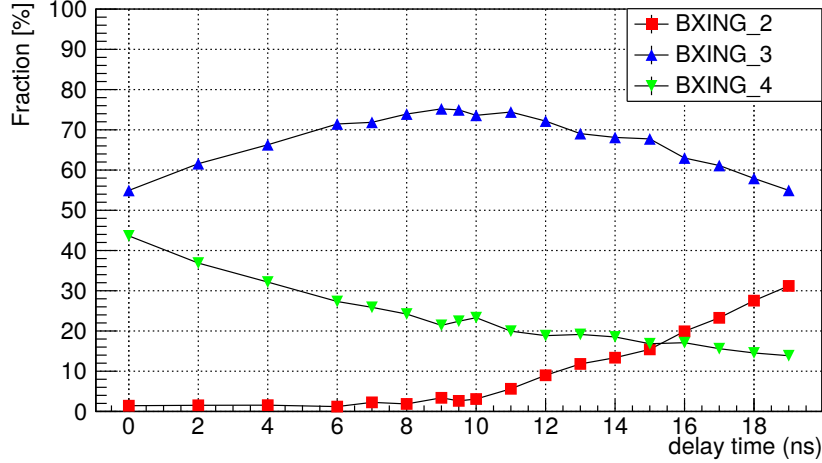


Figure 5.21: The delay time of 9 ns of delay unit is selected since exhibits the most integration within bunch crossing 3. An integration plateau above 70% for 7 ns with a maximum value of 75.21 % are observed.

the source profile without a collimator since only the center part of source profile is allowed to hit the fibre mat as shown in Fig. 5.28.

Measurements with different size of data were taken in order to investigate the cluster size distribution. Huge cluster size up to 15 channels have been observed. The cluster size distribution is normalized to one for the cases where the beta source is in a collimator 2 and 20cm above the fibre mat are presented in the Fig. 5.30. For the given geometry one can calculate the maximum incident angle of incoming particles. For the case, where the beta source positioned 2 and 20 cm above the fibre mat, the maximum incident angle of particle track is almost perpendicular to the fibre mat. Therefore, ideally it is expected that the tracks are hitting few adjacent fibres and therefore inducing small cluster size of 1-2 channels. However, considering effects such as cross talk in the fibre mat and SiPMs and the not perfect geometrical alignment of fibre to the SiPMs channels. One should expect a maximum cluster size of 4-6 channels.

One of the reasons of obtaining such big clusters is the generation of energetic electrons so-called  $\delta$  electrons hitting multiple neighbour scintillating fibres.

On the other hand, the cosmic rays could be considered as candidates for explaining such huge cluster sizes. Since they follow a  $\cos^2 \theta$  distribution [56] there is possibility for them to hit the fibre mat under large angles.

Measurements are performed at different positions of the beta source.

- Directly on the fibre mat without collimator (0 cm)
- 2 cm above the fibre mat with collimator (2 cm)
- 20 cm above the fibre mat with collimator (20 cm)

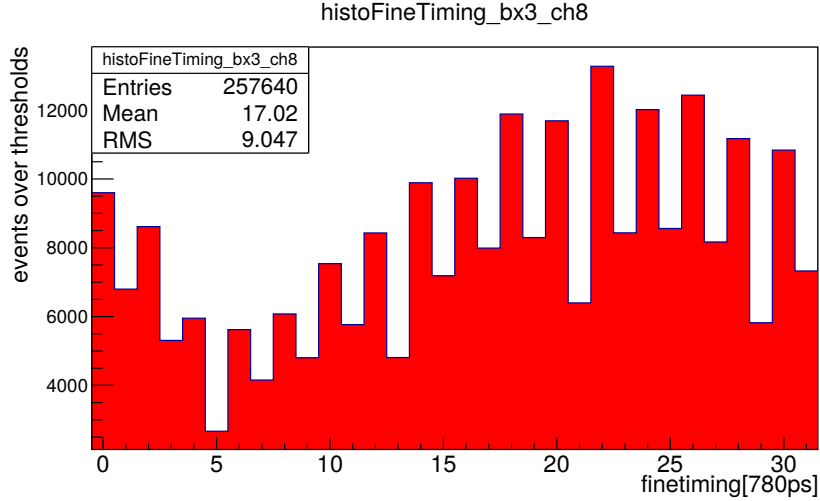


Figure 5.22: The finetiming distribution for the best bunch crossing 3 and best channel 8.

Their percentages of each cluster size is shown in table 5.2.

Cluster size	0cm[%]	2cm[%]-collimator	20cm[%]-collimator
1	8.1	11.0	5.6
2	38.9	38.9	34.7
3	31.9	32.6	38.5
4	13.8	12.6	15.8
5	4.7	3.2	3.9
6 >	2.6	1.7	1.5

Table 5.2: The cluster size percentage for each different position of beta source

No big differences are observed between the cases of 0 cm and 2 cm in the collimator. However, a difference on the most probable value between the cases of 2 cm and 20 cm is observed. Since, the most probable value of cluster sizes is 2 and 3 channels marked with red color in table 5.2 for beta source position on 2 and 20 cm above the fibre mat, respectively. This could be an indication of energy loss of electron travelling different distances through the air. Therefore, the less energy the electrons have the more energy they deposit and subsequently producing more light which can activate neighbour fibres. Moreover, the longer the distance is the more multiple scattering the particle experiences.

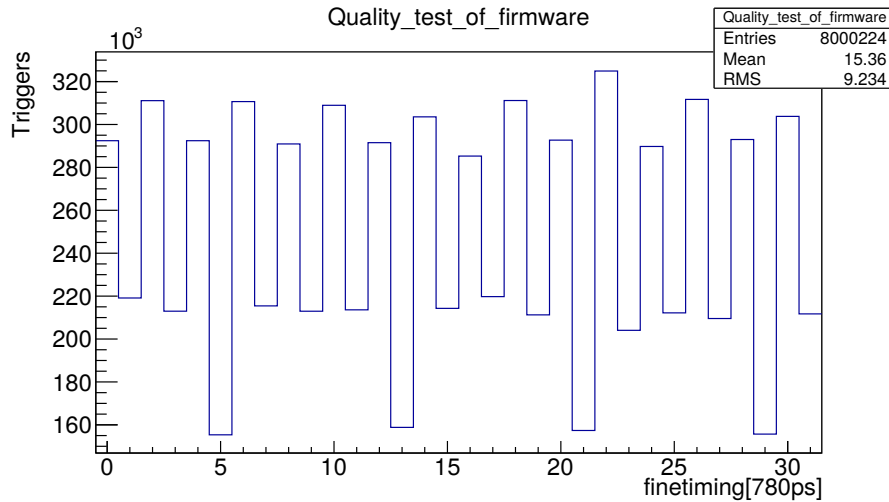


Figure 5.23: The finetiming histogram including all triggers gives an inspection of the quality of firmware.

### 5.4.5 Threshold scan with a beta source

Using the beta source, one can perform a threshold scan to obtain S-curve plots. This S-curve allows a comparison between the beta source and the light injection measurements and provides a verification of the exhibited gain. In contrast to the threshold scan presented before, not all channels, but only those that form a cluster center are compared to the low threshold. It turns out that due to the high light intensity in the cluster centers, the threshold is always exceeded. This leads to flat S-curve without visible transitions making it impossible to determine the gain. This problem is solved by comparing the neighbouring channels to the threshold instead of the cluster center channels. These measurements are performed using the first, second and third neighbour channels, as can be seen in Fig. 5.31. Transitions become visible when using the second and third neighbour. The rate of events over threshold decreases because those channels detect less light and are less likely to pass the low threshold. The transitions still occur at the same threshold DAC values, as expected.

In order to compare the S-curves of beta source and light injection, the average S-curve of all 16 channels of light injection has to be calculated. Since, for the beta source case, a threshold scan is applied looking for cluster centres distributed over all 16 channels. For comparison reasons, the overlay of two S-curves, coming from the beta source using the 2nd neighbour channels and the light injection system, are shown in Fig. 5.32. One can notice that the transitions occur at the same threshold DAC values (same gain) as expected since both measurements were conducted using the same voltage settings. However, a shift is observed between these two S-curves on the y-axis, this is due to the different light intensity detected by SiPMs.

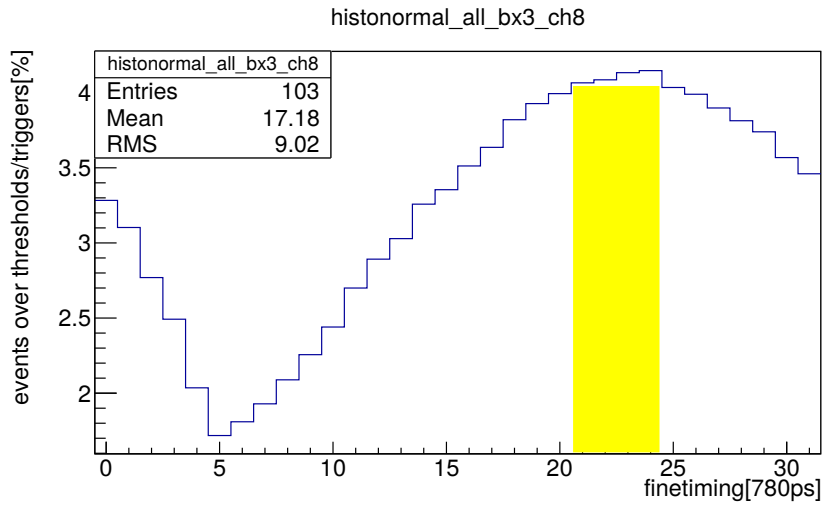


Figure 5.24: The unbiased finetiming histogram for the best bunch crossing 3 and best channel 8, the yellow area marks the selected finetimings for further processing.

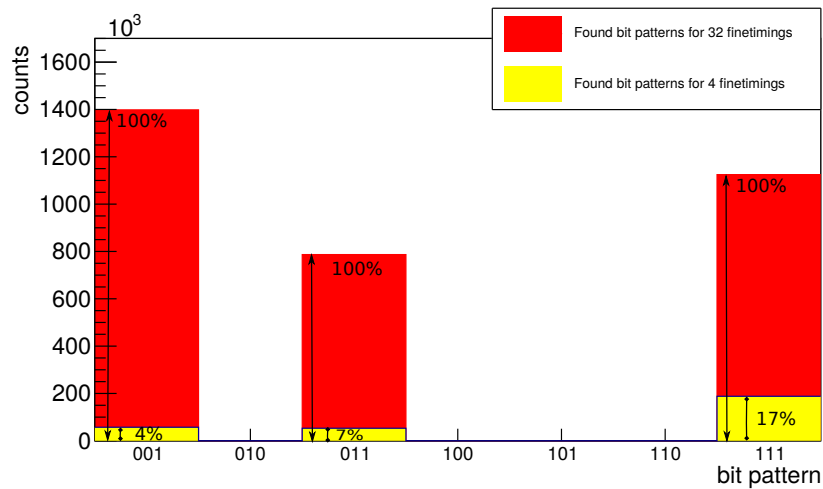


Figure 5.25: The bit patterns of measurement before (red) and after (yellow) the selection of the best 4 finetimings (marked with yellow in Fig .5.24) resulting a decrease of 96 %, 93 % and 83 % for low, middle and high thresholds, respectively. However, the bit pattern of high threshold is relatively larger than the other bit patterns after the selection of four finetimings.

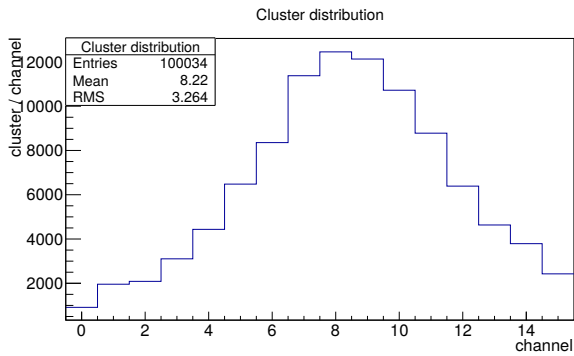


Figure 5.26: The location from  $\beta$ -tracks after applying pre-selection of the best four finetimings of most threshold passed.

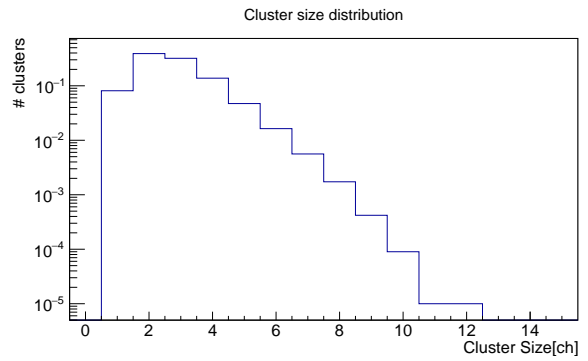


Figure 5.27: The cluster size distribution after applying pre-selection of the best four finetimings of most threshold passed.

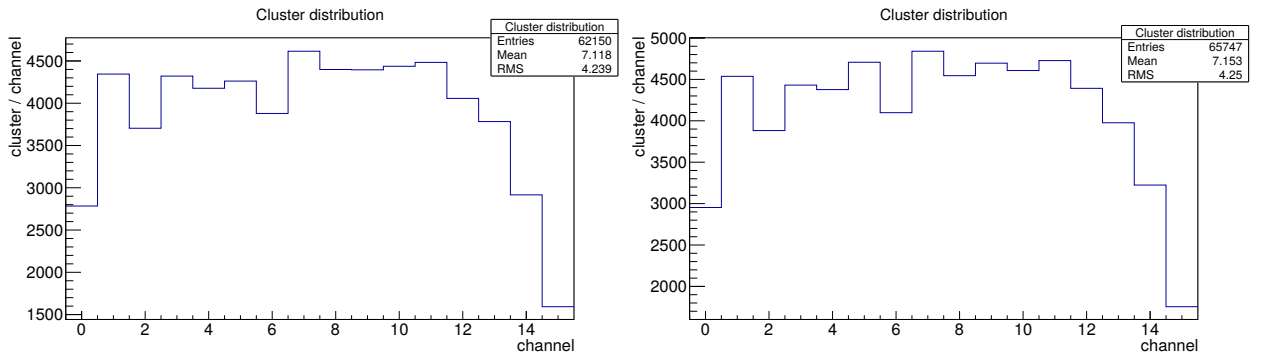


Figure 5.28: The cluster distribution for the case where the position of beta source is in the collimator 2(left) and 20 (right) cm above the fibre mat results a flat source profile.

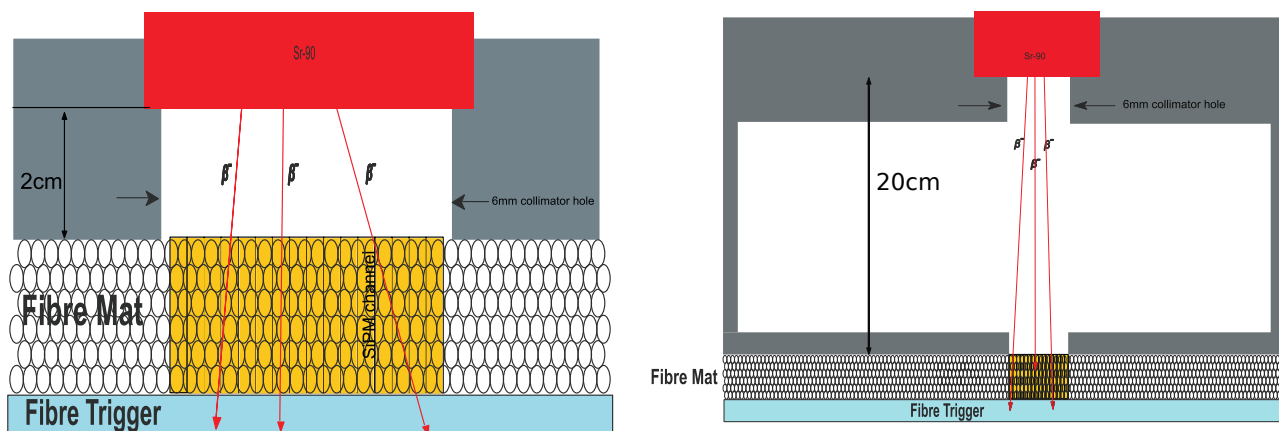


Figure 5.29: The beta source position in the collimator 2cm(left) and 20cm(right) above fibre mat.

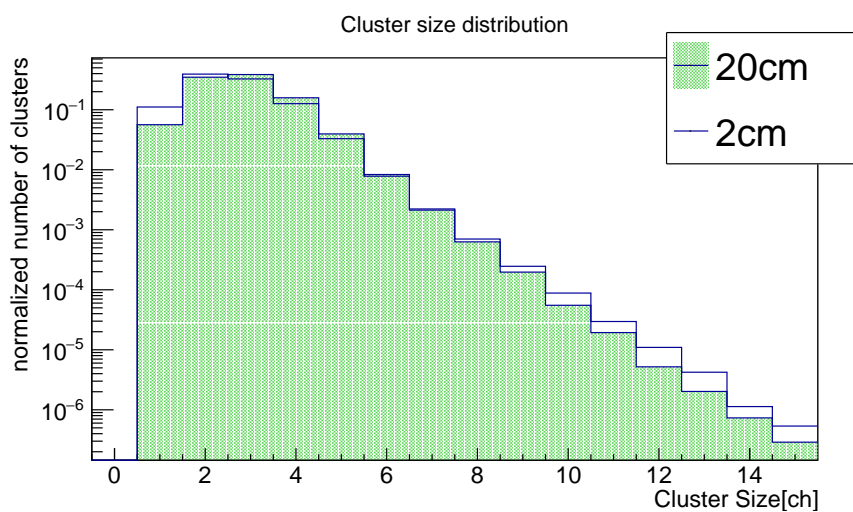


Figure 5.30: The cluster size distributions for large data sets for the cases of positioning the beta source 2cm and 20 cm above fibre mat.

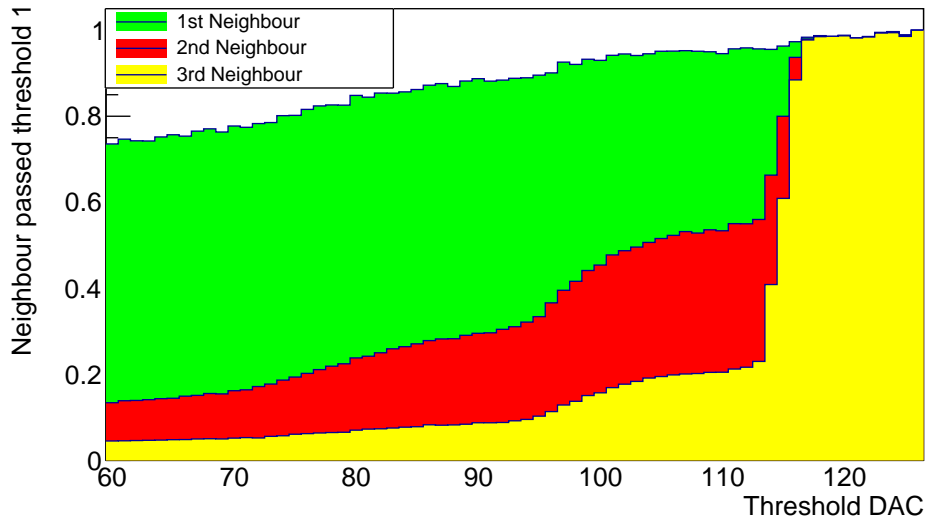


Figure 5.31: Three different cases of different neighbours are shown resulting three different S-curves. The photon transitions are clearly shown for the case of 2nd neighbour.

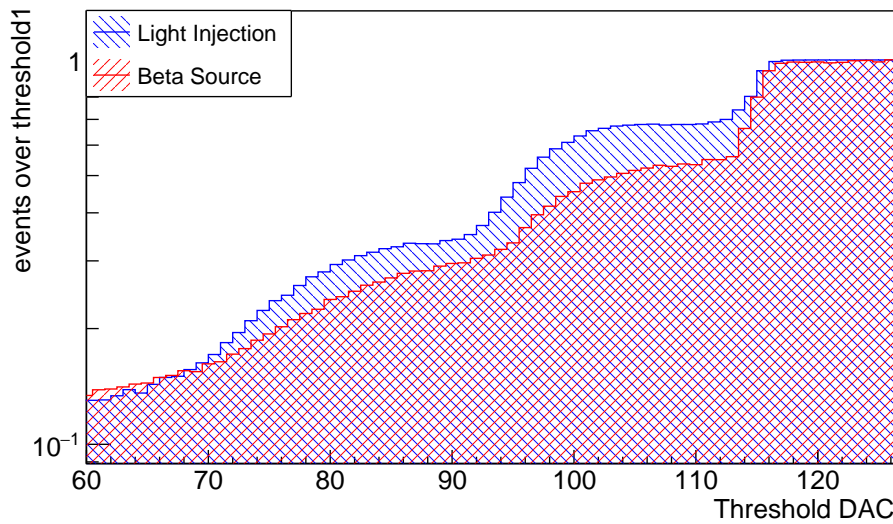


Figure 5.32: The two S-curves for beta source and light injection system shows that the transitions occur at the same threshold DAC.

## 6 PACIFICr4 characterization studies

The PACIFICr4 is the latest available version of PACIFIC ASIC that can be studied. The experimental setups used for this study were the same as for PACIFICr3 as described in section 5.1.

Before starting this chapter, it is necessary to summarize the new features of PACIFICr4 with respect to PACIFICr3:

- A higher granularity of 8 bits threshold DAC for all comparators.
- The CMC (common mode control) was removed. Thus, trimming was the only available mechanism to compensate potential variations.
- Local thresholds available for each channel.
- A uniform clock distribution across 64 channels.
- A wider integration window

The first characterization results show a problem of the comparator range and trimming circuit.

### Comparator range

The bias N-MOS transistor of the comparator circuitry implemented using Cadence<sup>1</sup> as shown in Fig. 6.1 experiences a saturation for high DAC values. This means that by increasing the voltage  $V_{ds}$  (drain-to-source voltage) as shown in Fig. 4.1, the current remains steady and therefore the MOSFET operates as a current source. This means by increasing the  $V_{ds}$  no more voltage drop over the N-MOS is provided, limiting thereby the range of threshold DACs to a value of 150, which corresponds to voltage of around 300 mV as shown .1 in the appendix. To solve this, the N-MOS bias transistor will be replaced by a P-MOS input version (reverse logic) in the PACIFICr5 allowing to reach the maximum threshold DAC value of 255 (0 V).

### Trimming

The trimming mechanism is capable of only adding current to trim the DACs allowing only a positive shift of the DC baseline. Since it exhibits an unstable behaviour for the case of removing current from the trim DAC in order to shift the DC to the lower threshold DACs as shown in Fig. 6.2. To solve this, a filter in the end of the Miller OPAMP in the integrator was added to PACIFICr5 such that thereby reducing the bandwidth and, in turn, make it more stable.

---

<sup>1</sup>Cadence is a multinational electronic design automation (EDA) software

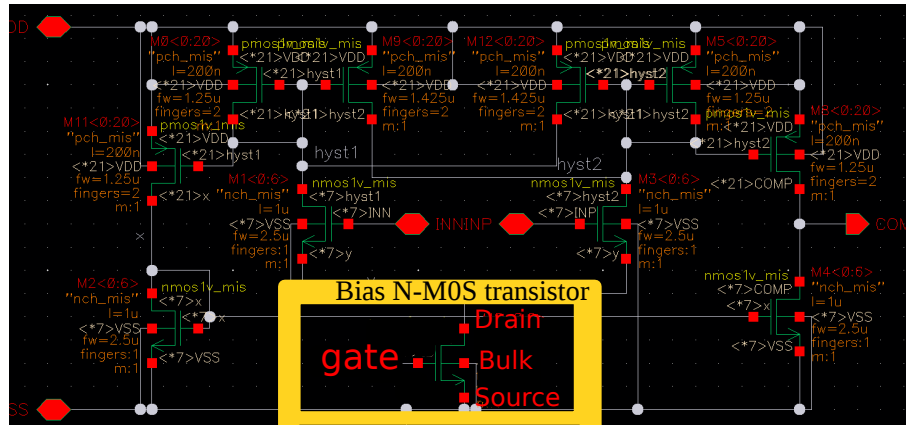


Figure 6.1: The CMOS schematic diagram of hysteresis comparators circuitry are shown left and right side of figure, while the bias N-MOS transistor is marked with yellow color [57]. The drain, source and gate terminals are marked with red color.

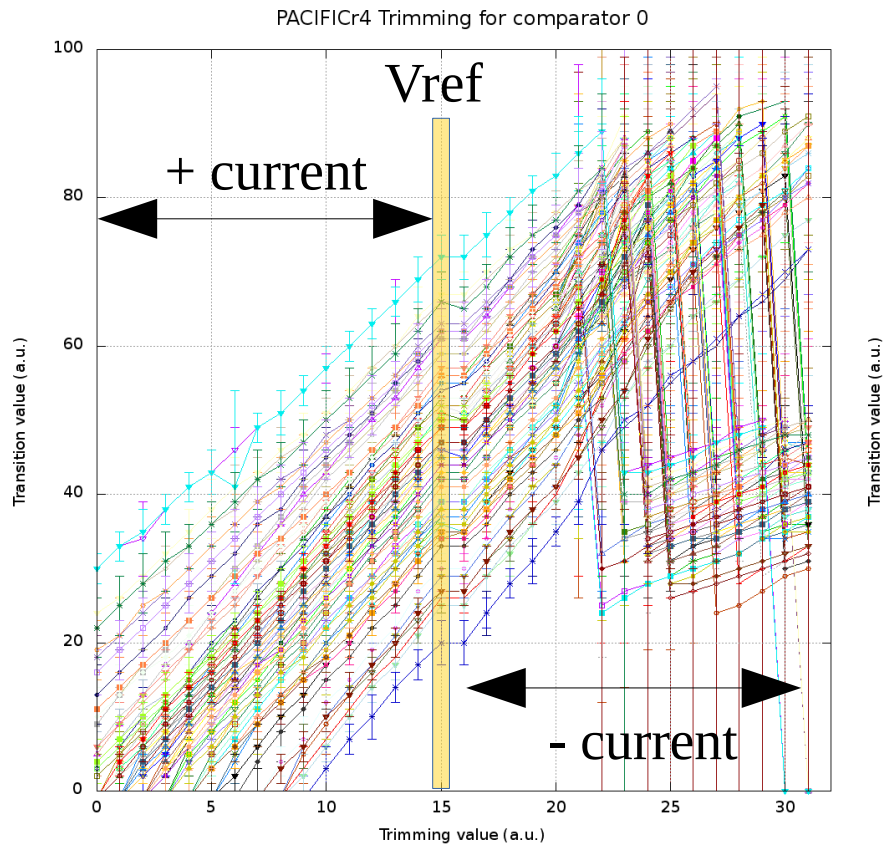


Figure 6.2: The areas where current is adding and removing from the trim DACs inducing a positive and negative shift with respect to reference voltage of each channel ( $V_{ref}$ ) [57].

## 6.1 DC baseline variation of the integrators

Once again it is necessary to test the PACIFIC uniformity. However, the only available mechanism allowing to cancel any non-uniformity response between integrators of PACIFIC is the trimming mechanism.

A problem encountered when a threshold scan is performed using a common threshold for multiple channels. In this case, large variations in the DC baseline can be observed for the three comparators of a channel. These differences decrease when the threshold scan using common thresholds is performed for a lower number of channels. Fig. 6.3 shows this effect for threshold scans using 8 and 64 channels. This problem is intrinsic to the chip and will be fixed in PACIFICr5. For PACIFICr4 a common threshold can in principle be used for 8 channels. However, the differences of the DC baseline between channels is 15-20 thresholds DACs which can not be compensated by the trimming mechanism due to the limited trim operating area as shown in Fig. 6.2. Instead local thresholds are used for each channel.

In case of the PACIFICr3, there are no significant differences in the DC baseline between the two integrators. Instead, corrections concerning the differences between the channels have to be performed. In contrast to this the local thresholds are used in PACIFICr4. The trimming mechanism has to be used in order to reduce the DC baseline difference only between integrators. Fig. 6.4 shows a histogram of the differences between the integrators for 64 channels and all three comparators after trimming. The distribution shows long tails on both sides. Mismatch of the DC baseline between the three comparators of a each integrator makes a perfect alignment impossible, leading to these outliers. Fig. 6.5 shows the mismatch between the comparators. The DC baseline difference is calculated separately for the three comparators and filled into the bin corresponding to the channel number.

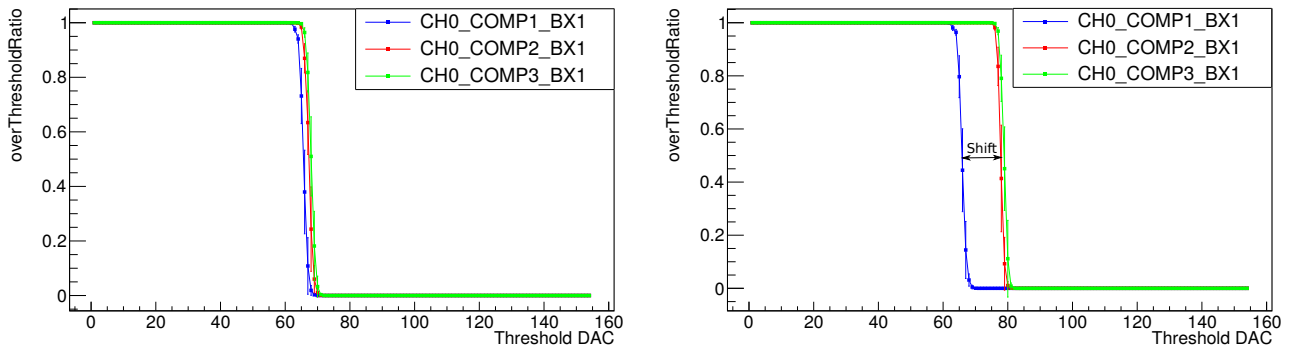


Figure 6.3: Threshold scan using common thresholds for only 8 channels(left) and 64 channels(right) shows a shift of the DC baseline of two comparators.

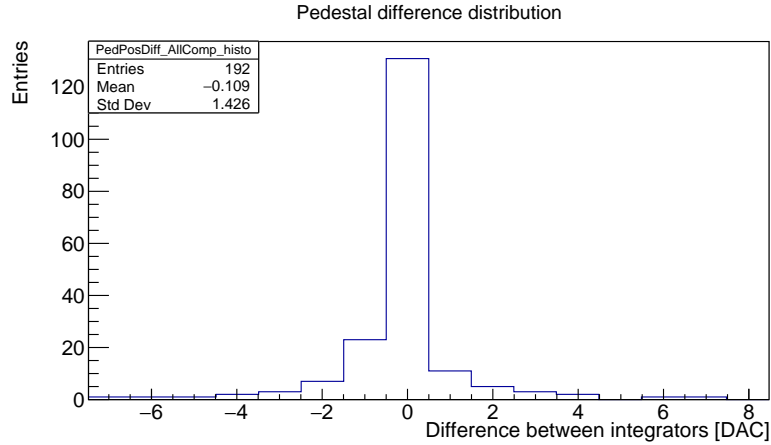


Figure 6.4: The DC baseline difference between two integrators for 64 channels  $\times$  three comparators after trimming alignment.

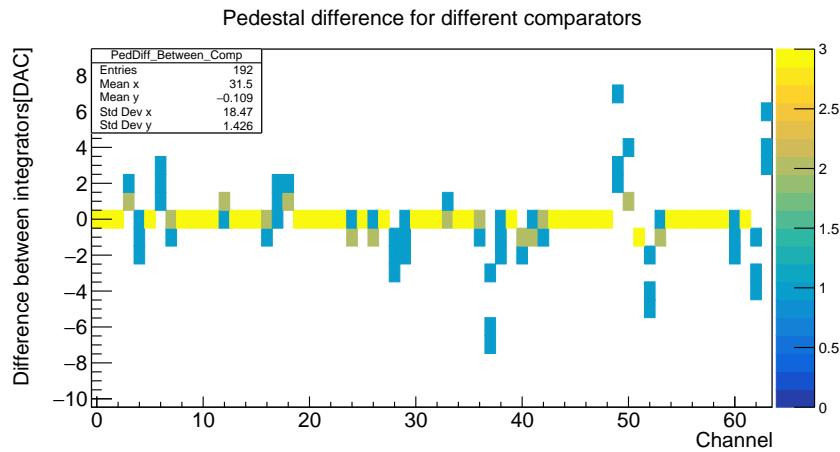


Figure 6.5: The DC baseline difference between two integrators for three comparators after trimming alignment can show the comparator mismatch.

### 6.1.1 DC baseline difference between different states of PACIFIC

The same procedure as for PACIFICr3 to investigate whether the DC baseline shifts for different operating conditions is applied also for PACIFICr4. The different operating conditions are the followings:

- PACIFIC without any connection
- PACIFIC connected to biased SiPMs
- PACIFIC connected to biased SiPMs and light injection

A plot of the DC baseline of 64 channels selected for these three different PACIFIC operating conditions is shown in Fig. 6.6. A shift is observed for channel 49, however,

this is due to the fact that the DC baseline position is out of the threshold DAC range. The algorithm finds thereby the next transition which is the 1st photon interpreting as DC baseline. Eventually, no DC baseline shift is observed.

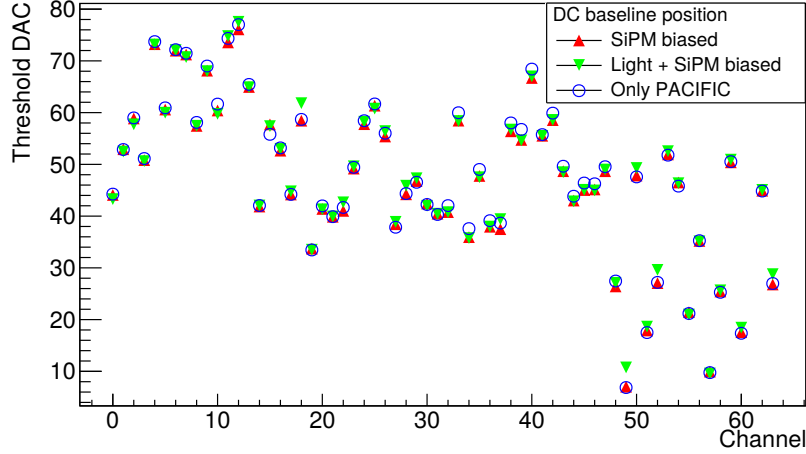


Figure 6.6: The DC baseline position for 64 channels for different states considered.

## 6.2 Light injection measurements

All measurements presented in this section are performed using a light injection system.

### 6.2.1 Delay Scan

As long as, the uniform response between two integrators within the same channel is ensured, there is no reason to use the  $V_{offset}$  in order to tune the voltage of each channel in order to align for 1 p.e transitions between channels.

The light injection system is used as explained in section 5.1.1 in order to perform a delay scan, however, we used HQR 2016 Hamatsu SiPMs instead of HQR 2015. A delay scan is employed in order to find the best delay to integrate the largest amount of signal. As it is presented for PACIFICr3, one has to determine the transitions of S-curve in terms of overThresholdratio levels. Since the overThresholdratio values can be used even though the transitions are not visible due to the not proper integration. Using these overThresholdratio values, the corresponding threshold DAC of the transitions of the S-curve can be determined for different delay times as shown in Fig. 6.7.

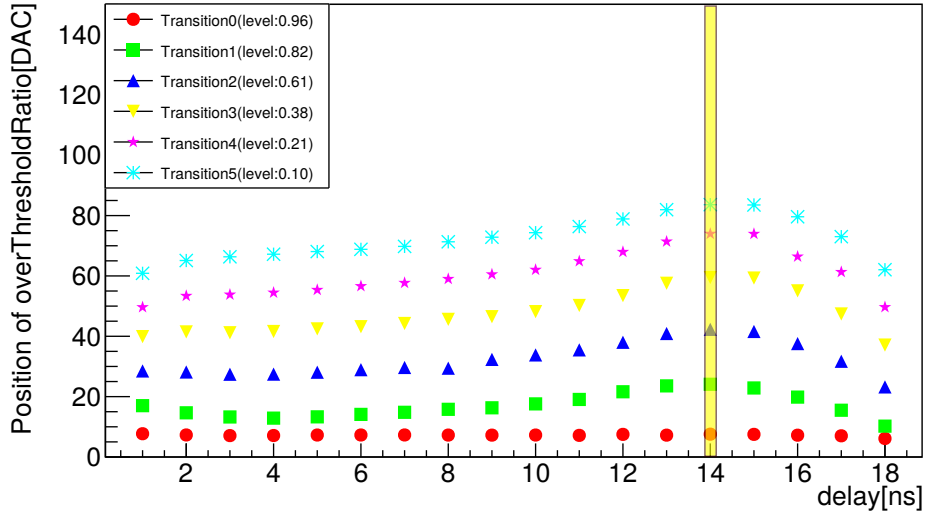


Figure 6.7: The best delay time is 14 ns exhibiting the best integration. The six transitions of a S-curve with their overThresholdRatio levels are shown. Note that the PACIFICr4 S-curve is inverted compared with PACIFICr3 S-curves, this means that the counting of photon-electrons starts from low threshold DAC value going to higher threshold DAC values for bigger number of photon-electrons. Thus, the transition 0 is the DC baseline, the transition 1 is the first p.e, etc. The higher the threshold DAC the transition has, the higher the gain is.

## 6.2.2 Breakdown voltage determination

The gain of SiPMs can be used in order to determine the breakdown voltage of each SiPM channel.

The distances between the transitions of S-curves ("calculated observed gain") have to be calculated for different operating voltages. Then, one can plot the gain as a function of operating voltage. A linear fit is performed such that the intercept of the fitting line with the x axis gives the breakdown voltage which corresponds to zero gain.

The first distance between DC baseline and 1st photon defines the 1st gain. The distance between the 1st photon and 2nd photon the 2nd gain etc. We have typically 5 transitions on the S-curves, that is 4 gain values. If the PACIFIC was linear, all these different gains should be equal.

However, this is not the case. Using the following notation to indicate the position of DC baseline position with P0, the first photon position with P1 etc. The extrapolation of breakdown voltage using all distances ("calculated observed gains") of P4-P3, P3-P2, P2-P1 and P1-P0 for the four operating voltages is shown in Fig. 6.8. Specifically, for the cases of P1-P0 and P4-P3, it can be shown that the determination of breakdown voltage fails, since a nominal breakdown voltage of 51.0V

at 25 C° is expected from characterization results conducted by EPFL<sup>2</sup> [58], where slight variations from SiPM channel to channel are expected. There are two different effects leading to wrong breakdown voltage here:

The first effect observed is the assignment of the 1st photon to the DC baseline for some channels rendering very difficult for the algorithm to distinguish those two transitions. The problem is even worse for low operating voltages where the gain is low. While, for high operating voltages, it is observed that the distance between the DC baseline and 1st photon (P1-P0) is always smaller with respect to the other transition distance (P2-P1) as shown on the left of Fig. 6.9.

On the other hand, a saturation effect is observed in the transitions (P2<) sitting on high threshold DAC values. This saturation effect manifests itself in systematically reduced gains for high threshold DAC values, as can be seen on the right of Fig. 6.9. Thus, this led us to select the P2-P1 in order to determine the breakdown voltage for all the channels. The statistical error of the gain is obtained from the uncertainties of determining the transitions of first and second photo electron transitions coming from the algorithm,  $\sigma_{P2-P1} = \sqrt{\sigma_{P1}^2 + \sigma_{P2}^2}$ , then the error is of the order of 1.5 DAC. In order to reduce this error, both 3 comparators are used, calculating the mean gain and mean gain error using:

$$Mean(P2 - P1) = \frac{\sum_{comp=1}^3 P2_{comp} - P1_{comp}}{3}$$

$$\sigma_{Mean(P2-P1)} = \frac{\sqrt{\sum_{comp=1}^3 \sigma_{P2_{comp}-P1_{comp}}^2}}{3}$$

In order to do this, it should be ensured that all three comparators should exhibit the same gain. The gain P2-P1 of eight channels for three comparators is almost the same within one threshold DAC. Thus, this allows us to find the average gain and error coming from all three comparators as explained above.

A series of lab measurements led to a more scrutinized study. The P2-P1 distance for different operating voltages is used and  $V_{offset} \approx 0.1V$  is set to its minimum value, such that  $V_{op} \approx V_{ov} + V_{br}$  as given from equation (5.1), in order to determine the breakdown voltage. The preliminary results show that it is necessary to increase the number of operating voltages considered. Thus, from 4 operating voltages we increase the number to 8. Moreover, a series of four repetitive measurements are conducted, under monitoring the temperature of SiPM. It is important to ensure that there are no gain variations due to the temperature variations since a difference of 57 mV/C° is expected from EPFL [58].

A temperature monitoring system is built using two digital temperature sensors Dallas DS18B20 connected to a Raspberry Pi. The sensor values are read out by means of a python code [59]. These two temperature sensors are attached as close as possible to SiPMs. The mean temperature from these two sensors with its standard

---

<sup>2</sup>École polytechnique fédérale de Lausanne

deviation is shown in Fig. 6.10. A gradual increase in temperature is observed, however, it is limited to 0.5 C°.

Only eight channels are selected for this study. The breakdown voltage distribution consisting of four different measurements for each of the eight channels is shown in Fig. 6.11. In the next table the mean breakdown voltage value and the standard deviation for each channel as well as the reference values are shown:

Channel	PACIFICr4		reference values from EPFL [58]	
	Mean [V]	Std [V]	Breakdown voltage [V]	Uncertainty [V]
32	51.51	0.04	51.02	0.27
33	50.51	0.01	51.01	0.17
34	51.05	0.02	51.03	0.47
35	50.77	0.02	51.01	0.18
36	51.44	0.04	51.01	0.17
37	53.18	0.01	51.01	0.15
38	51.05	0.07	51.06	0.52
39	50.95	0.01	51.07	0.15

The standard deviation that is reported is the statistical uncertainty. Beside this exist several systematic uncertainties such as the aforementioned saturation effect and the reduction of the distance between DC baseline and first photo-electron transition. These systematic uncertainties are the reason why the measurements are in agreement only for three channels, namely 34, 38 and 39.

It is necessary to check why the channel 37 has so different breakdown voltage. Investigating the S-curves, it is observed that the effect of assigning 1<sup>st</sup> photon to DC baseline influences the second photon transition P2 as well as shown in Fig. 6.12. This assignment of the second photon transition to DC baseline is more intensive for low operating voltages. One potential solution to avoid saturation is to trim the DC baseline towards to lower threshold DACs. Nevertheless, this is not possible as explained in the section 6.

### 6.2.3 Verification of $V_{offset}$

To ensure that these 3 channels are indeed unaffected by the aforementioned effects, one can use the well defined  $V_{offset}$ . By tuning it, any difference can be observed in the extrapolation of the breakdown voltage. It is known that  $V_{offset}$  has a dynamic range of 100-800mV divided in steps of 50 mV as shown in Fig .4.5. It can be adjusted linearly only between 100mV and 600mV. Thus, these two boundaries are used allowing a difference of 500 mV. To do so, two different sets of the same operating voltages used, while for each a different  $V_{offset}$  value of 100mV and 600mV have been selected. One should expect that these two measurements should lead to breakdown voltages having a difference of 500mV. The extrapolated breakdown voltages of channel 38 using these two different  $V_{offset}$  is shown in Fig. 6.13

The measured difference of the extrapolated breakdown voltages is shown in the table 6.1. This is a second verification that indeed these three channels are unaffected and

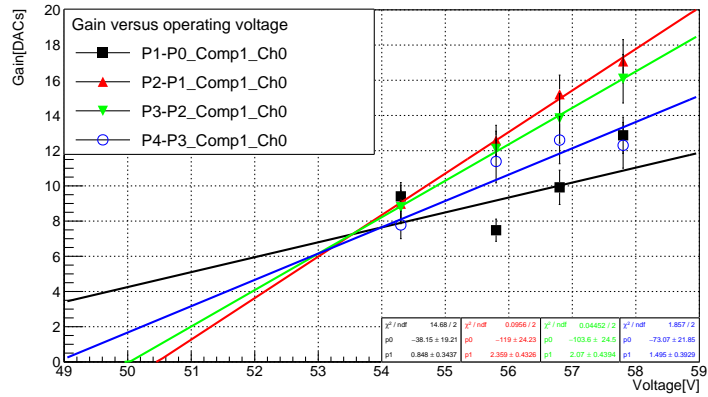


Figure 6.8: The extrapolation of breakdown voltage considering different distances between different transitions.

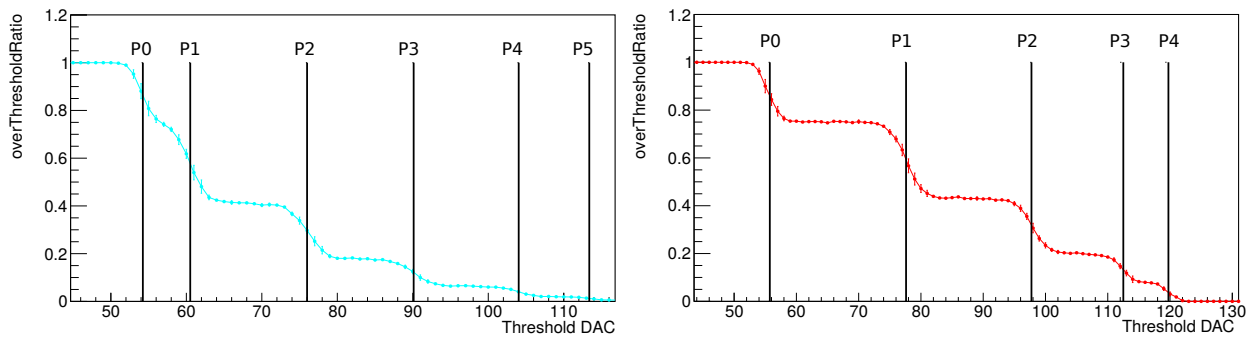


Figure 6.9: The left S-curve the distance P1-P0 is smaller with respect to P2-P1. While, on the right S-curves shows that the distances P4-P3, P3-P2 are subjected to saturation. Thus, P4-P3, P3-P2 and P1-P0 can not be used for the extrapolation of breakdown voltage.

in turn can be used for the extrapolation of the breakdown voltage.

### 6.2.4 Linearity region

Since the saturation affects the linearity of PACIFIC. A dedicated study is performed in order to specify the linear region of PACIFIC.

Two different parameters play an important role for the saturation. First is the DC baseline (P0) position. Since, if the DC baseline is placed close to the saturation area, then even the P1 is going to be experienced saturation. The second parameter is the operating voltage. Increasing the operating voltage, the gain is increased and therefore the transitions are shifted towards the saturation area.

The number of threshold DAC value where the transition occurs versus the number of transition number is plotted. Then, a line is drawn connecting the transitions

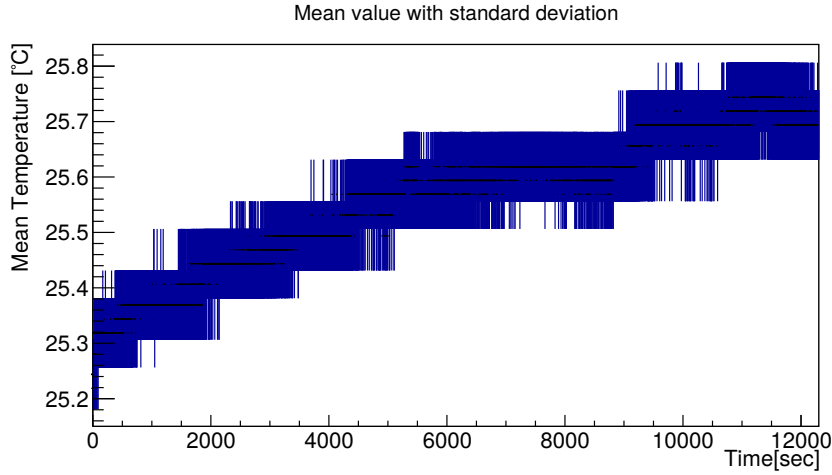


Figure 6.10: The temperature evolution over the time of measurement.

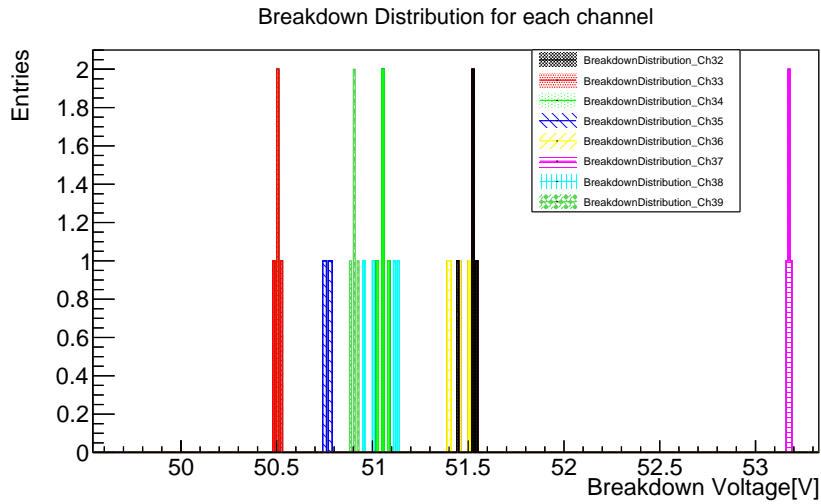


Figure 6.11: The distributions of the breakdown voltages for 8 channels.

points P1 and P3 as shown in Fig. 6.14. If the PACIFIC is linear then the line should pass through the P2 as well. The P1-P0 is discarded due to its reduced gain which some channels have as explained above.

Thus, the distance between the line and point P2 (residual) can be considered as a criterion to evaluate the linearity. A loose criterion of around 2 DACs is allowed in order to be considered linear, since the statistical error of the transition is around 1 DAC. For different operating voltages the residuals of P2 are calculated. Once any of the residual is above the maximum tolerance of 2 DACs then the region between the P1 and P3 is defined as the maximum operating linear region of PACIFIC. The maximum residual found for the channel 33 is 2.1 DAC as shown in the left Fig. of 6.15

The limit of linear region of PACIFICr4 is around 110 if the P1 is positioned on

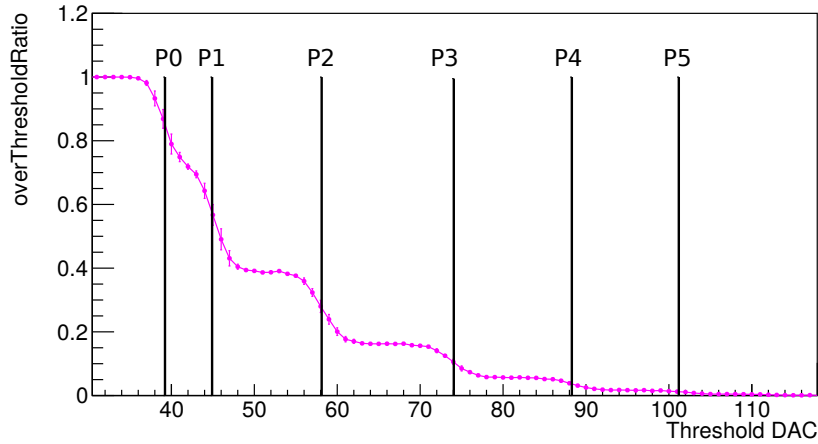


Figure 6.12: The assignment of  $2^{nd}$  p.e to  $1^{st}$  reduces the distance of P2-P1 inducing a wrong breakdown voltage determination.

Channel	Breakdown voltage Difference[V]
34	0.61
38	0.49
39	0.59

Table 6.1: The breakdown voltage difference using different  $V_{offset}$  values for channel 34,35 and 37 are shown.

the 76 threshold DAC as shown on the right side of Fig. 6.15. This is a specific case, however it is not going to vary dramatically from PACIFIC to PACIFIC and channel to channel.

The linear region depends on this limit (110) and the DC baseline position. If for instance, the P1 is lower than 76 then the linear region can be limited even lower than 110 threshold DAC. In this case it is still not linear if the gain is so high that the P1-P3 distance is bigger than 40-50 threshold DACs

## 6.2.5 Calibration of threshold DACs

The calibration is dedicated to extract the relation between the thresholds DACs and photo-electrons is similar as described in section 5.3.3. However, in the case of PACIFICr4, the thresholds are set for each channel individually. The calibration allows the photo-electrons to be expressed in terms of threshold DACs for each channel. Thus, we know the exact threshold DAC where the 1.5, 2.5 and 4.5 photo-electron occur and can be used in the clusterization algorithm.

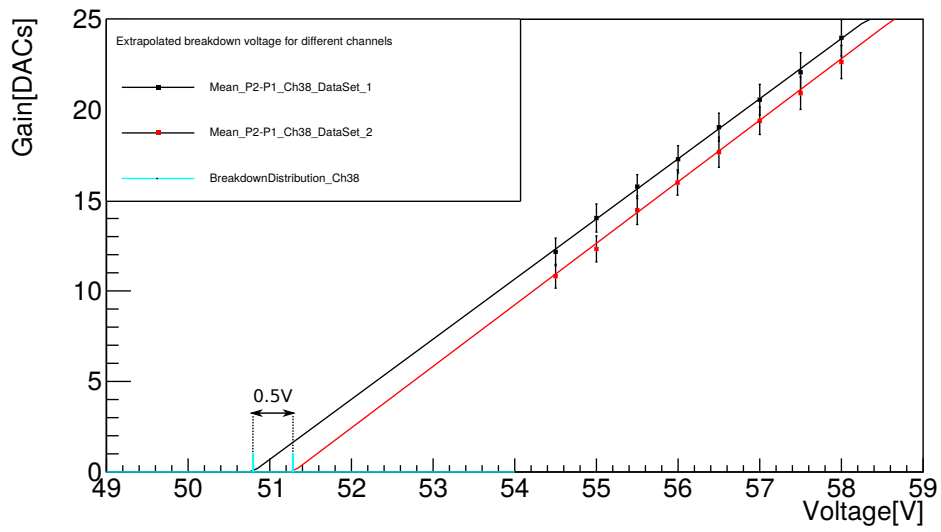


Figure 6.13: The extrapolation of these two different data sets lead to breakdown voltages having an approximate difference of 0.5V

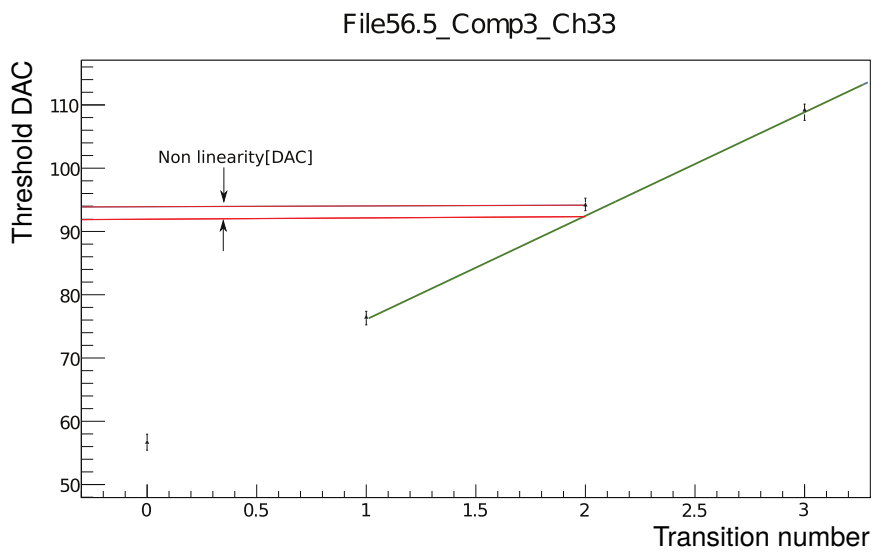


Figure 6.14: The distance between the green line and the P2 indicating with red color lines is presenting the non linearity [DAC].

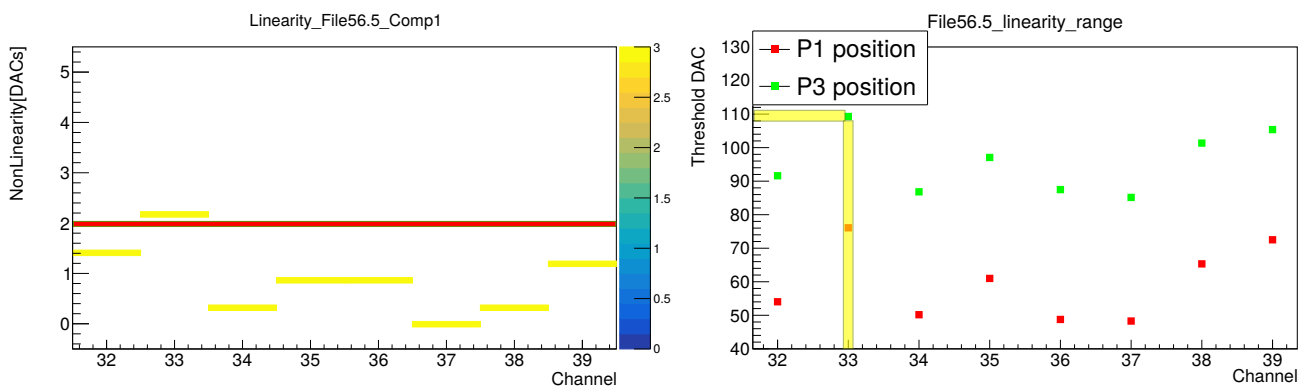


Figure 6.15: The residuals of all 8 channels are calculated. The residual of channel 33 exceeds the limit of Non Linearity (left). The P1 and P3 are shown (right) for each channel. The channel 33 is selected due to the non linearity behaviour. The P3 position is 109 DAC which considered the end of the linear region (right).

## 6.3 Beta source measurements

Using the same experimental setup as is used with the PACIFICr3 described in section 5.1.2, however, we used HQR 2016 Hamatsu SiPMs instead of HQR 2015. Measurements with an asynchronous beta source are conducted as described in section 5.4.

### 6.3.1 Delay Scan

A delay scan is employed in order to find the best delay time when the integration is the best within one bunch crossing. The process is described in section 5.4.2. The signal integration is shown in Fig. 6.16 for 3 bunch crossings while the delay time is changing.

A comparison with the delay scan of PACIFICr3 reveals that the PACIFICr4 is capable of integrating the signal more efficiently. Since PACIFICr4 presents an integration plateau above 70% for 11 ns. While, for the PACIFICr3 the corresponding plateau is for 7 ns. An important difference is observed on the maximum integration value which are 75.21 % and 79.85 % for PACIFICr3 and PACIFICr4, respectively.

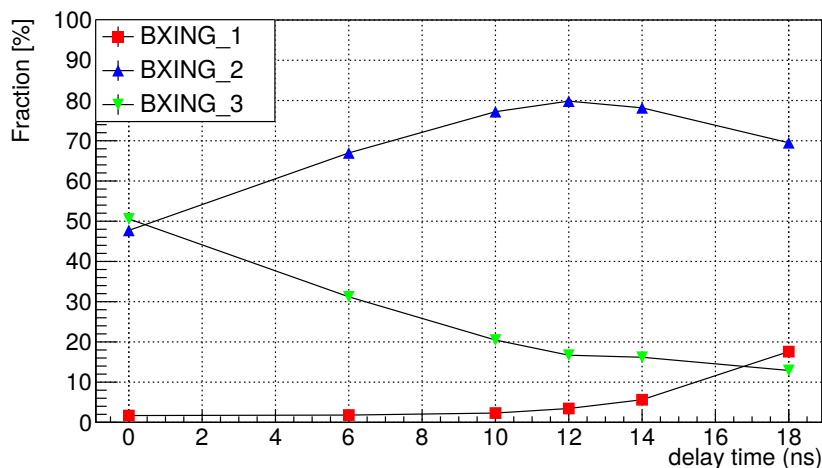


Figure 6.16: The delay scan indicates that the delay of 12 ns is the optimum.

### 6.3.2 Finetiming

A beta source is positioned on the fibre mat as shown in Fig. 5.20 resulting in a source profile. In this case the SiPM channel 10 is placed at the center of the source profile and should receive the most signal. The channel 10 and best bunch crossing 1 are selected in order to present the finetiming histogram for PACIFICr4 as shown in Fig. 6.17. An explanation of finetiming can be found on the section 5.4.1. One can notice the wider plateau of PACIFICr4 shown in Fig. 6.17 with respect to the

corresponding finetiming plot of PACIFICr3 shown in Fig .5.24. In the finetiming plot, a plateau of 14 ns is presented considering 15% variations on the y axis.

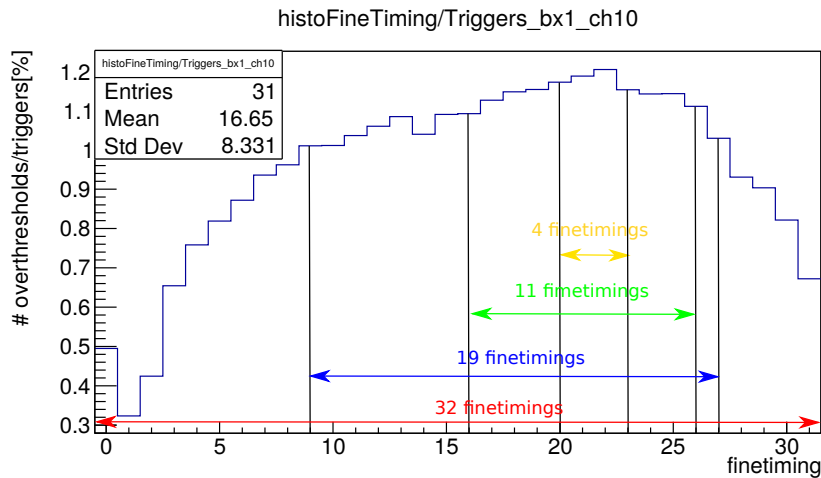


Figure 6.17: The finetiming histogram of PACIFICr4 exhibits a wider integration plateau with respect to the arrival time of the signal. The different color arrows show the selected areas of finetimings for further processing.

### Clusterization studies

For applying clusterization, the same setup is used as for PACIFICr4, presented in section 5.1. Moreover, the position of the beta source is above the fibre mat as shown in Fig 5.20. However, the latest SiPMs version of Hamatsu, that is H2016 is used. In addition, the following threshold settings  $T_{high} = 4.5$  p.e,  $T_{middle} = 2.5$  p.e and  $T_{low} = 1.5$  p.e are used in the cluster algorithm.

### 6.3.3 Threshold bit pattern

The threshold bit patterns give an insight of integration efficiency. In order to investigate which selection window of finetimings is the most appropriate, four different cases of selecting different number of finetimings are considered. The four used finetiming ranges are  $[0, 31]$ (32 finetimings),  $[9, 27]$ (19 finetimings),  $[16, 26]$ (11 finetimings) and  $[20, 23]$  (4 finetimings). They are shown in the Fig. 6.17.

For each case, the number of counts per bit pattern ( $T_{high}$ ,  $T_{middle}$  and  $T_{low}$ ) are divided by the number of bit patterns considering all 32 finetimings as shown in Fig 6.18.

It is observed that there is a considerable increase from 11 to 19 finetimings on the number of counts per bit pattern. An increase in the number of finetimings (11  $\rightarrow$  19) of 57.8% induces an increase of the counts per bit pattern of 56.5% , 55.5% and 60.6%. The biggest increase is observed for high threshold bit patterns.

It is necessary to normalize the counts per bit pattern for each group of finetimings.

This allows to determine the percentage of each bit pattern for the aforementioned cases of finetimings as shown in the following table.

finetimings	$TH_{low}$ [%]	$TH_{middle}$ [%]	$TH_{high}$ [%]	SUM [%]
32	29.8	41.5	28.7	100
19	16.9	41.9	41.2	100
11	16.6	40.5	42.9	100
4	16.2	38.2	45.6	100

The wider selection window of 19 finetimings with respect to 11 finetimings show an significant increase of statistics without a decrease in the relative percentage of  $TH_{high}$  bit pattern (42.9[%]  $\rightarrow$  41.2[%]). The optimum selection window is 19 finetimings considering a compromise between integration and statistics.

It is also noticeable that decreasing the number of finetimings considered, the percentage of  $TH_{high}$  is not increased significantly, while the  $TH_{high}$  is higher than  $TH_{middle}$  and  $TH_{low}$ , which is the manifestation of the integration efficiency of this finetiming area.

A comparison between PACIFICr3 and PACIFICr4 bit patterns can not be done considering 32 finetimings, since the finetiming plots are different as shown Fig 5.24 and Fig .6.17. However, this can be done for the plateau area of finetimings exhibiting the most integration, that is four finetimings. A comparison for this case is shown in the following Table.

ASIC version	finetimings	$TH_{low}$ [%]	$TH_{middle}$ [%]	$TH_{high}$ [%]	SUM [%]
PACIFICr3	4	19.2	17.8	63.0	100
PACIFICr4	4	16.2	38.2	45.6	100

This shows an important difference on the bit patterns of  $TH_{middle}$  and  $TH_{high}$  thresholds between these two PACIFIC versions. This is an indication that the  $TH_{middle}$  and  $TH_{high}$  thresholds may have not been set correctly for PACIFICr4. This shows that the  $TH_{high}$  threshold is set too high while the  $TH_{middle}$  is too low. If this is the case, this will influence the number of bit patterns observed, however the relative percentage differences on the bit patterns considering different finetimings as is investigated above will be the same.

### 6.3.4 Cluster distribution/size

Applying clusterization considering only 4 finetimings and bunch crossing 1 (the most integrated), a cluster distribution is shown on the left side of Fig. 6.19. It can be seen that this distribution differs from the one measured with PACIFICr3, shown in Fig. 5.26. The reason behind of the unexpected drop in the center of the source profile is the wrong settings of  $T_{high}$  and  $T_{middle}$  thresholds for some channels. The  $T_{high}$  and  $T_{middle}$  are set too high and too low, respectively. The right side of Fig. 6.19 shows the distribution of frequency of high threshold passed. It shows the same deficit as the cluster distribution.

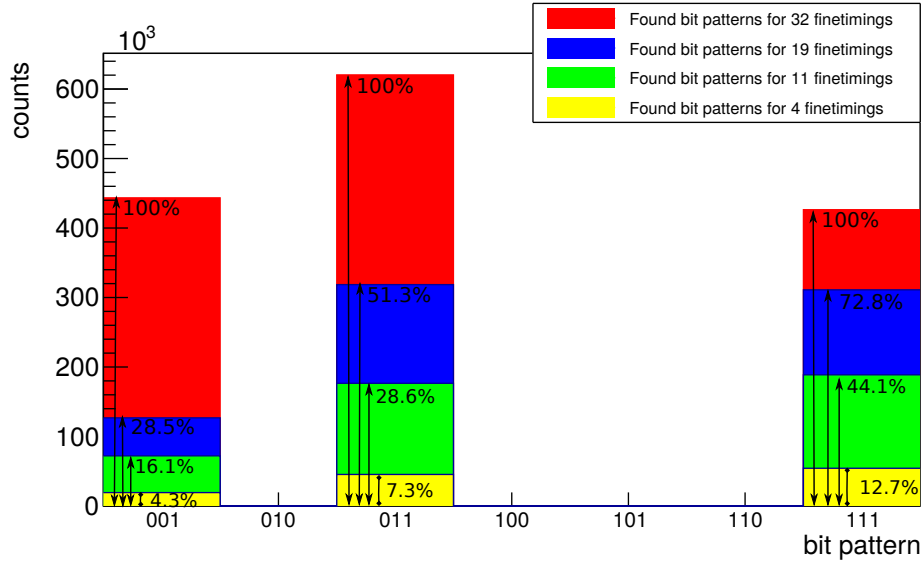


Figure 6.18: For  $T_{high} = 111$ ,  $T_{middle} = 011$  and low  $T_{low} = 001$  thresholds, the percentages for different finetiming groups are shown.

The verification of threshold settings can be done directly by investigating the calibration of the channel which exhibits a reduced number of counts over third threshold. It turns out that indeed the thresholds have not been set correctly for those channels. For clarity reasons the threshold settings of fourth channel is presented in Fig. 6.20, which has not passed the high threshold at all as shown on right of Fig. 6.19. The reason of the failure of setting correctly the  $T_{high}$  is the saturation effect as it has been described before. There is no 4.5 p.e which is required by the cluster algorithm.

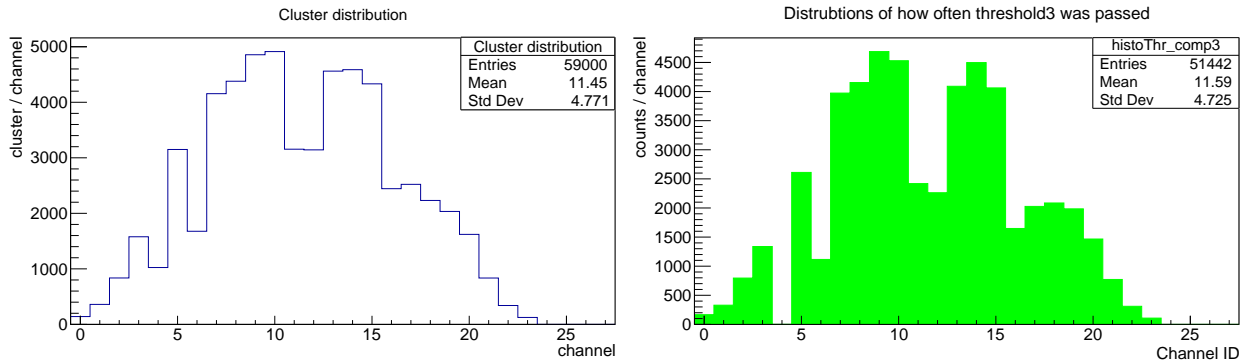


Figure 6.19: The cluster distribution of PACIFICr4 (left). The distribution of high threshold passed for bunch crossing 1 (right).

The normalized cluster size distribution is shown in the Fig. 6.21. The following table shows the cluster size with their corresponding probability.

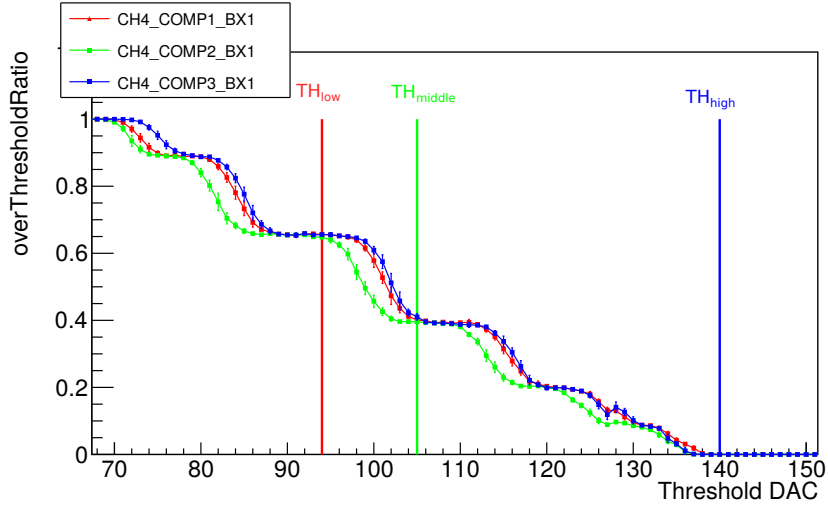


Figure 6.20: The S-curves of three comparators of channel four and their corresponding threshold settings are shown. It is clear that the  $T_{high}$  has been set too high since there is no clear 6<sup>th</sup> transition, that is 5<sup>th</sup> p.e. such that the threshold to be set on 4.5 p.e.

Cluster size[ch]	%
1	49.9
2	44.9
3	4.5
4 >	0.7

The most probable value is cluster size 1. From PACIFICr3 studies a cluster size distribution is expected as shown in Fig. 5.27 and table 5.2 (0 cm case). The most probable value of the cluster size is two channels.

In order to investigate the impact of the overestimation of the  $T_{high}$  threshold, measurements from PACIFICr3 and PACIFICr4 have to be compared considering only 4 finetimings and the best integrated bunch crossing. The following quantities are used for further analysis.

- Cluster distribution entries
- Single channel cluster distribution entries
- Entries of passed  $T_{high}$  threshold

In case that the  $T_{high}$  threshold passed, it is directly counted as a cluster. The entries of passed  $T_{high}$  threshold are divided into single channel cluster and multiple channel cluster. The contribution of  $T_{high}$  threshold to the formation of single and multiple channel clusters can be quantified and evaluated as shown in the following table.

	PACIFICr3	PACIFICr4
single channel cluster[%]	8.1	49.9
multi channel clusters[%]	91.9	50.1
sum	100	100
single channel cluster/ $T_{high}$ entries	4.3	57.3
multi channel clusters/ $T_{high}$ entries	95.7	42.8
sum	100	100

The fact that the 95.7[%] of the  $T_{high}$  threshold is distributed into the multiple channel clusters manifest the strong contribution of  $T_{high}$  threshold into the formation of clusters with cluster size bigger than two channels for PACIFICr3. While the overestimation of  $T_{high}$  threshold for PACIFICr4 led to less  $T_{high}$  thresholds passed inducing an effective decrease (95.7[%]  $\rightarrow$  42.8[%]) of their contribution to the formation of the multiple channel clusters. Thus, the single channel clusters are significantly increased with respect to the multiple channel clusters due to the loss of  $T_{high}$  threshold for PACIFICr4, resulting in a cluster size distribution with the most probable value to be 1 channel.

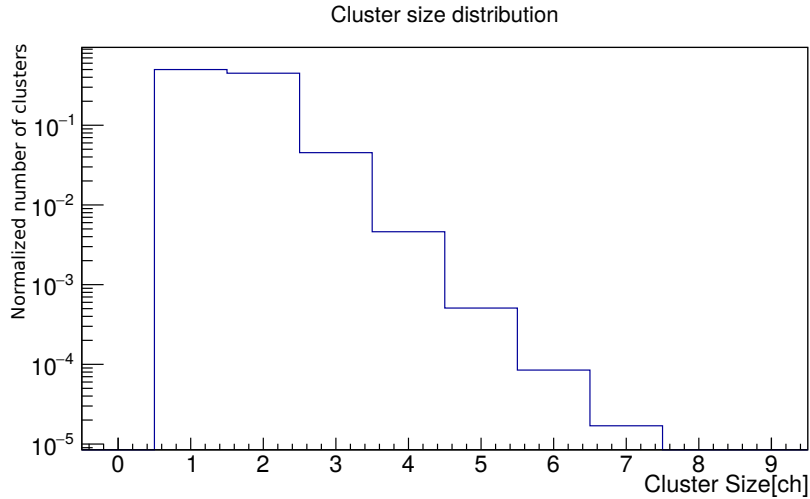


Figure 6.21: The normalized cluster size distribution using PACIFICr4 and HQR 2016 Hamamatsu SiPMs.

## 7 Conclusion

The LHCb detector will undergo a major upgrade during the second LHC long shutdown in 2019/20. The current outer tracker placed downstream of the LHCb dipole magnet, based on the drift tube detectors, will be replaced by the Scintillating Fibre (SciFi) Tracker in order to cope with higher instantaneous luminosities and an increased readout rate of 40 MHz using a trigger-less system. The Tracker is made of scintillating fibres with a diameter of  $250\mu\text{m}$ , read out by silicon photo-multipliers (SiPM) aiming to reconstruct hits with a spacial resolution better than  $100\mu\text{m}$ . The SiPMs are read out by a custom ASIC, so-called low-Power ASIC for the sCIntillating FIBres traCker (PACIFIC) designed to digitize the SiPM signals. In this thesis, the characterization results of the two latest PACIFIC versions, namely PACIFICr3 and PACIFICr4, are presented. Using the implemented features, a uniform response of channels was possible for both PACIFICr3 and PACIFICr4, respectively. This was achieved only for 16 channels for PACIFICr3 due to the mismatch of the clock distribution between groups of 16 channels.

The calibration of the SiPMs was successfully completed allowing to extract the photons in terms of thresholds DACs for PACIFICr3. For PACIFICr4, due to the saturation effect the high thresholds are not determined correctly.

A beta source generating a random signal was used to study the immunity of signal arrival with respect to the integration window of PACIFIC. The PACIFICr3 and PACIFICr4 exhibited an integration plateau of 7 ns and 11ns, respectively. Eventually, the PACIFICr4 was capable of successfully fulfilling the requirements of SciFi detector.

Clusterization studies were performed in order to reconstruct the source profile. In the case of PACIFICr3, this was successful since the expected source profile was observed. In contrast, in PACIFICr4 not the same source profile as was observed in PACIFICr3 could be reconstructed due to the incorrect high thresholds settings.

A part of this study was devoted to the characterization of SiPMs using PACIFICr4. This was partially successful since PACIFICr4 is suffering from systematic effects rendering the extrapolation of breakdown voltage difficult and correct under certain circumstances.

### 7.0.5 Outlook

One could say that despite certain features PACIFICr4 is already functional and fulfils all requirements for the usage in the experiment. All features are overcome with the next version. PACIFICr5 is going to maintain the wide integration plateau. In addition, the differential output included in PACIFICr5 will allow a threshold scan for 64 channels using common thresholds. The trimming mechanism will be fully

functional allowing to shift the DC baseline to negative direction of threshold DACs. Combined with the higher dynamical range of the threshold DACs, it will allow to choose more photon transitions for the extrapolation of the breakdown voltage.

# Part I

## Appendix

## Threshold DACs in terms of voltage

The threshold DACs are defined in terms of mV. Thus, the limit of around 300 mV corresponds to 150 threshold DAC value as shown in Fig .1.

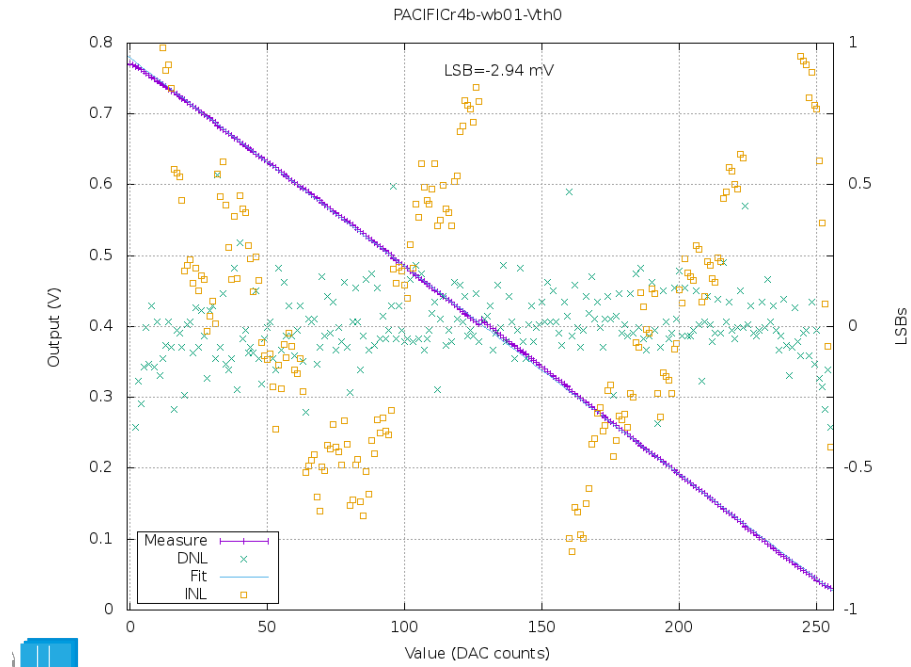


Figure .1: The threshold DACs of first comparator in terms of mV.

# A Lists

## A.1 List of Figures

2.1	Detector positions along CERN accelerator chain. Taken from [9] . . .	10
2.2	All elementary particles with their masses and spins described by Standard model. Taken from [12] . . . . .	11
2.3	The decay of $B_s^0$ is forbidden in SM through the direct flavour changing neutral current process, due to the $Z^0$ can not couple directly to quarks of different flavours. However, this transition is allowed for higher order transitions, resulting in a reduced probability of scattering amplitude due to the increased number of interaction vertices considered. Taken from [17] . . . . .	13
2.4	A simulation of the cross section for the production of $\bar{b}b$ quark pairs as a function of the polar angles $\theta_1$ and $\theta_2$ with respect to the beam axis. The red color region points the acceptance area of the LHCb detector, while the blue region the area which is not included. Taken from [20] . . . . .	14
2.5	Schematic view of the current LHCb experiment. Taken from [21] . .	15
2.6	Schematic view of the upgraded LHCb experiment. Taken from [21].	17
3.1	Left side: The expected 1 MeV neutron equivalent fluence at $z = 783$ cm after an integrated luminosity of $50 \text{ fb}^{-1}$ . Right Side: The expected dose in the $x - y$ plane at $z = 783$ cm after an integrated luminosity of $50 \text{ fb}^{-1}$ . Taken from [21] . . . . .	20
3.2	One station which consisted of 4 detection layers ("X","U","V" and "X") (left). The SciFi view with the squared cut in the middle for the beam pipe (right). Taken from [38] . . . . .	21
3.3	Fibre schematic showing the light production and propagation within the fibre thanks to total internal reflection. Taken from [21]. . . . .	23
3.4	Wavelength spectrum for three different position from the SiPMs. Taken from [21]. . . . .	24
3.5	The top schematic shows a single cast fibre mat before performing a longitudinal cut. While, on the bottom two adjacent mats are shown after the mats have been cut to a width of 130.60 mm. The grey fibres indicate that SiPMs can not read out them, since they lose the majority of transmission light due to their cut. Taken from [21] [Modified]. . . . .	25
3.6	A view of module showing its components. Taken from [34] [Modified]	25

3.7	A band gap diagram showing the different sizes of band gaps for conductors, semiconductors, and insulators. The Fermi energy is defined as the highest occupied energy level of a material at absolute zero temperature and is placed between the conduction and valence bands. Taken from [43]. . . . .	27
3.8	A schematic before and after merging the p-type with n-type semiconductor is shown. Taken from [44]. . . . .	28
3.9	A schematic of a typical SiPM channel consists of multiple single micro cells, that is APDs including their quenching resistors and interconnections between them. Taken from [45]. . . . .	29
3.10	Photo taken under the microscope showing the 64 channels of a single die of a Hamamatsu HRQ H2016. Taken from [47]. . . . .	31
4.1	The physical structure of N-Mos Transistor (left) and its characteristic curve of I-V(right). Taken from [48] and [49] . . . . .	33
4.2	PACIFIC evolution. . . . .	34
4.3	The SiPM simulated model (left) and the model parameters (right) [38]. . . . .	35
4.4	The current conveyor and the transimpedance amplifier. Taken from [38] . . . . .	36
4.5	The voltage anode adjustment ranges between 100 to 800mV with an approximate step of 50 mV. Taken from [51]. . . . .	37
4.6	For two different cases of positioning a beta source close to the mirror (left) and close to SiPMs (40cm) (right) resulting in a different shaper signal of PACIFIC. Close to SiPMs a reflected signal is observed coming after 25ns validating the rule of the mean propagation time of light along the fibre is 6 ns/m. On the left figure, the DC baseline, 1 <sup>st</sup> and 2 <sup>nd</sup> p.e have been pointed starting from low to high voltage values. . . . .	38
4.7	The interleaved gated integrators. Taken from [51] . . . . .	39
4.8	The track and hold circuit. Taken from [51] . . . . .	39
4.9	The generation of three groups of common thresholds for 64 channels. Taken from [51] [Modified]. . . . .	41
4.10	Selection between common and local threshold DACs for each channel [51] [Modified]. . . . .	41
4.11	The available output signals for debugging of the analogue and digital part of PACIFIC. At the output of every two channels, an encoder and serialization block is included encoding the three outputs of the channel comparators to two bits. Taken from [51]. . . . .	43
4.12	The two different cases where a particle track is indicated with red color can induce clusters fulfilling the minimum requirements as shown on the top of figure. . . . .	44

4.13	A typical S-curve (green) and its differential (red) are shown for channel 37 of PACIFICr4. The perpendicular lines (black) intersect the S-curve on the transition positions or alternatively on the peak positions of differential S-curve pointing the corresponding threshold DAC. Starting from left to right, the DC baseline, 1 <sup>st</sup> , 2 <sup>nd</sup> , 3 <sup>rd</sup> , 4 <sup>th</sup> and 5 <sup>th</sup> p.e (photo-electrons) are shown. . . . .	46
5.1	The aluminium lightbar with the optical fibre glued into one side (left) and the experimental setup dedicated for the SiPM calibration. (right). . . . .	48
5.2	The trigger is shown(left) and the beta source experimental setup (right). . . . .	49
5.3	The DC baseline distribution of 64 channels for two PACIFICr3 ASICs without any alignment. . . . .	50
5.4	The DC baseline distribution of 64 channels for two PACIFICr3 ASICs after enabling CMC. . . . .	51
5.5	The alignment of DC baseline of 64 channels of comparator 1 after applying trimming. . . . .	52
5.6	A linear fit of threshold DAC versus trim DAC for 16 channels of comparator 1 (left) is applied. A histogram with the slopes of the linear fit for 16 channels (right) is shown . . . . .	52
5.7	The DC baseline difference between two integrators of 64 channels for all three comparators before (left) and after trimming (right). . . . .	53
5.8	The DC baseline positions for 64 channels for different operating conditions. . . . .	54
5.9	The arrival time of signal exact between two integration windows, sharing the integration of signal. . . . .	55
5.10	The arrival time of signal within the integration window, allowing full integration within one bunch crossing. . . . .	55
5.11	The calculated observed gain is defined as the distance between the transitions in terms of threshold DACs. . . . .	56
5.12	The S-curve for proper delay time and improper delay time. . . . .	57
5.13	The delay of 5 ns is selected since exhibits the biggest gain. The level values correspond to the overThreshold values. Note that the counting of photon-electrons starts from high threshold DAC value going to lower threshold DAC values for bigger number of photon-electrons. Thus, the transition 0 is the DC baseline, the transition 1 is the first p.e, etc. The lower the threshold DAC the transition has, the higher the gain is. . . . .	57
5.14	Before $V_{offset}$ tuning. . . . .	58
5.15	After $V_{offset}$ tuning. . . . .	58
5.16	The transition positions of DC baseline(black), 1 <sup>st</sup> (red), 2 <sup>nd</sup> (green), 3 <sup>rd</sup> (blue) and 4 <sup>th</sup> (yellow) p.e for 16 channels (left). The position distributions of each transition for 16 channels (right). . . . .	58

5.17	The calibration of threshold DACs as a function of p.e of 16 channels for the first comparator allows to determine the thresholds as follows: 1.5 p.e = 83 DAC, 2.5 p.e = 58 DAC and 3.5 p.e = 28 DAC. Thus, for setting the low threshold common for 16 channels, the 83 threshold DAC value is used. . . . .	59
5.18	Once a particle passes through the fibre mat and trigger, two signals are made. The trigger (green) and particle (red) signals arrive at the FPGA with constant time difference. . . . .	60
5.19	Driving both trigger (green) and particle (red) signals in oscilloscope. The $t_{delay}$ is determined to 10 bunch crossing (250 ns). Then, one should look in the memory of FPGA back in time by 6 BXINGS and fetch 8 bunch crossings (pink). The particle signal is going to be distributed in the third bunch crossing of these 8 fetched bunch crossings. The trigger arrival in FPGA is stamped with the TDC counter so-called finetiming (Finetiming 15). . . . .	61
5.20	The position of beta source on the fibre mat without collimator. The channel 8 is considered as the "best channel". . . . .	63
5.21	The delay time of 9 ns of delay unit is selected since exhibits the most integration within bunch crossing 3. An integration plateau above 70% for 7 ns with a maximum value of 75.21 % are observed. . . . .	64
5.22	The finetiming distribution for the best bunch crossing 3 and best channel 8. . . . .	65
5.23	The finetiming histogram including all triggers gives an inspection of the quality of firmware. . . . .	66
5.24	The unbiased finetiming histogram for the best bunch crossing 3 and best channel 8, the yellow area marks the selected finetimings for further processing. . . . .	67
5.25	The bit patterns of measurement before (red) and after (yellow) the selection of the best 4 finetimings (marked with yellow in Fig .5.24) resulting a decrease of 96 %, 93 % and 83 % for low, middle and high thresholds, respectively. However, the bit pattern of high threshold is relatively larger than the other bit patterns after the selection of four finetimings. . . . .	67
5.26	The location from $\beta$ -tracks after applying preselection of the best four finetimings of most threshold passed. . . . .	68
5.27	The cluster size distribution after applying preselection of the best four finetimings of most threshold passed. . . . .	68
5.28	The cluster distribution for the case where the position of beta source is in the collimator 2(left) and 20 (right) cm above the fibre mat results a flat source profile. . . . .	68
5.29	The beta source position in the collimator 2cm(left) and 20cm(right) above fibre mat. . . . .	69
5.30	The cluster size distributions for large data sets for the cases of positioning the beta source 2cm and 20 cm above fibre mat. . . . .	69

5.31	Three different cases of different neighbours are shown resulting three different S-curves. The photon transitions are clearly shown for the case of 2nd neighbour. . . . .	70
5.32	The two S-curves for beta source and light injection system shows that the transitions occur at the same threshold DAC. . . . .	70
6.1	The CMOS schematic diagram of hysteresis comparators circuitry are shown left and right side of figure, while the bias N-MOS transistor is marked with yellow color [57]. The drain, source and gate terminals are marked with red color. . . . .	72
6.2	The areas where current is adding and removing from the trim DACs inducing a positive and negative shift with respect to reference voltage of each channel (Vref) [57]. . . . .	72
6.3	Threshold scan using common thresholds for only 8 channels(left) and 64 channels(right) shows a shift of the DC baseline of two comparators. . . . .	73
6.4	The DC baseline difference between two integrators for 64 channels $\times$ three comparators after trimming alignment. . . . .	74
6.5	The DC baseline difference between two integrators for three comparators after trimming alignment can show the comparator mismatch. . . . .	74
6.6	The DC baseline position for 64 channels for different states considered. . . . .	75
6.7	The best delay time is 14 ns exhibiting the best integration. The six transitions of a S-curve with their overThresholdRatio levels are shown. Note that the PACIFICr4 S-curve is inverted compared with PACIFICr3 S-curves, this means that the counting of photon-electrons starts from low threshold DAC value going to higher threshold DAC values for bigger number of photon-electrons. Thus, the transition 0 is the DC baseline, the transition 1 is the first p.e, etc. The higher the threshold DAC the transition has, the higher the gain is. . . . .	76
6.8	The extrapolation of breakdown voltage considering different distances between different transitions. . . . .	79
6.9	The left S-curve the distance P1-P0 is smaller with respect to P2-P1. While, on the right S-curves shows that the distances P4-P3, P3-P2 are subjected to saturation. Thus, P4-P3, P3-P2 and P1-P0 can not be used for the extrapolation of breakdown voltage. . . . .	79
6.10	The temperature evolution over the time of measurement. . . . .	80
6.11	The distributions of the breakdown voltages for 8 channels. . . . .	80
6.12	The assignment of $2^{nd}$ p.e to $1^{st}$ reduces the distance of P2-P1 inducing a wrong breakdown voltage determination. . . . .	81
6.13	The extrapolation of these two different data sets lead to breakdown voltages having an approximate difference of 0.5V . . . . .	82
6.14	The distance between the green line and the P2 indicating with red color lines is presenting the non linearity[DAC]. . . . .	82

6.15	The residuals of all 8 channels are calculated. The residual of channel 33 exceeds the limit of Non Linearity (left). The P1 and P3 are shown (right) for each channel. The channel 33 is selected due to the non linearity behaviour. The P3 position is 109 DAC which considered the end of the linear region (right). . . . .	83
6.16	The delay scan indicates that the delay of 12 ns is the optimum. . . . .	84
6.17	The finetiming histogram of PACIFICr4 exhibits a wider integration plateau with respect to the arrival time of the signal. The different color arrows show the selected areas of finetimings for further processing. . . . .	85
6.18	For $T_{high} = 111$ , $T_{middle} = 011$ and low $T_{low} = 001$ thresholds, the percentages for different finetiming groups are shown. . . . .	87
6.19	The cluster distribution of PACIFICr4 (left). The distribution of high threshold passed for bunch crossing 1 (right). . . . .	87
6.20	The S-curves of three comparators of channel four and their corresponding threshold settings are shown. It is clear that the $T_{high}$ has been set too high since there is no clear 6 <sup>th</sup> transition, that is 5th p.e such that the threshold to be set on 4.5 p.e. . . . .	88
6.21	The normalized cluster size distribution using PACIFICr4 and HQR 2016 Hamamatsu SiPMs. . . . .	89
.1	The threshold DACs of first comparator in terms of mV. . . . .	93

## A.2 List of Tables

5.1	The Mean DC baseline and RMS for two PACIFIC ASICs without alingnement and after enabling CMC. . . . .	51
5.2	The cluster size percentage for each different position of beta source . . . . .	65
6.1	The breakdown voltage difference using different $V_{offset}$ values for channel 34,35 and 37 are shown. . . . .	81

## B Bibliography

- [1] LHC Design Report, . URL [Link](#).
- [2] G. Aad et al. The ATLAS Experiment at the CERN Large Hadron Collider. *JINST*, 3:S08003, 2008. doi: 10.1088/1748-0221/3/08/S08003.
- [3] S. Chatrchyan et al. The CMS Experiment at the CERN LHC. *JINST*, 3:S08004, 2008. doi: 10.1088/1748-0221/3/08/S08004.
- [4] A. Augusto Alves, Jr. et al. The LHCb Detector at the LHC. *JINST*, 3:S08005, 2008. doi: 10.1088/1748-0221/3/08/S08005.
- [5] K. Aamodt et al. The ALICE experiment at the CERN LHC. *JINST*, 3:S08002, 2008. doi: 10.1088/1748-0221/3/08/S08002.
- [6] G. Anelli et al. The TOTEM experiment at the CERN Large Hadron Collider. *JINST*, 3:S08007, 2008. doi: 10.1088/1748-0221/3/08/S08007.
- [7] O. Adriani et al. The LHCf detector at the CERN Large Hadron Collider. *JINST*, 3:S08006, 2008. doi: 10.1088/1748-0221/3/08/S08006.
- [8] J. L. Pinfold. The MoEDAL Experiment at the LHC – a New Light on the Terascale Frontier. *J. Phys. Conf. Ser.*, 631(1):012014, 2015. doi: 10.1088/1742-6596/631/1/012014.
- [9] Michael Moll CERN, Geneva, Switzerland - ppt download. URL [Link](#).
- [10] Peter W. Higgs. Broken symmetries and the masses of gauge bosons. *Phys. Rev. Lett.*, 13:508–509, Oct 1964. doi: 10.1103/PhysRevLett.13.508. URL [Link](#).
- [11] Roel Aaij et al. Observation of  $J/\psi p$  Resonances Consistent with Pentaquark States in  $\Lambda_b^0 \rightarrow J/\psi K^- p$  Decays. *Phys. Rev. Lett.*, 115:072001, 2015. doi: 10.1103/PhysRevLett.115.072001.
- [12] Standard model particles. URL [Link](#).
- [13] B. A. Robson. The generation model of particle physics and the cosmological matter-antimatter asymmetry problem, 2016.
- [14] A. D. Sakharov. Violation of CP Invariance, c Asymmetry, and Baryon Asymmetry of the Universe. *Pisma Zh. Eksp. Teor. Fiz.*, 5:32–35, 1967. doi: 10.1070/PU1991v034n05ABEH002497. [Usp. Fiz. Nauk161,61(1991)].

- [15] mit physics annual 2006 Gabriella Sciolla. URL [Link](#).
- [16] T. N. Pham. CKM Matrix Elements. 2011.
- [17] CMS Collaboration and LHCb Collaboration. Observation of the rare  $s_0 \rightarrow \mu^+ \mu^-$  decay from the combined analysis of cms and lhcb data. *Nature*, 522 (7554):68–72, June 2015. ISSN 0028-0836. URL [Link](#).
- [18] Hamish Gordon. *The LHCb Detector*, pages 23–43. Springer International Publishing, Cham, 2014. ISBN 978-3-319-07067-4. doi: 10.1007/978-3-319-07067-4\_2. URL [Link](#).
- [19] Roel Aaij et al. Precision luminosity measurements at LHCb. *JINST*, 9(12): P12005, 2014. doi: 10.1088/1748-0221/9/12/P12005.
- [20] bbar production angle plot, . URL [Link](#).
- [21] LHCb Collaboration. LHCb Tracker Upgrade Technical Design Report. Technical Report CERN-LHCC-2014-001. LHCb-TDR-015, Feb 2014. URL [Link](#).
- [22] M. T. Alexander and LHCb VELO Group. LHCb VELO tracking resolutions. *Nuclear Instruments and Methods in Physics Research A*, 699:184–187, January 2013. doi: 10.1016/j.nima.2012.05.036.
- [23] LHCb - Large Hadron Collider beauty experiment. URL [Link](#).
- [24] Yu Guz and the LHCb collaboration. The lhcb hadron calorimeter. *Journal of Physics: Conference Series*, 160(1):012054, 2009. URL [Link](#).
- [25] X. Cid Vidal. Muon Identification in the LHCb experiment. In *Proceedings, 45th Rencontres de Moriond on Electroweak Interactions and Unified Theories: La Thuile, Italy, March 6-13, 2010*, 2010. URL [Link](#).
- [26] Letter of Intent for the LHCb Upgrade. Technical Report CERN-LHCC-2011-001. LHCC-I-018, CERN, Geneva, Mar 2011. URL [Link](#).
- [27] Heinrich Schindler. The LHCb upgrade. *PoS*, Hadron2013:128, 2013.
- [28] Federico Alessio. The LHCb upgrades. Apr 2017. URL [Link](#).
- [29] Karol Hennessy. LHCb VELO Upgrade. *Nucl. Instrum. Meth.*, A845:97–100, 2017. doi: 10.1016/j.nima.2016.04.077.
- [30] Federica Lionetto. LHCb Upgrade: Upstream Tracker. *PoS*, Vertex2014:009, 2015.
- [31] LHCb Collaboration. LHCb PID Upgrade Technical Design Report. Technical Report CERN-LHCC-2013-022. LHCb-TDR-014, Nov 2013. URL [Link](#).

- [32] Lorenzo Cassina. LHCb RICH Upgrade: an overview of the photon detector and electronic system. *JINST*, 11(01):C01025, 2016. doi: 10.1088/1748-0221/11/01/C01025.
- [33] Yu Guz. LHCb Calorimeter Upgrade. (LHCb-PROC-2013-051. CERN-LHCb-PROC-2013-051):8 p, Sep 2013. URL [Link](#).
- [34] Christian Joram, Ulrich Uwer, Blake Dean Leverington, Thomas Kirn, Sebastian Bachmann, Robert Jan Ekelhof, and Janine Müller. LHCb Scintillating Fibre Tracker Engineering Design Review Report: Fibres, Mats and Modules. Technical Report LHCb-PUB-2015-008. CERN-LHCb-PUB-2015-008, CERN, Geneva, Mar 2015. URL [Link](#).
- [35] Alfredo Ferrari, Paola R. Sala, Alberto Fasso, and Johannes Ranft. FLUKA: A multi-particle transport code (Program version 2005). 2005.
- [36] G. Battistoni et al. The FLUKA code: Description and benchmarking. In *M. Albrow and R. Raja, editors, Proceedings of the Hadronic Shower Simulation Workshop 2006 ,AIP Conference Proceeding 896, pages 31–49, 2007*.
- [37] Neus Lopez March and Matthias Karacson. Radiation studies for the LHCb tracker upgrade. Technical Report LHCb-PUB-2014-022. CERN-LHCb-PUB-2014-022. LHCb-INT-2013-003, CERN, Geneva, Feb 2014. URL [Link](#).
- [38] TWEPP 2014 - Topical Workshop on Electronics for Particle Physics (22-26 September 2014), . URL [Link](#).
- [39] T. O. White. Scintillating fibres. *Nuclear Instruments and Methods in Physics Research Section A: Accelerators, Spectrometers, Detectors and Associated Equipment*, 273(2-3):820–825, 1988. URL [Link](#).
- [40] M. Deckenhoff. Scintillating Fibre and Radiation Damage Studies for the LHCb Upgrade. URL [Link](#).
- [41] A Bay, F Blanc, S Bruggisser, O Callot, H Chanal, E Cogneras, A Comerma-Montells, M Deckenhoff, G Decreuse, M Demmer, V Egorychev, R Ekelhof, D Gascon, A Golutvin, E Graugès, O Grünberg, E Gushchin, Yu Guz, G Hae-feli, P Jatton, C Joram, M Karacson, B Leverington, R Lindner, N Lopez-March, T Nakada, M Patel, P Perret, A Puig Navarro, B Rakotomiarmanana, J Rouvinet, T Savidge, O Schneider, T Schneider, P Shatalov, B Spaan, E Thomas, G Veneziano, U Uwer, Z Xu, and H Yu. Viability assessment of a scintillating fibre tracker for the LHCb upgrade. Technical Report LHCb-INT-2013-004. CERN-LHCb-INT-2013-004. LHCb-PUB-2014-015, CERN, Geneva, Jan 2013. URL [Link](#). -.
- [42] C. Grupen and B. Shwartz. *Particle Detectors*. Cambridge Monographs on Particle Physics, Nuclear Physics and Cosmology. Cambridge University Press, 2008. ISBN 9781139469531. URL [Link](#).

- [43] Band gap - Energy Education, . URL [Link](#).
- [44] p-n junction, . URL [Link](#).
- [45] A technical guide to silicon photomultipliers (SiPM) | Hamamatsu Photonics, . URL [Link](#).
- [46] Nepomuk Otte. The Silicon Photomultiplier: A New Device for High Energy Physics, Astroparticle Physics, Industrial and Medical Applications. *eConf*, C0604032:0018, 2006.
- [47] A. Kuonen. Characterisation of Hamamatsu silicon photomultiplier arrays for the LHCb Scintillating Fibre Tracker Upgrade. TIPP 2017 , China Beijing, June 22-26 2017, 2017. URL [Link](#).
- [48] I-v characteristics. URL [Link](#).
- [49] Nmos structure.
- [50] Jose Mazorra De Cos. PACIFIC : The readout ASIC for the SciFi Tracker planned for the upgrade of the LHCb detector. Sep 2015. URL [Link](#).
- [51] Christian Joram and Ulrich Uwer. LHCb Scintillating Fibre Tracker Engineering Design Review: PACIFIC Readout ASIC. Technical Report LHCb-PUB-2016-013. CERN-LHCb-PUB-2016-013, CERN, Geneva, Apr 2016. URL [Link](#).
- [52] David Gascón Sergio Gómez. Pacific5.
- [53] J.H. Huijsing. *Operational Amplifiers: Theory and Design*. Kluwer international series in engineering and computer science. Kluwer Academic Publishers, 2001. ISBN 9780792372844. URL [Link](#).
- [54] Ana Barbara Rodrigues Cavalcante, Robert Jan Ekelhof, Laura Gavardi, Olivier Goran Girard, Roman Greim, Guido Haefeli, Xiaoxue Han, Christian Joram, Matthieu Kecke, Axel Kevin Kuonen, Blake Dean Leverington, Dominik Stefan Mitzel, Janine Muller, Max Neuner, Simon Nieswand, and Tobias Tekampe. LHCb Scintillating Fibre Tracker: Test Beam Report 2015. Technical Report LHCb-PUB-2015-025. CERN-LHCb-PUB-2015-025, CERN, Geneva, Nov 2015. URL [Link](#).
- [55] Angelo Rivetti. *CMOS: Front-End Electronics for Radiation Sensors*. CRC Press, 2017. ISBN 9781138827387. URL [Link](#).
- [56] Prashant Shukla. Energy and angular distributions of atmospheric muons at the Earth. 2016.
- [57] Albert Comerma. PACIFICr4b → PACIFICr5, MARCH 2017. URL [Link](#).

- [58] Axel Kevin Kuonen, Guido Haefeli, Maria Elena Stramaglia, and Olivier Goran Girard. Characterisation of the Hamamatsu MPPC multichannel array for the LHCb SciFi Tracker v.11.2016. Technical Report LHCb-INT-2017-006. CERN-LHCb-INT-2017-006, CERN, Geneva, Apr 2017. URL [Link](#).
- [59] Martin Baumann, Fabian Gehbart, Oliver Mattes, Sotirios Nikas, Vincent Heuveline. Development and implementation of a temperature monitoring system for HPC systems. In *Parallel-Algorithmen, -Rechnerstrukturen und -Systemsoftware (PARS)*, PARS Mitteilungen GI, 27th PARS Workshop, Hagen, Germany, May 4/5 2017, 2017. Gesellschaft für Informatik e.V.

Erklärung:

Ich versichere, dass ich diese Arbeit selbstständig verfasst habe und keine anderen als die angegebenen Quellen und Hilfsmittel benutzt habe.

Heidelberg, den (Datum) .....